

ABSTRACT

Title of Dissertation: THE YIN AND YANG OF AMYLOIDS:
INSIGHTS FROM ALPHA-SYNUCLEIN AND
THE PMEL17 REPEAT DOMAIN

Candace Marie Pfefferkorn, Ph.D., 2011

Dissertation Directed By: Distinguished University Professor
Devarajan Thirumalai, Institute for Physical
Science and Technology

While amyloidogenic proteins are commonly associated with human diseases such as Alzheimer's and Parkinson's disease, it is intriguing that amyloid fibrils also are utilized for essential biological processes. A key question then is why many amyloids are harmful whereas some serve essential functional roles. To begin to address this question, the environmental factors regulating the conformational changes in the Parkinson's disease-related protein, α -synuclein (α -syn), and a critical polypeptide fragment, the repeat domain (RPT) of Pmel17, the protein required for melanin formation are examined.

The role of membranes in modulating α -syn conformation is investigated because membranes are ubiquitous *in vivo* and affect α -syn aggregation *in vitro*. Using single tryptophan-containing α -syn variants (F4W, Y39W, F94W, Y125W) as site-specific fluorescent probes, distinct phospholipid vesicle and SDS micelle

interactions have been identified and membrane binding equilibria measured. The role of specific N-terminal residues in membrane binding also has been assessed. Specifically, environments of the highly sensitive Trp4 probe in α -syn polypeptide fragments (residues: 1 – 4, 1 – 6, 1 – 10, and 1 – 15) upon membrane binding were characterized using steady-state fluorescence and time-resolved anisotropy. The penetration depths of α -syn and N-terminal peptides into the lipid bilayer also were determined using brominated lipids as heavy-atom quenchers. To simultaneously monitor α -syn and bilayer structure, neutron reflectometry (NR) and a sparsely-tethered bilayer lipid membrane (stBLM) were employed. Using NR and an stBLM, α -syn concentration dependent effects on both protein structure and membrane properties were measured.

To begin to address biophysical and biochemical differences between pathological and functional amyloid, a systematic investigation of the effects of solution pH (4→7) on RPT aggregation was performed since melanosomes, acidic organelles where Pmel17 fibrils are formed, change pH during maturation. Using intrinsic tryptophan fluorescence, circular dichroism spectroscopy, and transmission electron microscopy, local, secondary, and fibril morphological structure were monitored, respectively. Notably, RPT fibril morphology can be transformed directly by changing solution pH, suggesting that pH is a natural regulatory mechanism for Pmel17 amyloid formation and its subsequent dissolution *in vivo*.

THE YIN AND YANG OF AMYLOIDS: INSIGHTS FROM ALPHA-
SYNUCLEIN AND THE PMEL17 REPEAT DOMAIN

By

Candace Marie Pfefferkorn

Dissertation submitted to the Faculty of the Graduate School of the
University of Maryland, College Park, in partial fulfillment
of the requirements for the degree of
Doctor of Philosophy
2011

Advisory Committee:

Principal Investigator Jennifer C. Lee

Distinguished University Professor Devarajan Thirumalai, Chair

Professor Sergei Sukharev, Dean's Representative

Professor Marco Colombini

Distinguished University Professor George H. Lorimer

Acknowledgements

First and foremost I would like to thank my Ph.D. thesis advisor Dr. Jennifer Lee for her continual support and mentorship during my graduate school tenure. My many experiences growing and learning with Jenn have positively impacted the way I question and think both in and outside the laboratory. I am sincerely grateful to have Jenn in my life and I look forward to her continuing support and friendship as I embark on many new journeys in the future.

Obtaining my Ph.D. would not have been possible without the love and support of my family and friends. I would especially like to thank my parents who have taught me to follow my dreams and to always do my best. I would not be the person I am today without their constant love and guidance. I would also like to give special thanks to my husband whose gentle support and encouragement over the past five years has made graduate school a wonderful time in my life.

Lastly, I would like to thank all of the past and current members of the Lee Laboratory with whom I have spent countless hours, all the members of the Laboratory of Molecular Biophysics at the NIH, and all of my professors and mentors at the University of Maryland, College Park.

Table of Contents

Acknowledgements.....	ii
Table of Contents.....	iii
List of Tables	vi
List of Figures.....	vii
List of Abbreviations	xi
Chapter 1: Amyloid Proteins and Biophysical Probes of Their Interactions with Biomembranes	1
1.1 Amyloid Proteins in Disease and Function.....	1
1.2 The Role of Membranes in Amyloid Formation.....	6
1.3 Biophysical Probes of Membrane Protein Structure.....	8
1.3.1 Secondary Structure	9
1.3.2 Tertiary Structure	9
1.3.3 The Membrane-protein Interface	11
1.4 Biophysical Techniques Used to Study the α -Synuclein-membrane Interface and Pmel17 Aggregation.....	13
Chapter 2: α-Synuclein Is a Membrane Protein Associated with Parkinson's Disease	15
2.1 α -Synuclein and Parkinson's Disease	15
2.2 α -Synuclein Discovery.....	16
2.3 α -Synuclein Primary Structure.....	18
2.4 α -Synuclein Membrane Interactions and Parkinson's Disease.....	19
2.4.1 Effect of Disease-related Mutations on Membrane Binding	19
2.4.2 Membrane Mediated α -Synuclein Oligomer Formation and Aggregation.....	20
2.4.3 α -Synuclein Induced Membrane Perturbation	22
Chapter 3: Tryptophan Probes at the α-Synuclein and Membrane Interface	24
3.1 Introduction.....	24
3.2 Materials and Methods.....	27
3.2.1 Materials	27
3.2.2 Lipid Vesicle Preparation	27
3.2.3 Recombinant Protein Expression and Purification	28
3.2.4 Steady-state Spectroscopic Measurements	29
3.2.5 Time-resolved Fluorescence Measurements.....	29
3.2.6 Circular Dichroism Data Analysis	30
3.2.7 Tryptophan Fluorescence Decay Data Analysis.....	30
3.2.8 Protein-membrane Equilibrium	31
3.2.9 Protein Packing on Lipid Vesicles.....	32
3.2.10 Computer Simulation.....	33
3.3 Results and Discussion	33
3.3.1 Membrane-mediated α -Helical Structure Formation.....	33
3.3.2 Estimation of α -Synuclein Vesicle Surface Coverage.....	38
3.3.3 Site-specific Tryptophan Probes of α -Synuclein Membrane Interactions.....	39
3.3.4 Conformational Heterogeneity of Phospholipid Vesicles-bound α -Synuclein Monitored by Tryptophan Kinetics.....	46

3.4 Summary	52
Chapter 4: Molecular Insights of N-terminal α-Synuclein at the Membrane Interface	53
4.1 Introduction	53
4.2 Materials and Methods	55
4.2.1 Materials	55
4.2.2 Recombinant Protein Expression and Purification	56
4.2.3 Phospholipid Vesicle Preparation	56
4.2.4 Steady-state Spectroscopic Measurements	57
4.2.5 Circular Dichroism Spectroscopy	58
4.2.6 ^1H Nuclear Magnetic Resonance Spectroscopy	58
4.2.7 Time-resolved Fluorescence Anisotropy	59
4.2.8 Peptide-membrane Equilibrium	60
4.3 Results and Discussion	61
4.3.1 Membrane Affinities and Gibbs Free Energies for N-terminal Peptides and Full Length α -Synuclein	61
4.3.2 Tryptophan Microenvironment at the Bilayer Interface	68
4.3.3 N-terminal Peptide Membrane Binding Probed by 1-Dimensional ^1H Nuclear Magnetic Resonance	69
4.3.4 Trp4 side-chain Bilayer Penetration	71
4.4 Summary	74
Chapter 5: Structure of the α-Synuclein Membrane Interface: Insights from Neutron Reflectometry	76
5.1 Introduction	76
5.2 Materials and Methods	77
5.2.1 Materials	77
5.2.2 Recombinant Protein Expression, Purification, and Labeling	78
5.2.3 Phospholipid Vesicle Preparation	79
5.2.4 Steady-state Spectroscopic Measurements	79
5.2.5 Preparation of Sparsely Tethered-lipid Bilayer Membranes for Neutron Reflectometry	80
5.2.6 Neutron Reflectivity Measurements	81
5.2.7 Neutron Reflectometry Data Analysis	82
5.2.8 Preparation of Supported Bilayer Membranes for Fluorescence Correlation Spectroscopy	83
5.2.9 Fluorescence Correlation Spectroscopy	84
5.2.10 Protein-bilayer Membrane Equilibrium	85
5.3 Results and Discussion	86
5.3.1 Fluorescence Correlation Spectroscopic Characterization of α -Synuclein Membrane Binding to a Planar Bilayer Membrane	86
5.3.2 Neutron Reflectometry as a Dual Probe of α -Synuclein and Membrane Structure	88
5.3.3 Using Neutron Reflectometry to Examine the Effects of α -Synuclein Concentration on the Protein-membrane Interface	93
5.4 Summary	99

Chapter 6: Effects of pH on Aggregation Kinetics of the Repeat Domain of a Functional Amyloid, Pmel17	101
6.1 Introduction.....	101
6.2 Materials and Methods.....	105
6.2.1 Materials	105
6.2.2 Protein Expression and Purification.....	105
6.2.3 Fibril Formation Kinetics and pH Titration	105
6.2.4 Fibril Characterization	107
6.2.5 Time-resolved Fluorescence	108
6.2.6 Tryptophan Quenching	109
6.2.7 pH Titration Data Analysis	109
6.3 Results and Discussion	110
6.3.1 RPT Amyloid Structure and Aggregation Kinetics	110
6.3.2 Critical Concentration for RPT Aggregation at pH 5.0	114
6.3.3 W423, a Site-specific Probe of RPT Conformation.....	115
6.3.4 W423, a Site-specific Probe of RPT Amyloid Formation	118
6.3.5 Tryptophan Fluorescence Reflects Fibril Morphologies	121
6.4 Implications.....	123
6.4 Summary.....	126
Appendix 1: Instrumentation	127
A1.1 Time-resolved Fluorescence	127
A1.2 Time-resolved Fluorescence Anisotropy	130
A1.3 Static Light Scattering.....	131
Appendix 2: Preparation and Characterization of Membrane Mimics	133
A2.1 Preparation of POPA:POPC Liposomes	133
A2.2 Characterization of 1:1 POPA:POPC Liposomes.....	134
A2.3 Preparation of Purified Synaptic Vesicles	135
A2.4 Characterization of Purified Synaptic Vesicles	136
Appendix 3: Preparation and Characterization of Dye Labeled α-Synuclein .	139
A3.1 Incorporation of Single Cysteine Mutations into α -Synuclein	139
A3.2 Dye Labeling and Purification of Single Cysteine Containing α -Synucleins	141
Bibliography	144

List of Tables

Table 1.1	Amyloidogenic polypeptides and associated disease and/or function	5
Table 4.1	Steady-state Trp4 spectral and equilibrium vesicle binding properties for full-length and N-terminal α -synuclein peptides	66
Table 5.1:	Neutron reflectometry fitting parameters for a POPA:POPC stBLM in the absence and presence of α -synuclein	91
Table 5.2:	Neutron reflectometry fitting parameters for a POPA:POPC stBLM in the absence and presence of varying concentrations of α -synuclein	97
Table 6.1	Spectral properties of soluble <i>vs.</i> fibrillar RPT at different pH	116

List of Figures

Chapter 1

Figure 1.1	Macroscopic morphology and molecular organization of amyloid fibrils	2
Figure 1.2	Amyloid formation kinetics	3
Figure 1.3	Schematic representation depicting pathways through which an unfolded/misfolded conformer can be either refolded, degraded, or converted to amyloid	6
Figure 1.4	Selected biophysical techniques used to examine membrane binding proteins	8

Chapter 2

Figure 2.1	α -Synuclein primary structure	18
------------	---------------------------------------	----

Chapter 3

Figure 3.1	Helical wheel representation for residues 1 – 44 of membrane-bound α -synuclein	26
Figure 3.2	Phospholipid vesicles induced secondary structure in α -synuclein	34
Figure 3.3	Phospholipid vesicle and sodium dodecyl sulfate micelles induced secondary structure in α -synuclein	35
Figure 3.4	Effect of zwitterionic vesicles on α -synuclein membrane binding using circular dichroism spectroscopy	35
Figure 3.5	Comparison of vesicle binding properties of wild-type and fluorescent single Trp α -synucleins	37
Figure 3.6	Inverse fluorescence lipid titration of Trp4 α -synuclein	37
Figure 3.7	Site-specific tryptophan fluorescence of α -synucleins	41
Figure 3.8	Mean wavelength of Trp α -synucleins as a function of lipid vesicles	42
Figure 3.9	Effect of zwitterionic vesicles on α -synuclein membrane binding using Trp4 fluorescence	43

Figure 3.10	Comparison of tryptophan fluorescence for micelles- and liposome-bound α -synuclein	45
Figure 3.11	Time-resolved fluorescence decay kinetics of Trp α -synucleins as a function of lipid vesicles	47
Figure 3.12	Non-negative least-squares fitting of Trp decay kinetics	48
Figure 3.13	Analysis of time-resolved Trp fluorescence decay kinetics for α -synucleins	50
 <u>Chapter 4</u>		
Figure 4.1	Schematic representation of full-length α -synuclein and N-terminal α -synuclein peptides	55
Figure 4.2	Comparison of vesicle binding of single Trp containing full-length α -synuclein (F4W) and N-terminal peptides	63
Figure 4.3	Vesicle induced secondary structural formation of P10 and P15 peptides	66
Figure 4.4	Vesicle induced secondary structural formation in P15 and the 1 – 15 wild-type peptide	67
Figure 4.5	Effect of phospholipid vesicles on Trp4 time-resolved anisotropy of F4W and N-terminal peptides	68
Figure 4.6	1D ^1H NMR spectra of N-terminal α -synuclein peptides	70
Figure 4.7	Tryptophan side-chain penetration into the vesicle bilayer	73
 <u>Chapter 5</u>		
Figure 5.1	Fluorescence correlation spectroscopy autocorrelation curves for singly labeled A90C α -synuclein exposed to a supported lipid bilayer in the absence and presence of wild-type protein	88
Figure 5.2	Neutron reflection of a sparsely tethered POPA:POPC bilayer lipid membrane and changes resulting from the addition of α -synuclein	90
Figure 5.3	Comparison of membrane induced secondary structure for protonated and uniformly deuterated α -synuclein	94

Figure 5.4	Neutron reflection of a sparsely tethered POPA:POPC bilayer lipid membrane and changes resulting from the addition of uniformly deuterated α -synuclein	95
Figure 5.5	Simplified molecular distributions for each of the organic interface layers of a POPA:POPC stBLM in the presence of varying concentrations of α -synuclein	96
Figure 5.6	Comparison of volume fraction of membrane bound α -synuclein extending into the bulk solvent and occupying the headgroup/hydrocarbon region as well as the degree of membrane thinning as a function of α -synuclein concentration.	98
 <u>Chapter 6</u>		
Figure 6.1	A schematic representation of the N-terminal domain (M α) of Pmel17 with the repeat domain highlighted	104
Figure 6.2	pH dependence of RPT aggregation kinetics and amyloid structures	112
Figure 6.3	Secondary structure of soluble and aged RPT	113
Figure 6.4	Concentration dependence of RPT amyloid formation	114
Figure 6.5	pH Dependence of W423 emission spectra for RPT	115
Figure 6.6	pH Dependence on size of soluble RPT	117
Figure 6.7	W423 emission intensity surfaces as a function of pH	119
Figure 6.8	Time-resolved anisotropy measurements for RPT	120
Figure 6.9	Acrylamide quenching for soluble and fibrillar RPT and N-acetyl-L-tryptophanamide	120
Figure 6.10	pH Dependence of time-resolved Trp fluorescence for soluble and fibrillar RPT and N-acetyl-L-tryptophanamide	122
Figure 6.11	Comparison of critical pH regimes for soluble and fibrillar RPT	124
Figure 6.12	pH induced RPT fibril morphological conversion and the melanosome maturation process	125

Appendix 1

Figure A1.1	Schematic representation of the femtosecond Ti:Sapphire and streak camera setup used to measure time-resolved fluorescence and anisotropy decays	128
Figure A1.2	Schematic representation of the streak camera	129
Figure A1.3	An image of the emission of a fluorescent protein sample generated by the streak camera and corresponding fluorescence decay curve	129
Figure A1.4	Time-resolved anisotropy data collection	131
Figure A1.5	Schematic representation of the static light scattering instrument used to monitor macroscopic protein aggregation	132

Appendix 2

Figure A2.1	Structure of POPC and POPA lipids	133
Figure A2.2	Characterization of 1:1 POPA:POPC lipid vesicles by TEM	135
Figure A2.3	Flow chart for synaptic vesicles purification	136
Figure A2.4	Confirmation of synaptic vesicle presence	137
Figure A2.5	TEM visualization of synaptic vesicles	138

Appendix 3

Figure A3.1	Primer design for G93C α -synuclein	139
Figure A3.2	Structure of 1,5-IAEDANS and IANBD amide	142
Figure A3.3	Anionic-exchange chromatogram from purification of 1,5-IAEDANS labeled G7C α -synuclein	143
Figure A3.4	SDS-PAGE gel used to confirm the purity of singly labeled 1, 5-IAEDANS α -synuclein fractions	143

List of Abbreviations

A	acceptor
aa	amino acid
α -syn	α -synuclein
A β	amyloid β
apoPs	apolipoproteins
β -ME	β -mercaptoethanol
COG	center-of-geometry
CD	circular dichroism
1D	1-dimensional
2D	2-dimensional
D	donor
DEER	double electron electron resonance
EPR	electron paramagnetic resonance
ESI-MS	electrospray ionization mass spectrometry
FRET	Förster resonance energy transfer
FTIR	Fourier transform infrared
GUVs	giant unilamellar vesicles
LBs	Lewy Bodies
NATA	N-acetyl-tryptophanamide
NR	neutron reflectometry
nSLD	neutron scattering length density
NAC	non-amyloid β component

NMR	nuclear magnetic resonance
Br ₆₋₇ PC	1-palmitoyl-2-(6,7-dibromo)stearoyl- <i>sn</i> -glycero-3-phosphocholine
Br ₉₋₁₀ PC	1-palmitoyl-2-(9,10-dibromo)stearoyl- <i>sn</i> -glycero-3-phosphocholine
Br ₁₁₋₁₂ PC	1-palmitoyl-2-(11,12-dibromo)stearoyl- <i>sn</i> -glycero-3-phosphocholine
POPA	1-palmitoyl-2-oleoyl- <i>sn</i> -glycero-3-phosphate
POPC	1-palmitoyl-2-oleoyl- <i>sn</i> -glycero-3-phosphocholine
PD	Parkinson's disease
Pmel17	premelanosome protein 17
QY	quantum yield
RSE	rapid solvent exchange
RPT	repeat domain
SAM	self-assembled monolayer
SUVs	small unilamellar vesicles
stBLM	sparsely tethered bilayer lipid membrane
ThT	thioflavin T
TEM	transmission electron microscopy
UVR	ultraviolet resonance-Raman
WT	wild-type
HC18	Z20-(Z-octadec-9-enyloxy)-3,6,9,12,15,18,22-heptaooxatetracont-31-ene-1-thiol

Chapter 1: Amyloid Proteins and Biophysical Probes of Their Interactions with Biomembranes*

1.1 Amyloid Proteins in Disease and Function

Knowledge of three-dimensional protein structure is vital given the intimate connection between protein structure and function. Though most proteins adopt stable native structures, many can undergo large structural rearrangements under certain solution conditions. Among the latter are proteins which form amyloid. Amyloid is comprised of proteinaceous fibrillar aggregates¹ that both bind fibril specific dyes such as thioflavin T (ThT)² and congo red³ and exhibit a characteristic cross β -sheet x-ray diffraction pattern.⁴ Morphologically, amyloid fibrils are usually unbranched filaments $\sim 0.1 - 100 \mu\text{m}$ in length and $\sim 10 \text{ nm}$ in width.⁵ At the molecular level, fibrils are comprised of individual β -strands running perpendicular to the long fibril axis (backbone hydrogen bonds are parallel to the long axis) that are arranged in β -sheets which extend over the length of the fibril.⁵

A transmission electron microscopy (TEM) image of fibrils as well as a schematic representation of one characteristic amyloid structure, in-register parallel β -sheets, is provided in [Figure 1.1](#). In this architecture, β -strands from adjacent stacked polypeptides are aligned in-register and parallel.⁶ Thus, β -sheets run the length of the fibril and are stabilized by backbone amide hydrogen bonds that are parallel to the long fibril axis.⁶ Though the in-register parallel β -sheet structure is common to many

*Adapted in part from Pfefferkorn, C. M., Jiang, Z., Lee, J. C., Biophysics of α -synuclein membrane interactions, *Biochim. Biophys. Acta Biomembr.* (2011), doi: 10.1016/j.bbamem.2011.07.032.

pathological amyloids, several other pathological and functional amyloids have alternate structures in which adjacent β -strands have different arrangements.⁶

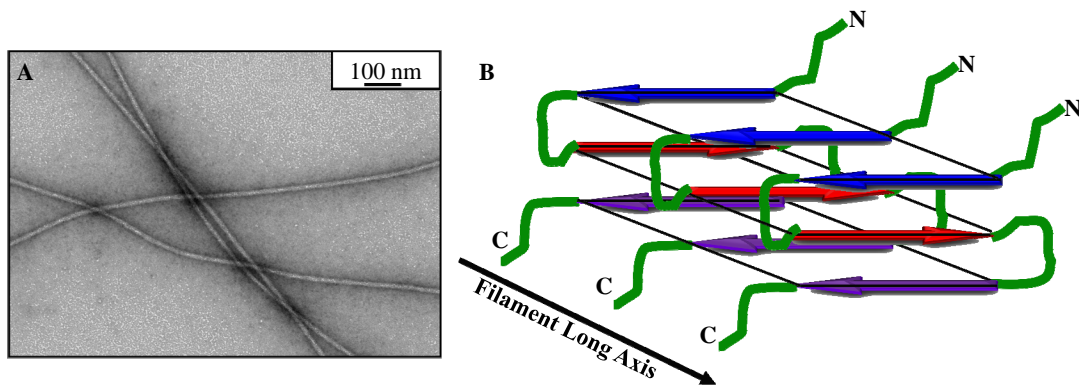


Figure 1.1: Macroscopic morphology and molecular organization of amyloid fibrils. (A) Transmission electron microscopy image of negatively stained (0.5% uranyl acetate) amyloid fibrils comprised of aggregated α -synuclein protein. (B) Schematic representation of a parallel in-register β -sheet amyloid fibril structure in which individual β -strands run perpendicular to the long axis with adjacent β -strands forming β -sheets that extend the length of the fibril.

In general, amyloid formation processes exhibit sigmoidal kinetic behavior characterized by a lag, growth, and stationary phase (Figure 1.2).⁷ Though several models have been proposed to describe amyloid formation processes, one prevalent model is based on nucleation-dependent assembly.⁷ In this model, monomeric proteins interact during the lag phase until a thermodynamically unfavorable oligomeric species, called a nucleus or seed, is formed.⁷ A growth phase then commences which is characterized by rapid fibril formation resulting from monomeric proteins templating onto the nucleus.⁷ Once equilibrium between the monomeric and fibrillar state is reached, fibril growth slows and eventually ceases indicating the beginning of the stationary phase. A nucleation-dependent mechanism for amyloid formation is attractive because the addition of a nucleus, usually fibrillar

seeds, can mitigate or even abolish the lag phase.⁷ Among the most common methods to monitor amyloid formation kinetics are ThT fluorescence, laser light scattering, and circular dichroism (CD) spectroscopy in which fibril, macroscopic aggregate, and secondary structural content are measured, respectively.

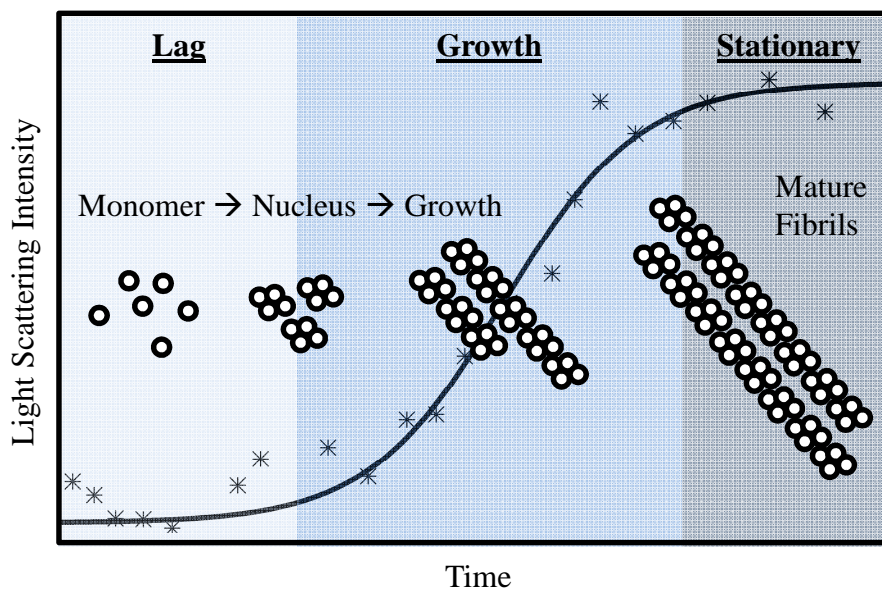


Figure 1.2 Amyloid formation kinetics. Amyloid formation kinetics for the repeat domain (RPT) of Pmel17 with lag, growth, and stationary phases indicated. Solid line is a sigmoidal fit to the data. In this example, aggregation kinetics are monitored by laser light scattering. A simplified schematic representation of the protein species present during each phase is provided for reference.

Amyloid formation has been long associated with specific human diseases such as Alzheimer's and Parkinson's disease. In these prevalent neurodegenerative diseases, a pathological hallmark is the presence of brain plaques comprised of aggregated protein. In the case of Alzheimer's and Parkinson's disease, amyloid brain deposits are composed primarily of amyloid- β ($A\beta$) and α -synuclein (α -syn) proteins, respectively. However, in the last ten years, the amyloid fold has also been discovered to play a role in essential biological processes.⁸⁻¹² For example, fibrils comprised of the melanosomal protein, Pmel17, serve as scaffolds required for proper

melanin deposition.¹³ A representative list of disease-related and functional amyloids (*i.e.* amyloids involved in essential biological processes) along with their respective biological involvement is provided in [Table 1.1](#).

Table 1.1 Amyloidogenic polypeptides and associated disease and/or function

Polypeptide	Disease/Function ^{6,8,10}
<i>Disease-related Amyloids</i>	
α -Synuclein	Parkinson's
Amyloid β	Alzheimer's
Apolipoprotein AI	Hereditary amyloidosis
Ataxins	Spinocerebellar ataxias
Atrial natriuretic factor	Artial amyloid
β_2 -Microglobulin	Hemodialysis-related amyloidosis
γ -Crystallins	Cataract
Gelsolin	Hereditary amyloidosis
Huntingtin	Huntington's
Islet amyloid polypeptide	Type 2 diabetes
Lysozyme	Hereditary amyloidosis
Medin	Amyloid in medial layer of arteries
Prion	Spongiform encephalopathies
Pro-calcitonin	Medullary carcinoma of the thyroid
Serum amyloid A	Secondary systemic amyloidosis
Superoxide dismutase	Amyotrophic lateral sclerosis
Tau	Dementia with Parkinsonism
Transthyretin	Senile systemic amyloidosis/familial amyloidotic polyneuropathy
<i>Functional Amyloids</i> ^a	
Chaplins (bacteria)	Spore surface protein
Chorion proteins (insects and fish)	Protective structure of eggshell
CsgA and CsgB (bacteria)	Biofilm formation/surface adhesion
FapC (bacteria)	Biofilm component
Fungal adhesions (fungus)	Cell adhesion
HET-s (fungus)	Regulation of heterokaryon formation
HpaG (bacteria)	Plant pathogen virulence factor
Hydrophobins (fungus)	Form amphipathic surface layer
Merozoite surface protein 2; MSP2 (protozoa)	Implicated in erythrocyte invasion
Microcin E492; Mcc (bacteriocin)	Regulate Mcc toxicity
Neuron-specific isoform of CPEB, prion (marine snail)	Long-term maintenance of synaptic changes associated with memory storage
Nsp1 (yeast)	Control nucleoplasmic mixing at nuclear pore
Peptide hormones (human)	Control hormone release
Pmel17 (human)	Melanin scaffold
Spidroin (spider)	To form the silk fibers of the web
Sup35 (yeast)	Regulation of stop-codon read-through
TasA (bacteria)	Biofilm component
Type 1 antifreeze protein; AFP (flat fish)	Ice inhibition
Ure2p (yeast)	Regulation of nitrogen catabolism

^a Species in which the functional amyloid is found is denoted in parenthesis

One central question is why functional amyloids are benign whereas their disease-related counterparts are harmful. A partial answer may be related to how efficiently cellular machinery and/or processes can regulate amyloid formation and degradation. Furthermore, it is plausible that disease-related amyloidogenic proteins adopt cytotoxic conformationally altered (misfolded) and fibrillar precursors such as spheres and annuli,¹⁴ whereas functional amyloid proteins do not. [Figure 1.3](#) provides a schematic representation depicting pathways through which an unfolded/misfolded conformer can be refolded, degraded, or converted to amyloid. Specifically, an unfolded or misfolded monomer can be degraded by the ubiquitin proteasome system (UPS) or the lysosome as well as be folded/refolded by chaperones. If not degraded or folded, soluble protein aggregates and amyloid may form. Notably, unfolded or misfolded amyloid precursors that bind to biomembranes may cause instability¹⁴ or even pores in the membrane leading to cytotoxicity.

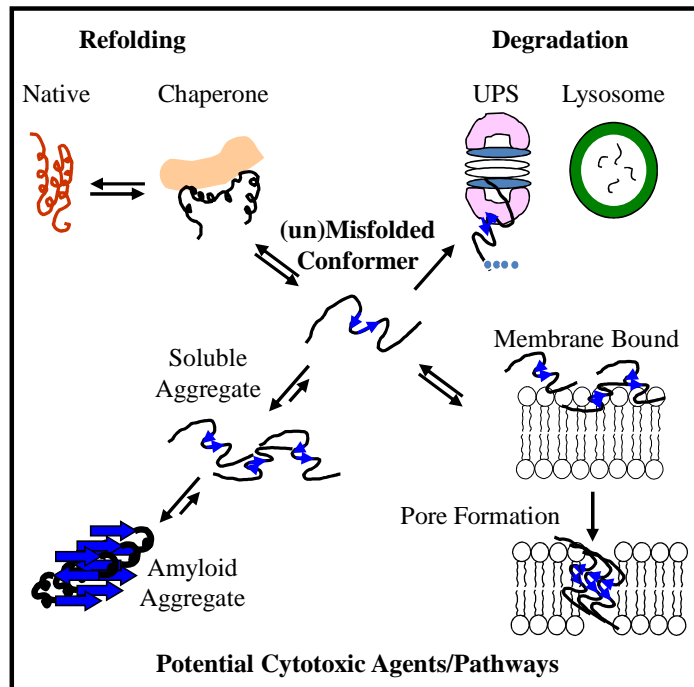


Figure 1.3 Schematic representation depicting pathways through which an unfolded/misfolded conformer can be either refolded, degraded, or converted to amyloid. The formation/interaction of membrane bound oligomers with membranes is also depicted.

1.2 The Role of Membranes in Amyloid Formation

To adopt amyloid structure, proteins must either partially unfold from the native globular state or undergo a conformational change from the unstructured state.¹⁵ For this reason, it is of utmost importance to elucidate the involvement of biomolecules that modulate protein structure by performing detailed studies of amyloid formation kinetics under different solution conditions. The role of membranes is of particular interest because membranes affect the protein-folding landscape¹⁶ and are ubiquitous *in vivo*. Indeed, it is now well established that biological membranes can modulate the aggregation kinetics of membrane interacting amyloid proteins.^{15,17}

One popular supposition for why membranes promote amyloid formation is that the membrane serves as a 2-dimensional (2D) folding template.¹⁷ While in solution the average distance between proteins is proportional to the cube root of the total protein concentration, at the 2D interface this distance is proportional to the square root of the total protein resulting in significantly decreased distances between nearest neighbors.^{17,18} Because aggregation requires specific protein-protein interactions, an effective local concentration increase at the membrane surface would enhance these contacts and subsequently aggregation. Moreover, in cases where the stability of the native state is reduced upon membrane binding, the critical concentration for aggregation may be lowered at the membrane interface further promoting aggregation.¹⁷ It is noteworthy that in addition to effective protein concentration increases, protein-protein interactions would also be modulated by the different relative ion concentrations¹⁹ and diffusion^{20,21} at the membrane interface.

Another explanation for why protein aggregation could be stimulated by the presence of membranes is that in the membrane-bound state, key hydrophobic residues, otherwise protected in the native state, could be exposed. Substantial evidence has been collected suggesting that in particular, partially helical intermediate structures may be important in amyloid formation.¹⁵ For example, it was found that in the A β peptide a transient increase in α -helical content precedes β -sheet formation and that the kinetics of α -helical formation is directly correlated to fibril formation.^{22,23} Other examples in which partially helical intermediates have been implicated include α -syn,²⁴ islet amyloid polypeptide,²⁵ tau,²⁶ and medin.²⁷

1.3 Biophysical Probes of Membrane Protein Structure

To elucidate the molecular basis of protein aggregation in the presence of membranes, techniques to probe membrane-bound protein structure and the protein-membrane interface are required. While recent advances in experimental techniques and purification procedures have facilitated the study of more membrane-protein systems than ever before,²⁸ preparation of samples that retain functionally relevant structures after purification and/or crystallization remains a challenge in most cases. As such, various complementary biophysical approaches (Figure 1.4), in addition to conventional structural techniques, such as solution-state nuclear magnetic resonance (NMR) spectroscopy^{29,30} and electron and x-ray crystallography^{31,32} have been employed to study membrane protein secondary and tertiary structure as well as the membrane-protein interface.

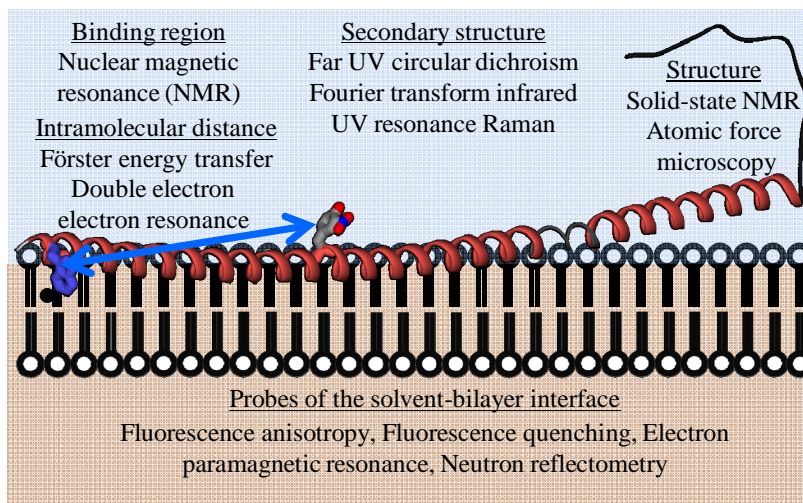


Figure 1.4: Selected biophysical techniques used to examine membrane binding proteins.

1.3.1 Secondary Structure

Among the most common biophysical probes of secondary structure are circular dichroism (CD), Fourier transform infrared (FTIR), and ultraviolet resonance-Raman (UVRR) spectroscopies. CD spectroscopy, in which the difference in left- and right-handed circularly polarized light absorption is measured, allows for direct quantitation of secondary structural content because alignments of polypeptide amide bonds (*i.e.* specific alignments corresponding to α -helical, β -sheet, or random-coil polypeptide conformations) induce distinct UV absorption bands.^{33,34}

In cases where measurements of solid and/or UV opaque samples are required, FTIR can be used since the absorption bands corresponding to the amide bond stretching frequencies are also modulated by polypeptide secondary structure.^{35,36} Though less widely applied, an emerging technique, UVRR, in which inelastic UV light scattering is measured, can also be employed to monitor secondary structural changes in proteins in presence of lipid membranes.³⁷ One advantage of UVRR over CD and FTIR is that by tuning into (resonance) the aromatic absorption bands, one can obtain high sensitivity to Tyr and Trp residues and hence the ability to characterize site-specific environments and structure.^{37,38}

1.3.2 Tertiary Structure

Though solution-state NMR is a widely used protein structural determination technique, high concentrations of isotopically labeled reconstituted protein is needed and the membrane bound protein must isotropically reorient on NMR relevant time scales. The latter point has particularly limited the use of solution-state NMR in the structural determination of membrane proteins because protein resonances simply

disappear upon association with the comparatively large phospholipid vesicles.³⁰ However, this NMR signal disappearance can be useful for identifying residues that are membrane bound.³⁹ Alternately, by using small membrane mimics such as micelles, solution-state NMR has been quite successful in producing structural models.^{17,40}

To address the problem of slow protein reorientation at the membrane interface, oriented and magic angle spinning solid-state NMR methods can be employed. In oriented solid-state NMR, membranes are aligned such that anisotropy inherent in chemical shifts, quadrupolar interactions, and dipolar couplings can be used to extract information regarding the tilt and pitch of helices interacting with membranes.^{29,41} When alignment of the membrane is not feasible, magic angle spinning solid-state NMR is particularly useful. In this technique, the sample spins at an angle with respect to the static magnetic field in such a way that signals are significantly enhanced.^{41,42} Using magic angle solid-state NMR, structural information on membrane-bound proteins can be extracted including distance and backbone dihedral angle restraints.

Distance constraints between specific residues in soluble or membrane bound proteins can be determined by exploiting Förster resonance energy transfer (FRET) and double electron electron resonance (DEER). In FRET, the energy transfer between fluorescent donor (**D**) and energy acceptor (**A**) molecules can be determined since the energy transfer rate, or efficiency, depends on the inverse sixth power of the distance between the **D** and **A**.⁴³⁻⁴⁶ By monitoring fluorescence from proteins containing **D** and **A** molecules in the presence and absence of membranes, changes in

pairwise distances can be extracted.^{47,48} In DEER, the coupling between two residues tagged with electron spin labels (typically between nitroxide spin labels) can be measured and correlated to distance.⁴⁹

1.3.3 The Membrane-protein Interface

Several fluorescence methods can be utilized to probe site-specific protein interactions with the membrane. Since many intrinsic and extrinsic fluorophores are highly sensitive to local environment, changes in fluorescence features (*e.g.* mean wavelength and quantum yield (QY)), can inform on membrane binding. For example, upon interaction with the hydrophobic membrane core, tryptophan fluorescence can shift by as much as 25 – 28 nm.^{50,51} In addition to membrane binding, differences in steady-state fluorescence QY also can reflect interactions with specific charged lipid headgroups or amino acid (aa) side chains.⁵² Moreover, because QY is greatly reduced in the presence of heavy-atom quenchers such as iodide or bromine, site-specific solvent/membrane exposure can be determined.⁵³⁻⁵⁶ Using fluorescence quenching, hydrophobic α -helical regions for several transmembrane peptides have been identified.⁵⁷

Similar determination of site-specific solvent or lipid exposure can be accomplished using electron paramagnetic resonance (EPR). In EPR, the interaction of unpaired electron spins in an external magnetic field is monitored. Though most systems do not contain unpaired electrons, EPR spin labels can be incorporated to determine site-specific information on molecular environment. For example, EPR signals can distinguish between a spin label in the O₂ rich membrane, or the aqueous

phase by using an extrinsic probe such as nickel ethylenediamine-N-N'-diacetic acid (NiEDDA).⁵⁸

Fluorescence anisotropy is another method informing on site-specific environments and membrane association. In fluorescence anisotropy, the extent of reorientation of the fluorophore between polarized excitation and emission planes is measured. Since the degree of reorientation of the fluorescence emission depends the rotational diffusion of the fluorophore, information regarding the size and shape of the diffusing molecule and the solvent viscosity can be extracted.⁵⁹ Anisotropy measurements are particularly useful in the study of membrane associating proteins, because both solvent viscosity and size change upon membrane binding. Furthermore, membrane-induced protein oligomerization and aggregation can be monitored using this technique.

One promising emerging technique for the study of protein-membrane interactions is neutron reflectometry (NR).⁶⁰⁻⁶² In this technique, neutrons impinge on a horizontally oriented sample at small angles ($< 5^\circ$) and scattered neutrons are measured. Using NR, the structure of deposited materials up to several hundred nm from the surface normal can be measured with angstrom level resolution.⁶³ The recent development of a sparsely-tethered solid-supported sparsely-tethered bilayer lipid membrane (stBLM) for use in NR has enabled simultaneous measurement of both membrane properties (*e.g.* membrane thickness) as well membrane-bound protein structure.⁶⁴ NR and a stBLM has recently been employed to study the effect of A β oligomers on membrane properties⁶² and the structure of functional *Staphylococcus aureus* α -hemolysin channels.⁶¹

1.4 Biophysical Techniques Used to Study the α -Synuclein-membrane Interface and Pmel17 Aggregation

In this work, several of the aforementioned biophysical techniques have been employed to elucidate the site-specific interactions of α -syn with model membranes and the conformational changes in the repeat domain (RPT) of Pmel17. One primary technique used is site-specific fluorescence. In particular, the exquisite environmental sensitivity of intrinsic Trp fluorescence is exploited to determine α -syn-membrane interaction sites and to generate equilibrium protein-phospholipid vesicle binding curves. Site-specific Trp fluorescence also is used to determine conformational changes in RPT as a function of its aggregation state and pH solution condition.

Time-resolved Trp fluorescence provides additional insights into conformational heterogeneity of α -syn in the presence of phospholipid vesicles. This technique is also used to determine if specific α -syn peptide fragments bind to phospholipid vesicles and to report on RPT oligomerization state. Fluorescence measurements in the presence of vesicles containing bromine allow for the site-specific determination of α -syn insertion into the bilayer. Another fluorescence quencher, acrylamide, is used to determine the level of solvent exposure of the Trp side chain in RPT under different solution conditions. Fluorescence correlation spectroscopy, a single molecule technique in which the concentration and diffusion of a fluorescently tagged species can be quantified, has also been used to determine α -syn-planar membrane bilayer binding equilibrium.

In addition to fluorescence spectroscopic methods, various additional complementary biophysical techniques are used in this work. One of these techniques is CD spectroscopy. Specifically, CD reports on membrane induced random-coil-to- α -helical transitions in α -syn as well as the secondary structures associated with RPT oligomerization and aggregation states. Solution-state NMR is employed as an independent assay of α -syn membrane interaction. TEM has been particularly useful in assessing macroscopic aggregate formation in both α -syn and RPT. Finally, the use of the emerging biophysical technique NR as a dual probe of membrane-bound α -syn and bilayer membrane structure is described.

Chapter 2: α -Synuclein Is a Membrane Protein Associated with Parkinson's Disease*

2.1 α -Synuclein and Parkinson's Disease

Parkinson's disease (PD) is a prevalent age-related neurodegenerative disorder with an estimated 1.5% lifetime risk for developing the disease.⁶⁵ PD patients exhibit resting tremors, bradykinesia, rigidity, and impaired balance caused by the loss of dopamine-producing cells in a midbrain region called the *substantia nigra*.⁶⁵ The origin of dopaminergic cell death is unknown; however, biochemical, histological, and genetic studies have implicated a neuronal protein, α -syn, in PD pathogenesis. Particularly, α -syn is the primary component of intracellular proteinaceous aggregates called Lewy bodies (LBs) and neurites found in PD patients.⁶⁵ While soluble α -syn is characterized as natively unfolded *in vitro*,⁶⁶ it is the aggregated β -sheet form (amyloid fibrils) that is found in LBs and neurites.^{8,67} It is clear that it is not simply the presence of α -syn that is associated with PD, but also its corresponding conformational state. Protofibrillar (oligomeric) species have also been implicated as pathogenic agents;^{67,68} however, the exact role of α -syn oligomers in cytotoxic and aggregation pathways is not clear. In addition, oligomers of α -syn have been shown to both accelerate⁶⁹ and inhibit α -syn fibril formation.⁷⁰ It is these features that consequently place PD in the category of a protein misfolding disease.^{8,71}

*Adapted in part from Pfefferkorn, C. M., Lee, J. C. Tryptophan probes at the α -synuclein and membrane interface, *J. Phys. Chem. B* 114 (2010) 4615 – 4622. and Pfefferkorn, C. M., Jiang, Z., Lee, J. C., Biophysics of α -synuclein membrane interactions, *Biochim. Biophys. Acta Biomembr.* (2011), doi: 10.1016/j.bbamem.2011.07.032.

Further implicating α -syn in PD are genetic findings that link early-onset PD to gene triplication⁷² and duplication⁷³ and three missense mutations (A30P, E46K, and A53T).⁷⁴⁻⁷⁶ Moreover, age-related increases in α -syn concentration also are observed in *nigral* brain regions.⁷⁷ Recent work demonstrates that triple α -, β -, γ -syn knockout mice exhibit age-dependent neuronal dysfunction providing further support for the tight connection between α -syn and PD.⁷⁸

2.2 α -Synuclein Discovery

The name synuclein (syn) was first given in 1988 to a novel 143 aa protein isolated from the presynaptic terminals and nuclei of the nervous tissues of the Pacific electric ray, *Torpedo californica*.⁷⁹ Two years later, a similar 134 aa phosphorylated protein was discovered in bovine brain neuron synapses; however, it was named phosphoneuroprotein 14.^{80,81} In subsequent independent work, a hydrophobic 35 aa sequence (termed non-amyloid β component; NAC) was identified in Alzheimer's disease (AD) amyloid plaques whose 140 aa precursor protein was coined NACP, or non-amyloid β component precursor protein.⁸² Yet another group discovered a homolog of NACP in zebra finch and called it synelfin.⁸³ Though identified in different organisms, all of these proteins are similar in size (134 – 143 aa), do not contain Cys or Trp residues, contain imperfect amphipathic aa repeats, and have a highly acidic C-terminal domain.⁸³

Finally, it became clear that synelfin, synuclein, and NACP were homologous proteins and thus, designated as α -syn. The human homolog of phosphoneuroprotein 14 was called β -syn.⁸⁴ Subsequently, yet another member of the synuclein family, γ -syn, was identified in breast cancer tissue.⁸⁵ Though the synucleins (α , β , and γ) are

highly homologous,^{83,86} and likely share similar biological functions *in vivo*, it is α -syn that has gained widespread interest due to its involvement in PD etiology.

To pinpoint a definitive role of α -syn, numerous *in vivo* and *in vitro* studies were conducted. A role of α -syn in membrane related cellular function, specifically in coordinating nuclear and synaptic events, was first predicted based on the localization of synuclein from the *Torpedo californica*.⁷⁹ Studies on canary α -syn further demonstrated a connection between α -syn expression and synaptic plasticity during learning.⁸³ Direct evidence for localization of α -syn near synaptic vesicles was later achieved *via* immunogold labeling of α -syn and visualization by electron microscopy.⁸⁷

Though α -syn knockout mice do not exhibit noticeable phenotypic changes as compared to wild type (WT) mice,^{88,89} differences in cells cultured from knockouts,⁹⁰ in the level of dopamine release,^{88,89,91} and in the quantity of the synaptic vesicle reserve pool^{92,93} point toward the involvement of α -syn in synaptic vesicle trafficking. Indeed more recent work shows that α -syn is required for the maintenance of continuous presynaptic SNARE (sensitive factor attachment protein receptor) complex assembly, a complex required for neurotransmission.⁹⁴

A correlation between mitochondrial dysfunction and PD⁹⁵ has also prompted significant interest in α -syn interactions with mitochondrial membranes. Specifically, it has been proposed that intracellular acidification resulting from oxidative or metabolic stress can induce translocation of α -syn from the cytosol to the surface of the mitochondria.⁹⁶ Using FRET-based reporters, it was shown that the conformation of α -syn is indeed altered in the presence of mitochondrial membranes.⁹⁷

2.3 α -Synuclein Primary Structure

α -Syn primary structure has several distinct characteristics. One dominating feature is that the N-terminal 89 residues contain seven imperfect 11 aa repeats (consensus sequence KXKEGV, Fig. 2.1) that are amphipathic in nature. These repeats, which contain charged residues flanked by paired lysine residues at the apolar-polar interface (class A₂ helix)⁹⁸ are also motifs found in AII, CI, CII, and CIII exchangeable apolipoproteins.^{99,100} The central region (residues 61 – 95), or NAC region, is composed of nonpolar side-chains and is important for promoting protein aggregation.¹⁰¹ In contrast, the C-terminal domain is highly acidic (15 carboxylates), does not generally associate with membranes,^{102,103} or form part of the fibril core.¹⁰⁴⁻

107

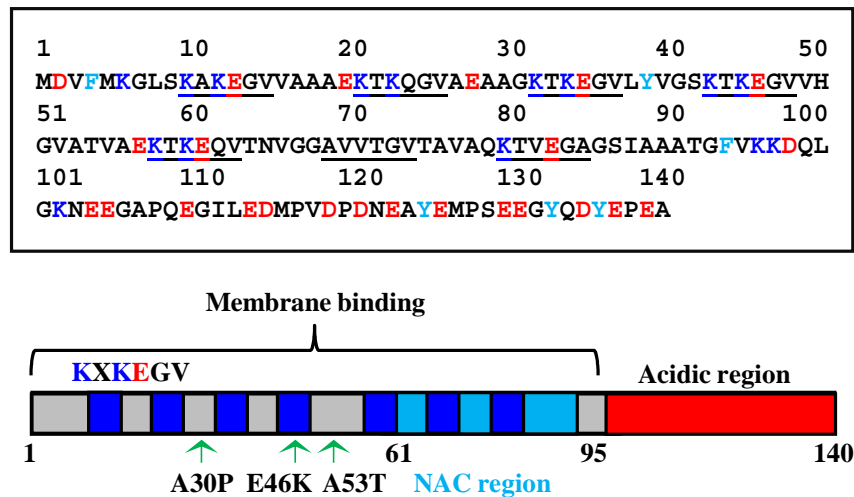


Figure 2.1 α -Synuclein primary structure. (Top) α -Syn primary amino acid sequence with aromatic (cyan), acidic (red), and lysine (blue) residues highlighted and the seven imperfect consensus sequence (KXKEGV) repeats underlined. (Bottom) Schematic representation of α -syn with amphipathic repeats, non-amyloid β component (NAC) region, membrane binding domain, and acidic region in blue, cyan, gray, and red, respectively. The location of the amphipathic repeats, the disease-related mutations, and the membrane binding domain also are denoted.

2.4 α -Synuclein Membrane Interactions and Parkinson's Disease

Despite a general consensus regarding the participation of α -syn in PD,^{65,108} work is still ongoing regarding the role of α -syn-membrane interactions. One link is that the presence of disease-related mutations modulates α -syn membrane binding *in vitro*.¹⁰⁹⁻¹¹⁵ Moreover, as PD is classified as a protein misfolding disease,^{8,71} perhaps the most compelling biophysical evidence is that the presence of membranes affects α -syn secondary structure.¹¹⁶ It is plausible that upon membrane binding, energy barriers inhibiting the formation of potentially toxic, oligomeric or β -sheet structures are lowered. Another mechanism, supported by mounting experimental data, is that α -syn membrane binding results in membrane instability and/or permeabilization, both of which could impact various *in vivo* processes.

2.4.1 Effect of Disease-related Mutations on Membrane Binding

Disparities in the membrane binding properties of WT and PD-related mutant α -synucleins were first noted in 1998 when it was reported that WT and A53T bound to rat brain vesicles whereas A30P did not.¹¹¹ Although to varying degrees, subsequent studies revealed further disparities between the membrane affinity of WT and A30P. In 2000, Perrin *et al.* showed using site directed mutagenesis and CD spectroscopy that the familial mutants had little (A30P) or no (A53T) effect on lipid binding or α -helicity.¹¹⁴ In contrast, using ultracentrifugation, CD spectroscopy, and low-angle X-ray diffraction Jo *et al.* found that A30P was defective in binding while A53T almost showed a comparable binding ability to WT α -syn.¹¹² Bussell *et al.* later confirmed that A30P, but not A53T, decreased lipid binding affinity.¹⁰⁹

Though some inconsistencies between the relative effects of the A30P and A53T mutation on membrane binding exist, it is likely that these differences can be accounted for by the fact that experiments were performed using model membranes of different composition and size and under different solution conditions. For example, in an isothermal calorimetry study, it was shown that A30P shared a similar binding affinity to the WT in a gel phase (*i.e.* DPPC) whereas binding was weaker in the liquid crystalline phase (*i.e.* DOPC/DOPG) as compared to WT.¹¹³ Moreover, it was shown using giant unilamellar vesicles (GUVs), that the A30P protein bound less efficiently compared to WT α -syn.¹¹⁵

Though less research has been conducted on the effects of the E46K mutant due to its more recent discovery,⁷⁶ unlike A30P, the presence of E46K generally increases α -syn membrane affinity.^{110,115} Since α -syn prefers anionic surfaces,¹¹⁶ it is likely the introduction of an additional positive charge enhances electrostatic forces between the protein and the anionic membrane. Whether the membrane affinity is increased (E46K) or decreased (A30P), it is clear that under certain solution conditions the presence of mutations can modulate the equilibrium between solution and membrane-bound conformations.

2.4.2 Membrane Mediated α -Synuclein Oligomer Formation and Aggregation

It is unclear whether the β -sheet structure found in the LBs of PD patients are protective or toxic to cells in the brain; however, substantial evidence show that the presence of membranes or membrane mimics can modulate the formation of β -sheets *in vitro*.¹¹⁷⁻¹¹⁹ One possibility is that the membrane surface facilitates local increases in α -syn concentration and therefore, stimulates aggregation.^{17,120} This reasoning is

attractive because it is known that increased α -syn concentration caused by gene triplication or duplication leads to early onset PD.^{72,73}

Notably, α -syn aggregation kinetics are highly dependent on the ratio of protein-to-membrane mimic in solution.^{118,119} This observation is consistent with another possibility that membrane binding induces the formation of toxic or aggregation-prone oligomers. This idea first was discussed in the context of CD data showing that α -syn aggregation rate is correlated to the level of α -helicity (partial and saturating helicity correspond to accelerated or slowed aggregation, respectively).^{118,119} This suggestion that membranes promote oligomer formation is corroborated by various other studies.¹²¹ For example, EPR data on small unilamellar vesicles (SUVs) bound α -syn, reveal a membrane induced dimeric structure.¹²² In another recent report, a trifluoroethanol induced partially helical monomeric species of α -syn was characterized and associated with enhanced fibril formation.²⁴ Interestingly, though disease-related mutants (A30P, E46K, A53T) exhibited similar TFE-induced secondary structure, oligomerization rates differed substantially as compared to WT protein, bolstering the connection between membranes and PD pathogenesis.²⁴

Substantial experimental data also support a likely prominent role of membranes in modulating α -syn oligomerization and/or protein aggregation *in vivo*. In the presence of isolated brain fractions, α -syn was found to aggregate, whereas no aggregates were detected in the cytosolic fraction.¹²³ The addition of membrane-bound α -syn also was found to seed aggregation in the cytosolic fraction.¹²³ Moreover, chemical cross-linking experiments in cells treated with high

concentrations of fatty acids show that α -syn forms dimers and trimers that preferentially associate with the phospholipid monolayers surrounding triglyceride-rich lipid droplets as well as other cellular membranes.¹²⁴ Interestingly, while the PD-related mutant E46K also localized to the lipid droplets and membranes, A30P remained cytosolic.

2.4.3 α -Synuclein Induced Membrane Perturbation

One mechanism through which amyloidogenic proteins can cause cellular dysfunction is by inducing instability in membranes.¹²⁵⁻¹²⁸ In 2001, it was shown that protofibrillar α -syn can cause transient permeabilization in anionic membranes and thus it was proposed that α -syn could alter calcium flux into the cytosol, depolarization of mitochondrial membranes, and/or leakage of intra-vesicular neurotransmitter molecules, such as dopamine.¹²⁹ Further experiments revealed that protofibril induced membrane leakage is increased when disease-related mutations are present (A30P and A53T).¹³⁰

Numerous other studies have since confirmed that indeed various conformations of α -syn can cause membrane instability and even pore formation. For example, using atomic force microscopy and vesicle dye leakage assays, it was shown that membrane disruption is positively correlated to α -syn membrane affinity and that fibrillar, as well as oligomeric, α -syn enhances membrane permeability.¹¹⁹ It was later shown that the presence of WT, E46K, and A53T protein can induce formation of ion channels in anionic SUVs, whereas A30P did not under similar solution conditions.¹³¹

Van Rooijen *et al.* showed that the presence of anionic lipids and lipid-disordered domains affects the ability of α -syn to perturb membranes,^{132,133} offering new insight into the specific conditions promoting membrane disruption. Subsequent study revealed that disruption of vesicles is caused by non-equilibrium processes and that despite rapid dye efflux from vesicles membrane morphology is maintained in the presence of oligomeric α -syn.¹³⁴

Using solid-state NMR and EPR methods it has been determined that α -syn pores are comprised of β -sheet structures unique from those found in amyloid fibrils.¹³⁵ In recent work, a low resolution wreath shaped α -syn oligomer was identified by x-ray scattering methods and was shown to disrupt liposomes.¹³⁶

Though the specific mechanism of membrane disruption is yet to be determined, several recent reports have demonstrated that α -syn also can transform membrane surface topology. This phenomenon was brought to light when it was noted that the addition of α -syn to SUVs induced tubular structures as well as multilamellar and branched vesicles.^{39,136} Further work showed that α -syn can increase membrane curvature causing smaller vesicles and tubules to form.¹³⁷ Accordingly, fluorescence microscopic studies on supported lipid bilayers also revealed tubule formation as well as a correlation between increased tubulation and the presence of anionic lipids and disease-related mutations.¹³⁸

Chapter 3: Tryptophan Probes at the α -Synuclein and Membrane Interface^{*}

3.1 Introduction

To elucidate the connection between α -syn membrane interactions and PD etiology, numerous *in vitro* biophysical studies to determine membrane-bound α -syn conformation have been conducted. Initial CD studies demonstrated that the protein undergoes disordered-to-helical structural changes upon the addition of membrane mimics such as SDS micelles and anionic phospholipid vesicles of varying size and composition.¹¹⁶ Later, several structural techniques were employed for molecular level insights. α -Syn structures derived from NMR, site-directed spin labeling EPR, and fluorescence spectroscopy show large N-terminal α -helical domain formation upon membrane binding.¹³⁹⁻¹⁴⁵ Specifically, SDS-micelle-bound α -syn conformation derived from NMR data¹⁴² reveal two antiparallel α -helices (residues 3-37 and 45-92) separated by a short linker (residues 38-44) while EPR¹⁴⁶⁻¹⁴⁸ and single molecule fluorescence measurements^{48,149} using SUVs suggest that one continuous, extended α -helix is adopted. In both SDS micelle- and SUV-bound cases, the acidic C-terminal region (aa 101 – 140) remains disordered and solvent-exposed.

^{*} Adapted from Pfefferkorn, C. M., Lee, J. C. Tryptophan probes at the α -synuclein and membrane interface, *J. Phys. Chem. B* 114 (2010) 4615 – 4622. Thanks to Dr. Hank Fales (Laboratory of Applied Mass Spectrometry) for technical assistance with ESI-MS, Myoung-Soon Hong (Laboratory of Cell Biology), Dr. Mathew Daniels, and Patricia Connelly (Electron Microscopy Core Facility) for technical assistance with electron microscopy, Dr. Grzegorz Piszczek (Biophysical Facility) for assistance with the dynamic light scattering measurements, and Michel de Messieres for assistance with computer modeling.

Despite numerous work on membrane composition and size effects on α -syn membrane binding properties, a consensus on the conditions required to promote α -syn into one, both, or other variants of the proposed membrane-bound structures remains elusive. It is not clear whether or not these conformers are modulated by membrane surface availability (*i.e.* surface area available for protein binding), detergent or phospholipid headgroup composition, or simply solution conditions. Indeed, a recent NMR study suggests that there are multiple distinct α -syn membrane binding modes that are dependent on α -syn-to-lipid stoichiometry.³⁹ Furthermore, given the ability for this protein to undergo large conformational rearrangements, it is even more likely that bound structures are not mutually exclusive and can interchange.

Regardless of the specific length and arrangements of α -helical segments, based on insights from primary structure as well as structural studies, an 11/3 α -helical periodicity was proposed for membrane-bound α -syn as is the case of apolipoprotein AI.^{99,100} In an 11/3 α -helix, there are three full turns over 11 residues ($3.6\bar{6}$ residues per turn) as compared to five full turns over 18 residues in an ideal helix (3.6 residues per turn).^{141,145,148} Based on EPR data for SUVs bound α -syn, a contiguous 11/3 α -helical region was confirmed for residues 9 – 89.¹⁴⁸ A 11/3 helical wheel representation of the first 44 N-terminal residues of α -syn is shown in [Figure 3.1](#). In this representation, it is clear that acidic residues are water facing while basic residues flank the lipid-water interface.

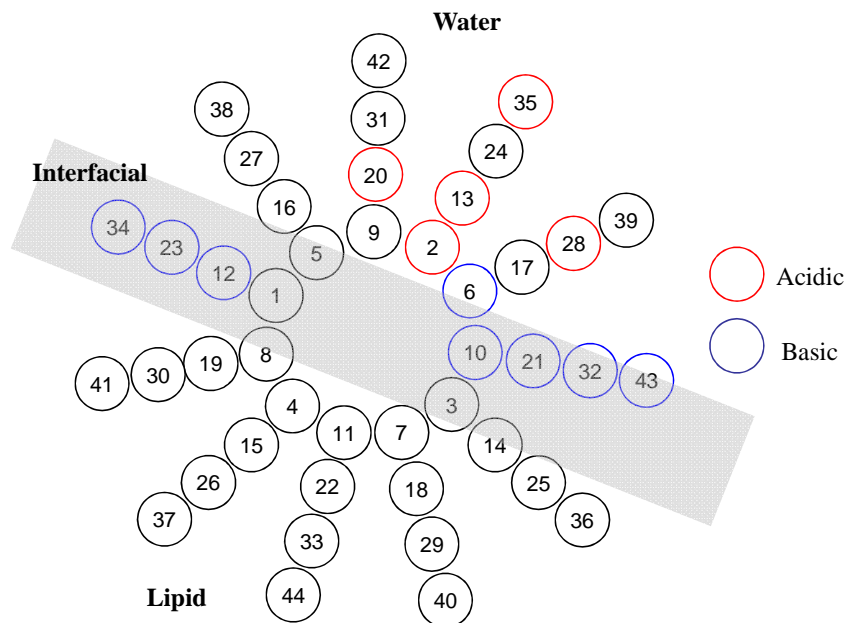


Figure 3.1 A 11/3 helical wheel representation for residues 1 – 44 of membrane-bound α -synuclein. Each residue is denoted by a numbered circle with charged and basic residues denoted in red and blue, respectively. Water, lipid, and interfacial regions are indicated for reference.

To develop a detailed understanding of how membranes influence α -syn conformation, site-specific probes of protein conformational heterogeneity and polypeptide-membrane interactions are necessary. Fluorescence spectroscopy is particularly well suited for this application because of the availability of environmentally sensitive fluorophores and the ease of performing experiments near physiological temperatures and concentrations even down to a single molecule. In prior work, tryptophan⁴⁷ and 5-fluorotryptophan¹⁵⁰ have been exploited as fluorescent amino acids of α -syn conformation and dynamics^{151,152} in solution. The emission properties of the indole side chain are exquisitely responsive to local environment and conformation providing remarkably useful probes of protein-lipid interactions.^{44,153-157} In this study, anionic unilamellar vesicles and SDS micelles are employed as

membrane mimics to investigate membrane-induced conformational changes by fluorescence as well as CD spectroscopy. Tryptophan is substituted at four different aromatic residues (F4W, Y39W, F94W, and Y125W) to report on local polypeptide environment and conformational heterogeneity in vesicles-bound and SDS-micelles-bound α -syn. Furthermore, insights into the role of surface coverage (total number of proteins bound and respective surface area occupied) were extracted from saturating equilibrium binding curves for all α -synucleins in the presence of vesicles.

3.2 Materials and Methods

3.2.1 Materials

Lipids in chloroform were purchased from Avanti Polar Lipids (Alabaster, AL), N-acetyl-tryptophanamide (NATA), and sodium dodecyl sulfate (SDS) were purchased from Sigma (St. Louis, MO) and used as received.

3.2.2 Lipid Vesicle Preparation

Lipid vesicles were made from a 1:1 molar ratio of 1-palmitoyl-2-oleoyl-sn-glycero-3-phosphate (POPA) and 1-palmitoyl-2-oleoyl-sn-glycero-3-phosphocholine (POPC). Solutions of 1:1 POPA and POPC dissolved in chloroform were dehydrated under a nitrogen stream for 15 minutes followed by vacuum desiccation for 45 minutes to ensure complete removal of organic solvent. Dehydrated samples were resuspended in 10 mM NaP_i, 100 mM NaCl buffer, pH 7.4 to a final concentration of 5 mg/mL. Complete dissolution was achieved by bath sonication for 5 minutes. Unilamellar vesicles were prepared *via* ultrasonication in a water bath (45 minutes, 50% duty cycle, microtip limit, Branson 415 Sonifier). Vesicle solutions were diluted

to a final concentration of 2.5 mg/mL and equilibrated overnight (14 – 24 h) at 30°C. Vesicles were prepared freshly for each experiment. Stock lipid concentrations were confirmed using the Bartlett method.¹⁵⁸ An average vesicle hydrodynamic radius of ~40 nm was measured using an 18-angle photometer dynamic light scattering instrument with QELS detection (Wyatt EOS). Vesicle sizes ranged from 20 – 100 nm as visualized by electron microscopy (JEOL-1200EX).

3.2.3 Recombinant Protein Expression and Purification

Wild-type and single Trp-containing α -synucleins were expressed^{84,159} and purified⁴⁷ as previously reported with minor modifications. All purification steps are performed at 4 °C and a HiPrep 16/10 DEAE FF column (GE Healthcare) is used for the first chromatographic step. The protein was eluted with a linear gradient from 100 – 300 mM NaCl in 20 mM Tris buffer (pH 7.4 – 8.0). Protein concentrations were determined using a molar extinction coefficient estimated on the basis of amino-acid content:¹⁶⁰ $\epsilon_{280 \text{ nm}} = 5,120 \text{ M}^{-1}\text{cm}^{-1}$ (wild-type); $\epsilon_{280 \text{ nm}} = 9,970 \text{ M}^{-1}\text{cm}^{-1}$ (Y39W and Y125W); $\epsilon_{280 \text{ nm}} = 10,810 \text{ M}^{-1}\text{cm}^{-1}$ (F4W and F94W). The purity of all protein samples was assessed by native- and SDS-PAGE on a Pharmacia Phastsystem (Amersham Biosciences) visualized by silver-staining methods. The protein molecular weights were confirmed by electrospray ionization mass spectrometry (ESI-MS). All purified proteins were concentrated using Centriprep YM-3 (MWCO 3kD, Millipore) and stored at –80 °C.

3.2.4 Steady-state Spectroscopic Measurements

Spectroscopic measurements were made as follows: absorption, Cary 300 Bio spectrophotometer; CD, Jasco J-715 spectropolarimeter (198 – 260 nm, 1 nm steps, 1 nm bandwidth, 0.5 s integration time, and 50 nm/min); and luminescence, Fluorolog-3 spectrofluorimeter ($\lambda_{\text{ex}} = 295$ nm, $\lambda_{\text{obs}} = 300 - 500$ nm, 0.20 – 0.25 s integration time, 1 nm excitation and emission slit widths). All measurements were collected at 25 °C using temperature controlled cuvette holders except for absorbance experiments. Prior to experiments, all protein samples were exchanged into the appropriate buffer (10 mM NaP_i, 100 mM NaCl, pH 7.4) using gel filtration chromatography (PD-10 column, GE Healthcare). For SDS and lipid titration experiments, protein (5 μ M) was added to SDS (40 mM) or varying concentrations of lipid (0 – 2.5 mM) in appropriate buffer (10 mM NaP_i, 100 mM NaCl, pH 7.4), respectively. For inverse titration experiments, varying concentrations of protein (1 – 20 μ M) were added to a fixed concentration of lipid (1 mM) in appropriate buffer (10 mM NaP_i, 100 mM NaCl, pH 7.4). All protein-SDS and protein-lipid solutions were incubated for at least 30 minutes at RT prior to measurement. Steady-state fluorescence spectra were measured before and after laser experiment to verify minimal photodamage (<10%).

3.2.5 Time-resolved Fluorescence Measurements

Tryptophan fluorescence decay kinetics were measured using the fourth harmonic (295 nm) of a regeneratively-amplified femtosecond Ti:sapphire (Clark-MXR) pumped optical parametric amplifier laser (Light Conversion) as an excitation source (60 – 260 μ W, 1 kHz) and a picosecond streak camera (Hamamatsu C5680) in

photon counting mode for detection. Tryptophan emission between 325 and 400 nm was selected through edge (REF-325) and short-pass (UG-11) filters (CVI Laser). Protein samples (3 – 5 μM in 10 mM NaP_i , 100 mM NaCl buffer, pH 7.4) were deoxygenated on a Schlenk line by 3 sets of 5 repeated evacuation/Ar fill cycles over 30 minutes. Buffer solutions were filtered (0.22 μm membrane) to remove any particulate matter. A collection temperature of 25 $^\circ\text{C}$ was maintained using a temperature controlled cuvette holder. To ensure good signal to noise, all kinetics data were collected such that at least 10,000 counts were achieved in highest channel.

3.2.6 Circular Dichroism Data Analysis

Mean residue ellipticity, $[\Theta]$ ($\text{deg cm}^2 \text{ d mol}^{-1}$), was calculated according to the equation $[\Theta] = \frac{100\theta}{c l N}$, where θ is the measured ellipticity (mdeg), c , the sample concentration (mM), l , the path length (cm), and N , the number of amino acids.

Percent α -helicity was calculated using the equation $\frac{[\Theta]_{222\text{nm}} - 3,000}{-39,000} \times 100$.

Reference values of $[\Theta]_{222\text{ nm}} = 0$ and $-36,000$ ($\text{deg cm}^2 \text{ d mol}^{-1}$) were used for 0% and 100% helicity, respectively.¹⁶¹

3.2.7 Tryptophan Fluorescence Decay Data Analysis

Fluorescence decay kinetics were logarithmically compressed (100 points per time decade) and normalized ($I(t=0) = 1$). Kinetics were fit using a MATLAB (The Mathworks, Inc.) algorithm (LSQNONNEG; hereafter referred to as NNLS) that minimizes the sum of the squared deviations (χ^2) between the observed and calculated

values of $I(t)$, subject to a nonnegativity constraint on the probability distribution of rate constants, $P(k)$. NNLS fitting produces the narrowest $P(k)$ distributions.^{47,162}

3.2.8 Protein-membrane Equilibrium

Binding equilibrium data were modeled according to the simple law of mass action for identical and independent binding sites.^{163,164} Estimation of apparent association constants were extracted for the following two-state equilibrium:



where P_f is the free α -syn concentration, B_f is the free binding sites, and PB_b is the bound α -syn concentration (occupied binding sites). The total binding sites (B_t) is defined as $B_{\max} L$, where B_{\max} is the maximum binding sites per lipid molecule, and L is the total lipid concentration. Substituting $P_t = P_f + PB_b$ and $B_t = B_f + PB_b = B_{\max} L$ into the expression for K_a^{app} and using the definition of B_t , we obtain:

$$K_a^{app} = \frac{PB_b}{(P_t - PB_b)(B_{\max} L - PB_b)}. \quad (3.2)$$

Rearranging this equation yields:

$$PB_b^2 - (B_{\max} L + P_t + \frac{1}{K_a^{app}})PB_b + P_t B_{\max} L = 0. \quad (3.3)$$

Since our CD data ($\Delta[\Theta]_{222 \text{ nm}}$) is proportional to $\frac{PB_b}{P_t}$, Eq. 3 can be solved for our

fitting equation (3.4) and used to extract B_{\max} as well as K_a^{app} :

$$\Delta[\Theta]_{222nm} = \frac{1}{2P_t} \left(B_{\max} L + P_t + \frac{1}{K_a^{app}} - \sqrt{\left(B_{\max} L + P_t + \frac{1}{K_a^{app}} \right)^2 - 4P_t B_{\max} L} \right) \quad (3.4)$$

Fitting was performed using IGOR Pro 6.01 (Wavemetrics).

3.2.9 Protein Packing on Lipid Vesicles

The number of lipid molecules per vesicle was estimated by dividing total vesicle surface area by the area per lipid molecule parallel to the bilayer surface. A total of 56,795 lipid molecules per vesicle was calculated using 40 nm for outer vesicle radius, 0.643 nm² for the lipid area (estimated using DPPC), and 3.86 nm for the bilayer thickness.^{165,166} This number is consistent with that predicted from the molecular weight of a hydrated vesicle.¹⁶⁷ Estimation of the maximum number of α -synucleins binding to vesicles was calculated by modeling the proteins as rigid bodies of dimensions consistent with α -syn in continuous extended-¹⁴⁸ (14.97 nm) and bent-helical^{142,143} (approximate segment lengths: helix 1 = 5.5 nm, linker = 1.4 nm, helix 2 = 6.8 nm) conformations. Using a value of 0.75 nm for the protein-helix diameter, we estimate an area of 11.3 nm² and 10.3 nm² is required for α -syn to bind in bent-helical and extended-helical conformations, respectively. Maximum α -synuclein packing number on a vesicle using B_{max} (maximum number of protein binding sites per lipid molecule) were calculated considering that only the lipid molecules on the outer leaflet of the vesicle (~31,300) are available for protein binding. Percent surface coverage was calculated using the maximum total of protein sites extracted from B_{max} .

3.2.10 Computer Simulation

Computer simulations used to approximate α -syn vesicle binding saturation numbers considered only geometrical packing constraints. Proteins were modeled as rigid bodies of dimensions consistent with those for α -syn in continuous extended- (14.97 nm) and bent-helical (approximate segment lengths: 5.5 nm helix 1, 1.4 nm linker, 6.8 nm helix 2) conformations. Saturation number was determined when 10,000 successive attempts to randomly place simulated proteins on a sphere of fixed radius were unsuccessful.

3.3 Results and Discussion

3.3.1 Membrane-mediated α -Helical Structure Formation

To monitor site-specific interactions of α -syn membrane binding, four single tryptophan-containing proteins (F4W, Y39W, F94W, and Y125W) were produced. CD spectroscopy was employed to assess the effects of the Trp mutations and to characterize vesicle-induced secondary structural changes for all α -synucleins. In pH 7.4 buffer solutions (10 mM NaPi, 100 mM NaCl, 25 °C), CD spectra for wild-type and Trp variants (3 – 5 μ M) exhibit a dominant minimum near 200 nm that is consistent with random coil configurations. With increasing amounts of anionic phospholipid vesicles (equal molar POPA, anionic –1 per headgroup, and POPC, zwitterionic) the CD spectra show prototypical features (negative maxima at 208 and 222 nm) for α -helical structure (Figure 3.2).

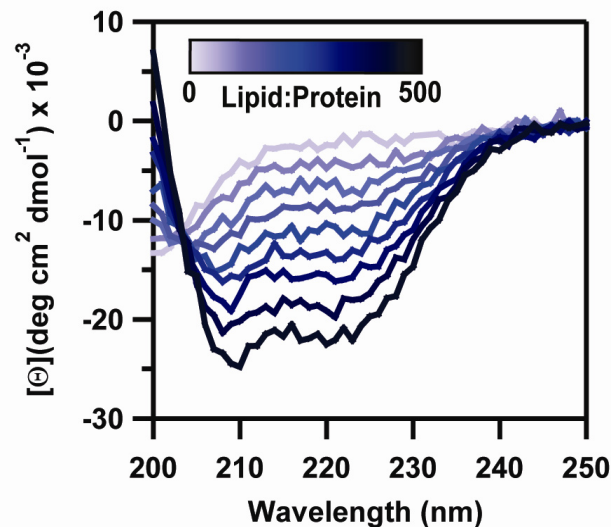


Figure 3.2 Phospholipid vesicles induced secondary structure in α -synuclein. Representative far UV CD spectra of Y39W α -syn ($5 \mu\text{M}$) as a function of increased lipid vesicles (0 – 2 mM 1:1 POPA:POPC in 10 mM NaP_i , 100 mM NaCl buffer at pH 7.4, 25°C).

The spectra for the Trp mutants were indistinguishable from the wild-type protein, indicating that this naturally occurring fluorophore does not change the secondary structure of vesicle-bound protein under these solution conditions. An isodichroic point (204 nm) suggests that binding is consistent with an unstructured to α -helical conformation transition with a maximum total α -helical content of $\sim 67\%$ (mean residue ellipticity at 222nm, $[\Theta]_{222 \text{ nm}} = -23,130 \text{ deg cm}^2 \text{ dmol}^{-1}$), consistent with previously reported values.¹¹⁶ Similarly, all α -syn variants exhibit an α -helical content of $\sim 67\%$ in the presence of SDS micelles, demonstrating not only that substitution of Trp residues does not perturb micelle-bound structure, but also that α -helical content is not a distinguishing feature between vesicle- and SDS micelles-bound α -syn (Figure 3.3).

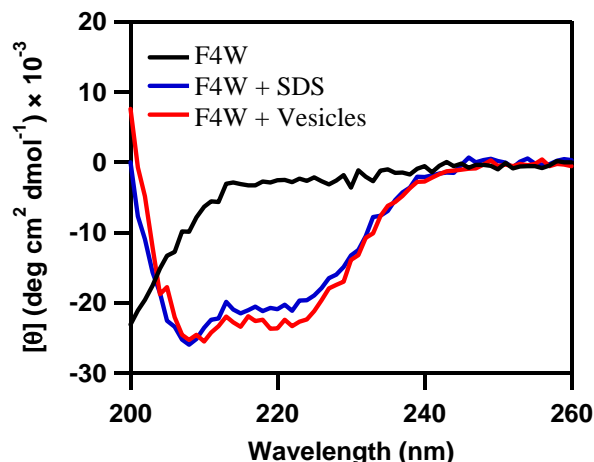


Figure 3.3 Phospholipid vesicle and sodium dodecyl sulfate (SDS) micelles induced secondary structure in α -synuclein. Representative CD spectra of F4W α -syn (5 μ M α -syn in 10 mM NaPi, 100 mM NaCl buffer at pH 7.4, 25°C) (black) and with the addition of SDS micelles (40 mM) (blue) and lipid vesicles (2 mM 1:1 POPA:POPC) (red).

As α -syn has substantially reduced affinity for zwitterionic vesicles,¹⁶⁸ 100% POPC vesicles (at highest lipid concentration \sim 2 mg/mL) were employed to assess macromolecular crowding effects. No apparent conformational transitions were observed for wild-type and Trp mutants verifying the involvement of electrostatic interactions in membrane binding affinity (Figure 3.4).

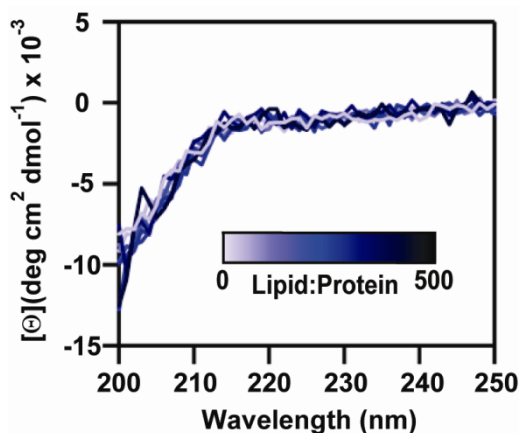


Figure 3.4 Effect of zwitterionic vesicles on α -synuclein membrane binding. Representative far UV CD and steady-state fluorescence emission spectra of F4W α -syn (5 μ M) as a function of increased lipid vesicles (0 – 2 mM POPC in 10mM NaPi, 100 mM NaCl buffer at pH 7.4, 25 °C).

Membrane binding curves were generated for all proteins using mean residue ellipticity (Figure 3.5). All isotherms are nearly identical and reversible, with similar midpoint transitions (lipid-to-protein molar ratio of 120 – 160) approaching saturation at a lipid-to-protein molar ratio of ~380. Interestingly, while α -synuclein membrane binding curves generated from calorimetric¹¹³ and single molecule fluorescence¹⁶⁸ techniques are not well described by membrane-partition models, adequate fits to CD data using a law of mass action for identical independent binding sites were achieved.^{163,164} An apparent association constant ($K_a^{app} \sim 1 \times 10^7 \text{ M}^{-1}$) and a total number of binding sites per lipid molecule ($B_{max} \sim 0.004$) were extracted for all α -synucleins. To ensure that K_a^{app} values derived from CD data were independent of bound polypeptide concentration in the low lipid-to-protein regimes, inverse fluorescence titrations also were performed in which protein concentration was varied (1 – 20 μM) while lipid concentration (1 mM) was maintained (Figure 3.6).^{16,156}

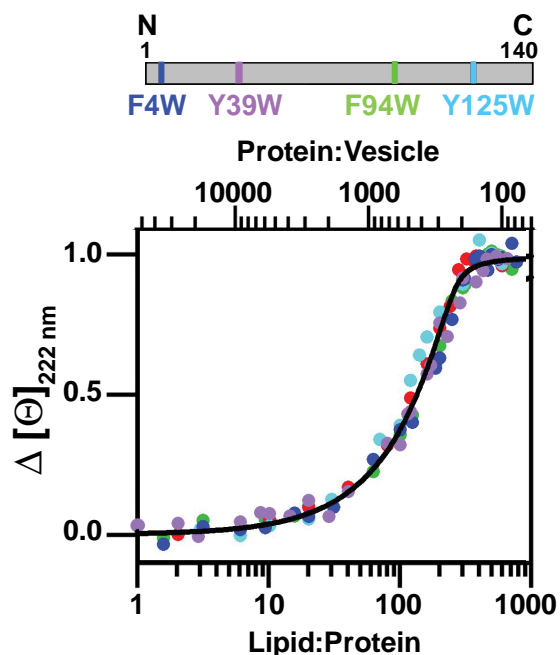


Figure 3.5 Comparison of vesicle binding properties of wild-type and fluorescent single Trp α -synucleins. (Top) Schematic representation of α -synuclein primary sequence with the tryptophan mutations (F4W, Y39W, F94W, and Y125W) highlighted. (Bottom) Normalized change in mean residue ellipticity ($\Delta[\Theta]$) as a function of lipid-to-protein (bottom axis) as well as an estimated protein-to-vesicle (average diameter ~ 80 nm) ratio (top axis) (0 – 2.5 mM 1:1 POPA:POPC in 10 mM NaP_i , 100 mM NaCl buffer, pH 7.4, 25°C) for wild-type(\bullet), W4(\bullet), W39(\bullet), W94(\bullet), and W125 (\bullet) variants. A representative fit is shown as a line.

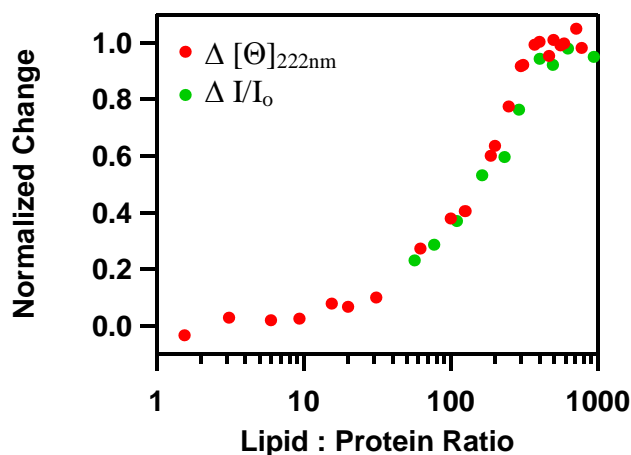


Figure 3.6 Inverse fluorescence lipid titration of F4W α -synuclein. Representative comparison of F4W α -syn membrane binding curves derived from CD ($\Delta[\Theta]_{222 \text{ nm}}$) and from inverse fluorescence titrations $\Delta I/I_0$, where I is the integrated fluorescence intensity and I_0 is the initial fluorescence intensity of protein alone).

Because α -syn membrane binding likely is affected by electrostatic repulsion of the acidic C-terminal tail, our K_a^{app} values are unexpectedly similar to several full length apolipoproteins (apoPs) (apoA-I and apoE4 (egg PC), $K_a^{app} = 8.3 \times 10^5$ and $8.3 \times 10^6 \text{ M}^{-1}$, respectively).^{163,169} While K_a^{app} values for α -syn suggest comparable affinity as the apoPs, we would anticipate an isolated N-terminal amphiphilic α -syn polypeptide would bind to membranes even more tightly. Furthermore, the full length α -syn membrane affinity would be expected to increase in solution conditions favoring charge neutralization (acidic pH) and the binding of biomolecules or metal ions such as polyamines¹⁷⁰ and calcium ions¹⁰³ to the C-terminus.

3.3.2 Estimation of α -Synuclein Vesicle Surface Coverage

Using CD binding curves the possible role of membrane surface coverage in modulating α -syn conformation was assessed. Assuming that only outer leaflet lipids bind proteins and using B_{max} obtained from fits, we find that the vesicle surface contains ~120 protein binding sites with ~250 lipids per binding site. If all binding sites are occupied, only ~7% of the total vesicle surface would be covered by proteins (see Materials and Methods). Simple geometrical estimates of the total possible number of α -syn proteins bound to vesicles in both bent- and extended-helical conformations are higher than our experimentally derived value (~1000 and ~650 respectively). These disparities likely are attributable to repulsive electrostatic protein-protein and even phospholipid-protein interactions with the acidic C-terminus. Our data suggest that α -syn proteins are not closely packed on the membrane surface at binding saturation; this result is consistent with electron spin

resonance data (36 – 100 lipids per protein; DMPG).¹⁷¹ Interestingly, the surface coverage determined for α -syn is low compared to other peripheral membrane proteins such as apocytochrome *c* (2 lipids per protein; DMPG)^{171,172} and myelin basic protein (18 lipids per protein; DMPG).^{171,173}

Notably, α -syn fibril formation in the presence of low lipids (lipid-to-protein molar ratio ~4) is ~3.5 times faster than protein alone.¹¹⁹ For this case, we estimate a staggering ~14,000 proteins-per-vesicle; a value significantly higher than the maximum binding sites per vesicle. While our data suggest that α -syn proteins are not closely packed at saturation, it is plausible that changing the lipid-to-protein ratio could result in conformational rearrangement at the vesicle surface, a phenomena observed in apocytochrome *c*.¹⁷² Because intracellular synaptic vesicles contain heterogeneous distributions of phospholipid headgroups and membrane-associated proteins, the biological relevance of the conformational rearrangement of α -syn due to protein packing remains to be elucidated.

3.3.3 Site-specific Tryptophan Probes of α -Synuclein Membrane Interactions

Site-specific interactions of α -syn with phospholipid vesicles were monitored by measuring steady-state and time-resolved Trp fluorescence as a function of POPA:POPC vesicle concentration (0 – 2.5 mM in 10 mM NaP_i, 100 mM NaCl buffer at pH 7.4). In solution, all four Trp residues exhibit identical fluorescence maxima at 348 nm consistent with water-exposed side chains and similar local protein conformations. The model complex, N-acetyl-tryptophanamide also has a maximum at 348 nm under similar solution conditions. However, upon addition of phospholipid vesicles, Trp photophysical properties become site-dependent with differences in the

emission maxima (F4W > F94W ~ Y39W >> Y125W, Figure 3.7 and Figure 3.8) and quantum yields (F4W ~ F94W > Y39W >> Y125W, Figure 3.7). In particular, F4W exhibits a pronounced spectral blue shift ($\Delta\lambda_{\text{max}} = 23$ nm) reminiscent of integral (*E. Coli* outer membrane protein A (OmpA): $\Delta\lambda_{\text{max}} = 25\text{--}28$ nm, DMPC)^{50,51} rather than surface-bound membrane proteins (mimics of the class A1 helices in exchangeable apoPs: $\Delta\lambda_{\text{max}} = 14$ nm, POPC).⁹⁸ In addition, the three fold increase in W4 quantum yield is consistent with this side chain partitioning into the bilayer. While this residue was initially predicted to be membrane exposed using SDS micelles studies,¹⁴² it was not characterized in the α -syn vesicle-bound EPR structure (residues 9-89).¹⁴⁸

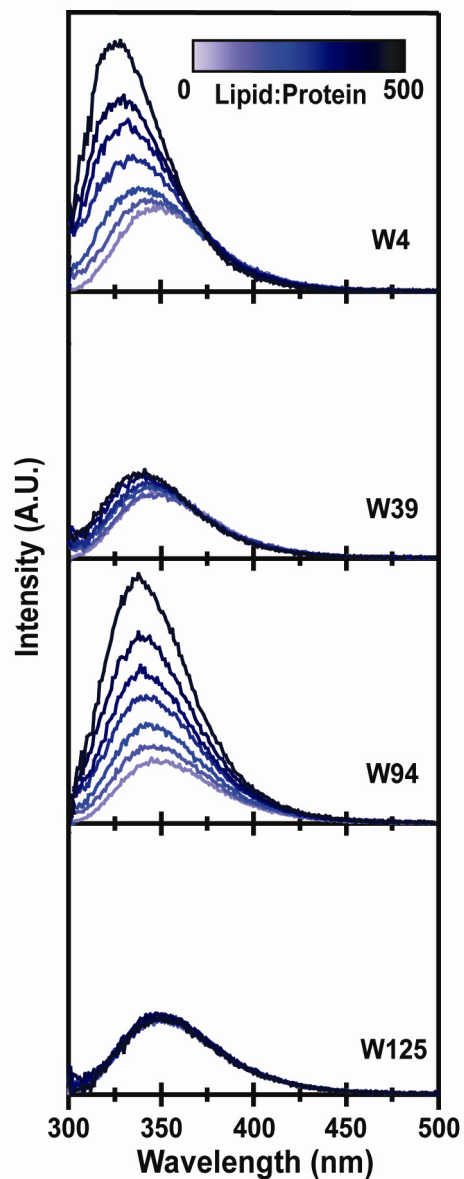


Figure 3.7 Site-specific tryptophan fluorescence of α -synucleins. Steady-state emission spectra of F4W, Y39W, F94W, and Y125W (top to bottom) α -syn mutants in the presence of lipid vesicles (0-2.5 mM 1:1 POPA:POPC in 10mM NaP_i, 100 mM NaCl buffer, pH 7.4, 25 °C). For all steady-state spectra, lipid vesicle backgrounds were collected and subtracted for each vesicle concentration.

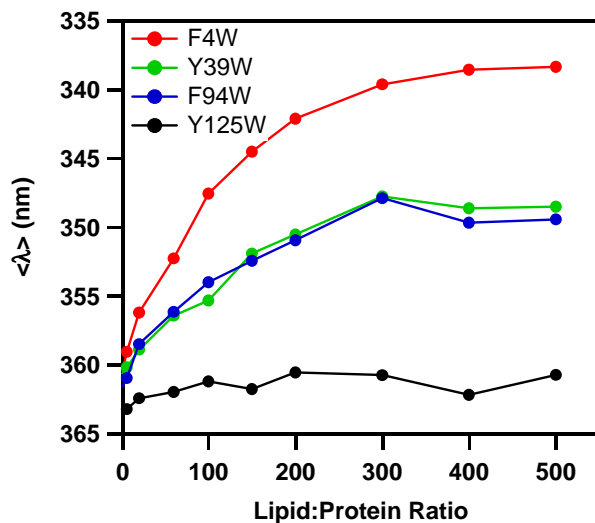


Figure 3.8 Mean wavelength of Trp α -synucleins as a function of lipid vesicles. Mean wavelength of spectral distribution, $\langle \lambda \rangle$, for F4W, Y39W, F94W, and Y125W α -synucleins (5 μ M) as a function of increased lipid vesicles (1:1 POPA:POPC in 10mM NaP_i, 100 mM NaCl buffer at pH 7.4, 25 °C), where $\langle \lambda \rangle = \frac{\sum \lambda_i I_i}{\sum I_i}$, and λ and I are wavelength and intensity, respectively.

In contrast, W39, which is located in the loop region of the micelle-bound NMR structure¹⁴² and water-exposed in the SUV-bound conformation,¹⁴⁸ exhibits a modest spectral blue shift ($\lambda_{\max} \sim 339$ nm, $\Delta\lambda_{\max} \sim 10$ nm) and QY increase (1.2 fold) in the presence of vesicles. These reduced Y39W fluorescence changes compared to that of F4W point to greater water exposure, consistent with proposed micelle and liposome bound conformations. Located in the C-terminal end of the NAC region, F94W exhibits a similar emission spectral shift as Y39W ($\lambda_{\max} \sim 338$ nm $\Delta\lambda_{\max} \sim 9$ nm), but a significant QY increase (comparable to W4) upon vesicle binding suggesting that this indole is lipid-exposed or in a conformation that alleviates nonradiative pathways (*e.g.* restriction of mobility and electron transfer). The pronounced spectral response of F94W to membranes is particularly interesting and somewhat unexpected because this residue is predicted to be solvent exposed^{141,145,148}

and, while micelle facing, is unstructured when bound to SDS.¹⁴² It is important to note that Trp fluorescence quantum yields are modulated by local charges as well as fluorophore mobility.⁵² If the indole ring is in close proximity to a positive (negative) charge then its quantum yield could increase (decrease). It is plausible as the protein binds to the membrane surface, W94 may become closer to K96, the closest intramolecular positive charge. Alternatively, W94 may reside near the trimethylammonium cation of the POPC headgroup. Not surprisingly, Y125W fluorescence remains unchanged in the presence of phospholipid vesicles confirming that the C-terminal tail remains in solution. Although Y125W is unresponsive, it provides a control to ensure that our spectroscopic changes are solely due to protein-membrane interactions and not the mere presence of the membranes themselves. To further verify that the emission features were not a result of macromolecular crowding, the spectra of all Trp variants in the presence of zwitterionic POPC vesicles were obtained. No changes were observed even at the highest vesicle concentrations (Figure 3.9).

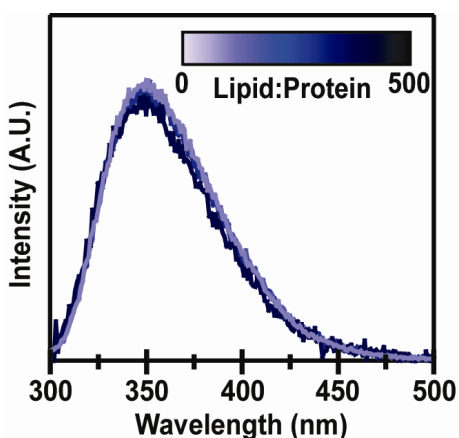


Figure 3.9 Effect of zwitterionic vesicles on α -synuclein membrane binding. Representative steady-state fluorescence emission spectra of F4W α -syn (5 μ M) as a function of increased lipid vesicles (0 – 2 mM POPC in 10mM NaP_i, 100 mM NaCl buffer at pH 7.4, 25 °C).

Because secondary structural characterization does not provide a distinguishing marker of micelle- vs. vesicle-bound proteins (Figure 3.3), Trp fluorescence data also were collected for SDS micelles-bound α -synuclein (Figure 3.10). In all positions except W125, Trp data reveal significant differences for vesicle- and SDS micelles-bound conformations. The F4W spectrum in the presence of SDS micelles (40 mM, critical micelle concentration = 1.33 mM¹⁷⁴ (100 mM NaCl, 25°C)) exhibits a QY decrease (20% decrease compared to in solution) and the spectral shift is greatly reduced ($\Delta\lambda_{\max} = 23$ (vesicles) \rightarrow 15 (micelle) nm). The reduced QY suggests considerable differences in the local polypeptide conformation near the vicinity of residue 4. The reduced spectral shift also supports different protein-lipid interactions (head group vs. hydrocarbon chain) as well as variations in micellar vs. bilayer microenvironment hydration. Interestingly, in the presence of SDS micelles, Y39W also exhibits a decrease in QY which may be due to its proximity to a Trp quencher, such as His50, the most likely side chain in the amino acid sequence to participate in excited-state deactivation processes (there is no native Cys and only one His).¹⁵⁴ Examination of the SDS structure (PDB 1XQ8)¹⁴² reveals that the nearest negative charges (E35) is over 15 Å away and the nearest positive charge (K45) is much closer (8 Å) to Y39. Because these side chains are relatively distant, likely it is the proximity of W39 to the sulfonate groups that is responsible for the reduced quantum yield (*vide supra*). In contrast, W94 appears to be the most sensitive probe for micelle interaction with both a spectral shift and an increase in quantum yield, qualitatively similar to that of the bilayer. Not surprisingly, the

Y125W spectrum remains unchanged, indicating that both micelle- and vesicle-bound conformers have C terminal regions that remain solvent exposed.

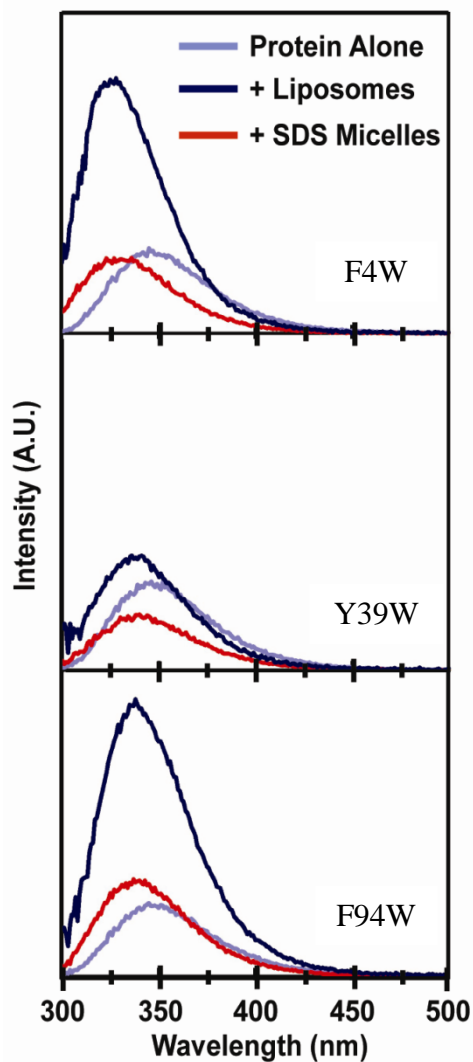


Figure 3.10 Comparison of tryptophan fluorescence for micelles- and liposome-bound α -synuclein. Steady-state emission spectra for F4W, Y39W, and F94W (top to bottom) in buffer (10mM NaP_i, 100 mM NaCl, pH 7.4) (light blue), bound to SDS micelles (40 mM) (red), and at saturating SUV concentrations (2.0 – 2.5 mM 1:1 POPA:POPC) (blue).

Our steady-state fluorescence data clearly demonstrate site-specific differences for the SDS micelle and liposome-bound α -syn conformers. While the trends in spectral shifts are consistent between micelle- and liposome-bound

conformations, the quantum yields reveal distinct behavior, particularly highlighting the local polypeptide environmental changes of W4. Notably, W4 and W94 were not characterized in the continuous α -helical (residues 9 – 89) membrane-associated structure reported by Langen and coworkers.¹⁴⁸ If we use the periodicity of $3.6\bar{6}$ aa per turn from Langen¹⁴⁸ and previous NMR studies on micelles,¹⁴⁵ then W4 and W94 are predicted to be lipid- and solvent-exposed, respectively. Since our data demonstrate that both W4 and W94 partition into the bilayer, we suggest that this α -helical periodicity ($3.6\bar{6}$ aa per turn) spans from residues 4 to 89 and is not extended to position 94. However, the strong spectral response we observe for W94 does suggest that this residue interacts directly with the micelle. Taken together, our vesicle and micelle data support that there are more protein-membrane interaction sites beyond helical regions.

3.3.4 Conformational Heterogeneity of Phospholipid Vesicles-bound α -Synuclein Monitored by Tryptophan Kinetics

To characterize membrane-bound protein conformational heterogeneity we measured tryptophan decay kinetics for F4W, Y39W, F94W, and Y125W α -synucleins (Figure 3.11). For all variants and solution conditions, decay kinetics are not well described by single exponential functions as it is typically observed for Trp-containing proteins attributable to side chain local environments and conformations.^{44,153,154,157} Accordingly, we used a nonnegative linear least squares method to analyze our data which produces the narrowest probability distribution of lifetimes ($P(\tau)$) required to fit the decay kinetics and distinguish protein subpopulations (see Figure 3.12 for residuals).⁴⁷ Our time-resolved data are

consistent with steady-state observations (F4W and F94W: increases in average fluorescence lifetime ($\langle\tau\rangle$); Y39W: modest changes in $\langle\tau\rangle$; Y125W: no changes, Figure 3.11). Notably, the $P(\tau)$ extracted from our fits provided insights in the evolution of subpopulations in the protein ensemble and revealed local conformational heterogeneity that was not apparent through steady-state analyses.

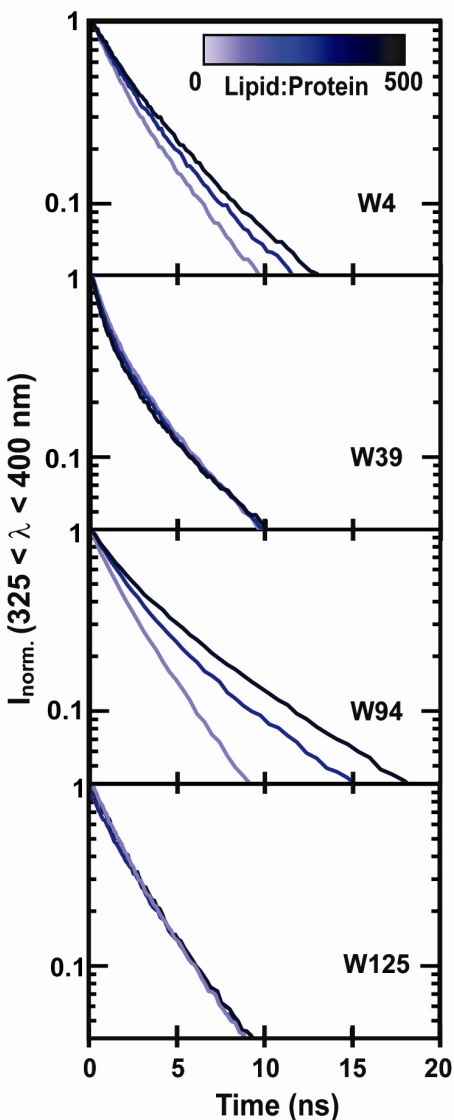


Figure 3.11 Time-resolved Trp fluorescence decay kinetics of F4W, Y39W, F94W, and Y125W (top to bottom) α -syn mutants in the presence of lipid vesicles (1:1 POPA:POPC (midpoint and saturated concentrations: 0.5 mM and 2.0 mM respectively) in 10 mM NaPi_i, 100 mM NaCl buffer, pH 7.4, 25 °C).

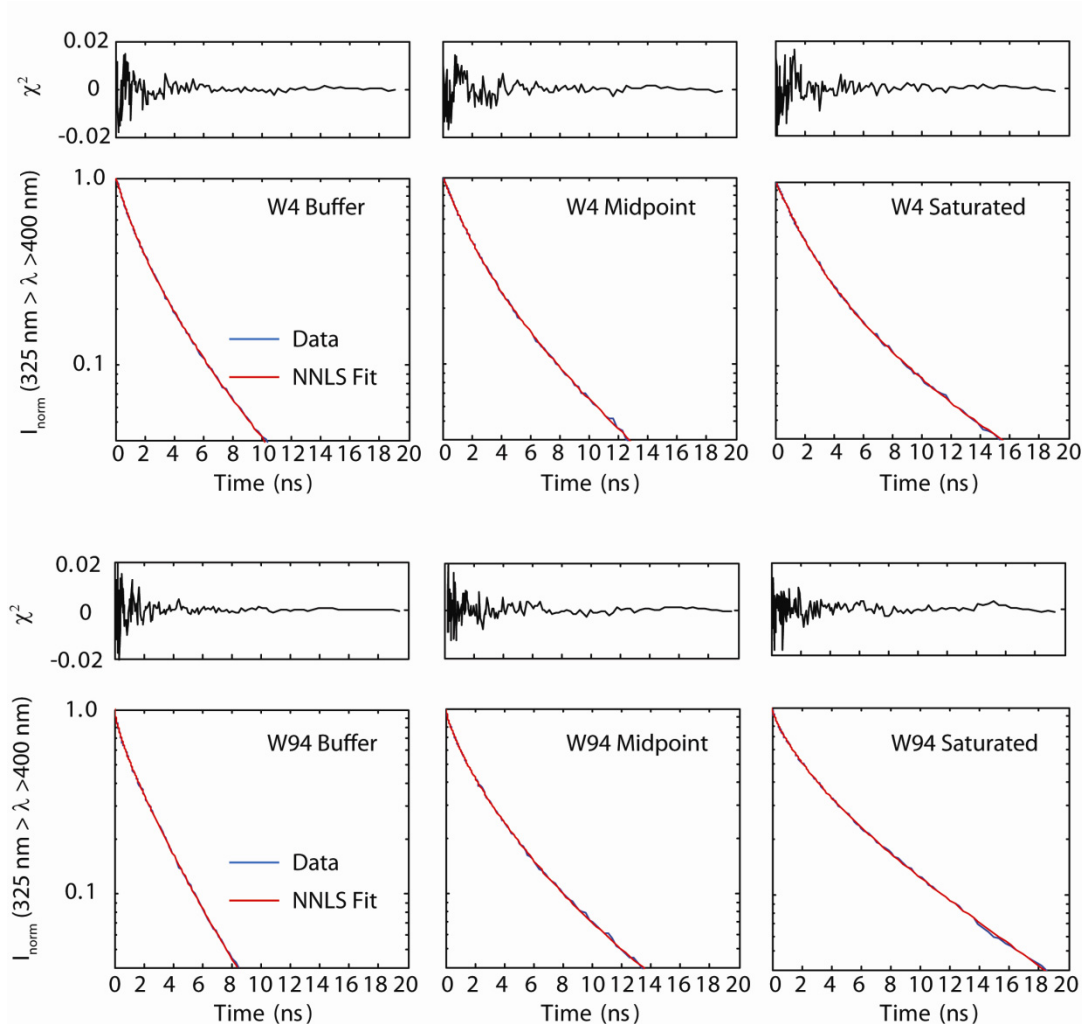


Figure 3.12 Non negative least squares fitting of Trp decay kinetics. Logarithmically compressed (100 points per time decade) and normalized ($I(t=0)=1$) fluorescence decays (blue) with corresponding NNLS fits (red) and fitting residuals (black) for W4 (top) and W94 (bottom) α -synucleins in buffer (10 mM NaPi, 100 mM NaCl, pH 7.4, 25°C) (left) and at midpoint (middle) and saturated (right) concentrations of 1:1 POPA:POPC (0.5 mM and 2.0 mM respectively).

In solution (10 mM NaPi, 100 mM NaCl, pH 7.4), two ($\langle\tau_1\rangle = 3.0$ ns, $P(\tau_1) = 57\%$; $\langle\tau_2\rangle = 1.0$ ns, $P(\tau_2) = 43\%$) and three ($\langle\tau_1\rangle = 4.2$ ns, $P(\tau_1) = 24\%$; $\langle\tau_2\rangle = 2.1$ ns, $P(\tau_2) = 59\%$; $\langle\tau_3\rangle = 0.5$ ns, $P(\tau_3) = 17\%$) distinct populations were observed for W4 and W94, respectively (Figure 3.13). For both W4 and W94, vesicle-bound decays generally are characterized by increases in average lifetimes as a function of

added vesicles; however, the evolution of the individual lifetimes is distinct for W4 and W94. Upon vesicle addition, W4 exhibits characteristic $\langle\tau\rangle$ increases ($\langle\tau_1\rangle$: 3.0 ns \rightarrow 5.7 ns; $\langle\tau_2\rangle$: 1.0 ns \rightarrow 1.7 ns) with only modest changes in relative amplitudes ($P(\tau_1)$: 57% \rightarrow 41%; $P(\tau_2)$: 43% \rightarrow 59%). These average lifetime increases are consistent with those that have been observed for folding of single-Trp containing OmpA into DMPC SUVs (τ_1 : 4.5 – 5.5 \rightarrow 5.3 – 6.3 ns; τ_2 = 1.5 – 1.8 \rightarrow 2.1 – 2.7 ns (urea \rightarrow DMPC)).⁵⁰ The small relative amplitude changes in $P(\tau)$ coupled to increases in both $\langle\tau_1\rangle$ and $\langle\tau_2\rangle$ suggest that all F4W subpopulations are sensitive to the presence of the bilayer. Similar to W4, two W94 subpopulations change with vesicle addition; however, F94W kinetics reflect an increased conformational heterogeneity not observed in F4W. While both τ_1 and τ_2 increase in average lifetime ($\langle\tau_1\rangle$: 4.2 ns \rightarrow 7.7 ns; $\langle\tau_2\rangle$: 2.1 ns \rightarrow 2.7 ns) indicative of a membrane-bound conformations, the relative amplitude of τ_2 is appreciably decreased in favor of τ_1 ($P(\tau_1)$: 24% \rightarrow 40%; $P(\tau_2)$ 59% \rightarrow 41%) suggesting a conformational transition that is dependent on lipid-to-protein ratio. The presence of a third component τ_3 that exhibits no significant changes in $\langle\tau\rangle$ or $P(\tau)$ even at saturating lipid concentrations in addition to the change in $P(\tau_3)$ is suggestive of a unbound subpopulation. However, because τ_3 represents $< 25\%$ of the total distribution and τ_2 exhibits only a modest lipid induced lifetime increase, the exact nature of this heterogeneity is not clear. The presence of an unbound subpopulation would not be surprising because of the electrostatic repulsion due to the acidic C-terminus in this region. Alternatively, because the Trp excited state captures nanosecond snapshots of

the protein ensemble, heterogeneity observed in W94 could reflect side chain dynamics.

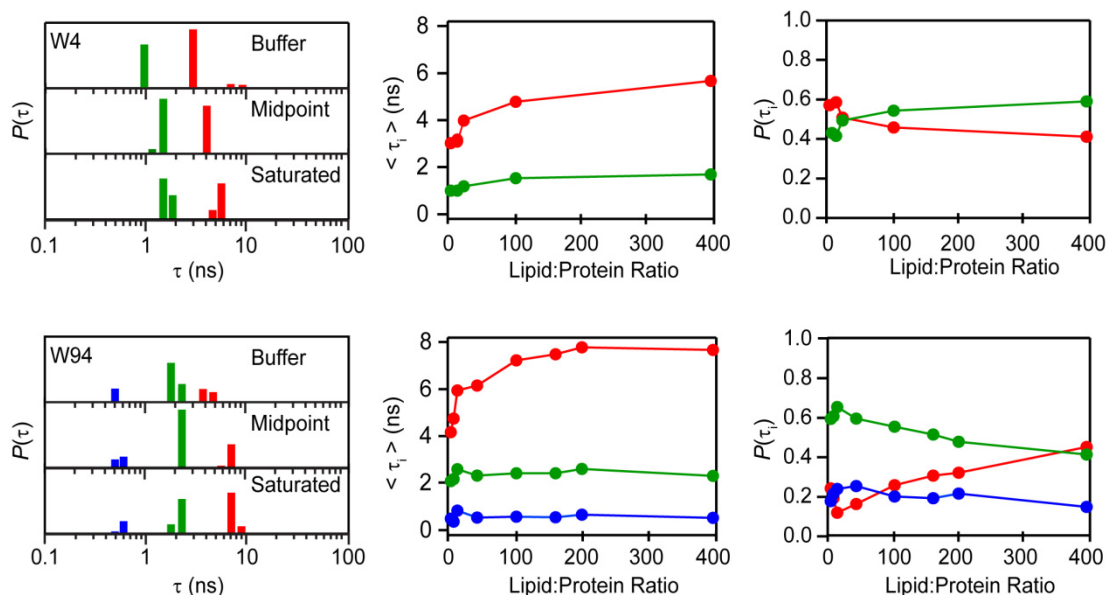


Figure 3.13 Analysis of time-resolved Trp fluorescence decay kinetics for α -synucleins. Representative probability distribution of fluorescence lifetimes ($P(\tau)$) extracted from NNLS fits for F4W (top) and F94W (bottom) α -synucleins in buffer (10 mM NaP_i , 100 mM NaCl, pH 7.4, 25 °C) and at midpoint and saturated concentrations of 1:1 POPA:POPC (0.5 mM and 2.0 mM respectively) (left), variations in individual average lifetimes ($\langle \tau_i \rangle$) (middle) and the development of individual lifetime populations ($P(\tau_i)$) (right) as a function of added lipids.

While assignment of distinct populations is challenging due to the smaller dynamic range for changes in Y39W, inspection of the kinetics do reflect a conformational heterogeneity similar to that of F94W (data not shown). Although the W39 decays accelerate only modestly, there is a consistent development of shorter lifetime components from buffer to vesicle-containing solutions which is atypical for lipid-associated changes. It appears that upon membrane binding, there may be quenchers in closer proximity to W39 as a result of local conformational changes

(*vide supra*). Finally, consistent with steady-state results, Y125W decay kinetics are not affected to the presence of vesicles even at saturating lipid conditions.

Time-resolved analyses demonstrate that all sites examined (except W125) have interactions with the membrane. Particularly, our data suggest that W4 is a high affinity membrane binding site with increases in average lifetimes for all components; it appears that W4 kinetics are sensitive to the presence of vesicles even at low lipid concentrations (100 μM , $[\text{lipid}]_{\text{midpoint}} = 500 \mu\text{M}$). Though exhibiting only modest changes, residue W39 does exhibit conformational heterogeneity with increases in average lifetime with vesicle addition. Our Y39W data agree with both micelle- and liposome-bound structures in that this residue is likely both solvent-exposed and flexible at the interface of the lipid headgroups and the surrounding solvent. While F94W steady-state results show a spectral response comparable to that of F4W, F94W kinetics data also reveal conformational heterogeneity for this position with vesicle addition. The local conformational change between the solvent-to-lipid or different lipid-bound states is evidenced in the lipid concentration dependent decrease in $P(\tau_2)$ in favor of $P(\tau_1)$. F94W data could indicate that protein-membrane stoichiometry is crucial in modulating membrane interactions in this region of the protein. Moreover, W4 could act as an anchor with all populations sensitive to the membrane at all lipid concentrations, while W94 has both lipid and solvent exposed conformers that are dependent on lipid-to-protein ratio. It is noteworthy that the hydrophobic NAC region has been proposed to be secluded from intermolecular contacts by the intra-molecular N- and C-terminal interactions.¹⁷⁵ Similarly, it is feasible for membrane stimulated aggregation to arise because as the local protein

concentration increases at the surface, polypeptide conformational rearrangement ensues leading to exposure of potential protein-protein interaction sites promoting amyloid formation.

3.4 Summary

We have demonstrated that Trp fluorescence is a sensitive, site-specific probe of α -syn interactions with both vesicles (QY: F4W \sim F94W $>$ Y39W \gg Y125W; $\langle\lambda\rangle$: F4W $>$ F94W \sim Y39W \gg Y125W) and micelles (quantum yield: F94W $>$ F4W $>$ Y125W $>$ Y39W; $\langle\lambda\rangle$: F4W $>$ F94W \sim Y39W \gg Y125W). Vesicle-binding curves generated from steady-state CD and fluorescence data can be described by a two-state equilibrium partition model with $K_a^{app} \sim 1 \times 10^7 \text{ M}^{-1}$. We estimate that α -syn binds to POPA:POPC vesicles with a relatively low surface coverage $\sim 7\%$ (~ 120 proteins for a 80 nm diameter vesicle) at saturation. Furthermore, measurements of fluorescence decay kinetics reveal the presence of protein conformational heterogeneity in the bilayer, suggesting that the both W4 and W94 exhibit high membrane affinity. Notably, both of these sites have not been characterized previously in the vesicle-bound α -syn structure.¹⁴⁸ With this approach, the crucial protein-to-membrane conditions and key sites of interaction that promote membrane-mediated protein aggregation can be elucidated.

Chapter 4: Molecular Insights of N-terminal α -Synuclein at the Membrane Interface*

4.1 Introduction

Though substantial biophysical research efforts have provided insights into the interaction of α -syn with model membranes, a molecular understanding of the role of specific key residues in mediating membrane binding is still unclear. However, recent fluorescence,¹⁰² NMR,³⁹ and isothermal titration calorimetry¹⁷⁶ studies point toward the importance of N-terminal residues. The biological relevance of the N-terminus of α -syn in membrane binding is underscored by a recent report using *Saccharomyces cerevisiae* as a cellular model system in which α -syn induced cell toxicity is mediated by the presence of N-terminal residues; deletion of even one amino acid (D2) in this region can significantly enhance cell viability.¹⁷⁷

Biophysical evidence from site-specific fluorescence and NMR data indeed suggest that vesicles-bound α -syn conformation is dependent on α -syn-to-lipid stoichiometry and that high affinity N-terminal residues could serve as a protein-membrane anchor under certain low lipid solution conditions.^{39,102} Based on the disappearance of solution NMR signals, two distinct binding modes were characterized, SL1 and SL2, corresponding to the association of the first 25 and 97 residues, respectively. As the lipid-to-protein ratio is increased, decreases in the ratio

* Thanks to Alex Maltzev (Laboratory of Chemical Physics, NIDDK) for collecting NMR data, Ad Bax (Laboratory of Chemical Physics, NIDDK) for the use of the NMR spectrometer, and Grzegorz Piszczek (Biophysics Facility, NHLBI) and Duck-Yeon Lee (Biochemistry Core Facility, NHLBI) for technical assistance.

of the SL1 to SL2 binding mode were observed. Evidence for the presence of multiple-membrane bound conformations also can be found in time-resolved tryptophan fluorescence data showing increased heterogeneity near the C-terminal site, W94, compared to that of the N-terminal probe, W4.¹⁰² The idea that different regions of α -syn can associate with the membrane under different solution conditions is further corroborated by a recent study of the role of the N-terminus in α -syn membrane binding.¹⁷⁶ In this study, it was found that different isolated regions of the α -syn sequence bind to membranes to various degrees and that secondary structural formation for each of these regions is dependent on lipid composition as well as other factors such as temperature.¹⁷⁶ This study further suggests that the N-terminus, specifically the first 25 residues, is involved in the membrane induced polypeptide folding.¹⁷⁶

In this chapter, a range of experimental tools are used to identify the role of N-terminal residues in membrane binding. Specifically, the spectroscopic properties of a series of synthetic W4 containing peptides: residues 1 – 4 (P4), 1 – 6 (P6), 1 – 10 (P10), and 1 – 15 (P15) ([Figure 4.1](#)) are measured to determine a minimal N-terminal amino acid sequence to preserve phospholipid vesicle binding. Furthermore, we examine how membrane binding is modulated by the presence of the consensus amphipathic repeat (residues 11 – 15; P15), the addition of lysine residues, K6 (P6) vs. K10 (P10), and the shortest sequence (P4) required for our fluorescent studies. Trp4 is used because it has been demonstrated to be a particularly sensitive reporter of polypeptide environments and conformational changes in the presence of biomolecules such as lipids¹⁰² or copper.¹⁵⁹ Moreover, W4 is a minimalist probe that

does not significantly affect membrane binding properties in the full length protein¹⁰² or in the P15 peptide (*vide infra*) as evidenced by CD spectroscopy (CD) and 1-dimensional (1D) ¹H NMR, respectively. CD and 1-D ¹H NMR also were measured to assess the role of other (non-fluorescent) residues in secondary structural formation and membrane interactions, respectively. To determine the penetration depth of the W4 into the bilayer as a function of polypeptide length, phospholipids in which specific sites in the phospholipid acyl-chain region are labeled with the heavy-atom fluorescence quencher bromine, were employed.

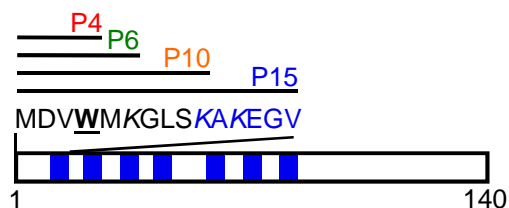


Figure 4.1 Schematic representation of full-length α -synuclein with the seven amphipathic amino acid imperfect repeat regions (KXKEGV) highlighted (blue). The sequence for N-terminal peptides is also given with the single tryptophan site (W4; bold and underlined) and lysine residues (italics) highlighted.

4.2 Materials and Methods

4.2.1 Materials

Phospholipids (1-palmitoyl-2-oleoyl-*sn*-glycero-3-phosphate (POPA), 1-palmitoyl-2-oleoyl-*sn*-glycero-3-phosphocholine (POPC), 1-palmitoyl-2-(6,7-dibromo)stearoyl-*sn*-glycero-3-phosphocholine (Br₆₋₇PC), 1-palmitoyl-2-(9,10-dibromo)stearoyl-*sn*-glycero-3-phosphocholine (Br₉₋₁₀PC) and 1-palmitoyl-2-(11,12-dibromo)stearoyl-*sn*-glycero-3-phosphocholine (Br₁₁₋₁₂PC)) were purchased from Avanti Polar Lipids (Alabaster, AL) and used as received. N-acetyl-tryptophanamide

(NATA) was obtained from Sigma-Aldrich (St. Louis, MO). Synthetic C-terminally amidated peptides (>95% purity) were purchased from Anaspec, Inc. (San Jose, CA) and D₂O from Cambridge Isotopes Laboratory (Andover, MA).

4.2.2 Recombinant Protein Expression and Purification

Wild-type (WT) and F4W α -syn were expressed and purified as previously reported.¹⁰² Protein concentration was determined using a molar extinction coefficient estimated on the basis of amino-acid content: $\epsilon_{280\text{ nm}} = 5,120\text{ M}^{-1}\text{cm}^{-1}$ and $10,810\text{ M}^{-1}\text{cm}^{-1}$ for WT and F4W, respectively. The purity of protein samples was assessed by SDS-PAGE on a Pharmacia Phastsystem (Amersham Biosciences) and visualized by silver-staining methods. The protein molecular weights were confirmed by electrospray ionization mass spectrometry (Biochemistry Core Facility, NHLBI). All purified proteins were concentrated using a YM-3 filter (MWCO 3kD, Millipore) and stored at $-80\text{ }^{\circ}\text{C}$.

4.2.3 Phospholipid Vesicle Preparation

Phospholipid vesicles were made from a 1:1 molar ratio of POPA and POPC. For Trp penetration depth experiments, brominated-PC lipids (BrPC: Br₆₋₇PC, Br₉₋₁₀PC, and Br₁₁₋₁₂PC) were added to a final molar concentration of 30% while maintaining an overall 1:1 molar ratio of PA and PC. Chloroform solutions of 1:1 POPA and POPC or 1:1 POPA and POPC/BrPC were dried under a nitrogen stream for 20 min followed by vacuum desiccation for 45 min to ensure complete removal of organic solvent. Dried samples were then resuspended in 10 mM NaPi, 100 mM NaCl buffer, pH 7.4 to a final concentration of 5 mg/mL by bath sonication for 5 – 10

min. Vesicles were prepared *via* ultrasonication in a water bath (45 minutes, 50% duty cycle, microtip limit, Branson 450 Sonifier). Vesicle solutions were diluted to a final concentration of 2.5 mg/mL, equilibrated overnight (14 – 24 h) at 37 °C, and prepared freshly for each experiment. Average vesicle hydrodynamic radius was determined to be 45 – 55 nm by dynamic light scattering (Wyatt DynaPro NanoStar; fifty 5-s acquisitions, 25 °C).

4.2.4 Steady-state Spectroscopic Measurements

Spectroscopic measurements were made as follows: absorption, Cary 300 Bio spectrophotometer; CD, Jasco J-715 spectropolarimeter (205 – 260, 1 nm steps, 1 nm bandwidth, 0.5 s integration time, and 50 nm/min, 5 mm cuvette pathlength), and luminescence, Fluorolog-3 spectrofluorimeter ($\lambda_{\text{ex}} = 295$ nm, $\lambda_{\text{obs}} = 300 - 500$ nm, 0.25 s integration time, 1 and 2 nm excitation and emission slit widths, respectively). All measurements were collected at 25 °C using temperature controlled cuvette holders except for absorbance experiments. For all spectra measured in the presence of vesicles, background scans were collected and subtracted. Though CD spectra for most samples was collected between 200 and 260 nm, due to the high scattering associated with high vesicle concentrations, CD data between 205 and 260 nm is presented herein. Prior to all experiments, F4W α -syn was exchanged into 10 mM NaPi, 100 mM NaCl, pH 7.4 buffer using a PD-10 column (GE Healthcare).

All α -syn N-terminal peptides (P4, P6, P10, P15 and the 1 – 15 wild type sequence) had the C-terminus amidated and were used as received. Stock peptide solutions were prepared in deionized H₂O prior to dilution to the desired final concentration. A molar extinction coefficient $\epsilon_{280 \text{ nm}} = 5,500 \text{ M}^{-1}\text{cm}^{-1}$ was used to

estimate peptide concentration for P4, P6, P10, and P15. For the 1 – 15 wild-type peptide, protein concentration was determined by measuring the mass of lyophilized stock prior to dilution. All protein and peptide solutions containing vesicles were incubated for at least 30 min at RT prior to measurement. For Trp quenching experiments, a phospholipid-to-protein/peptide molar ratio of 300 (1.5 mM phospholipid) was used. Under these conditions, all peptides are at binding saturation with the exception of P6 and P4.

4.2.5 Circular Dichroism Spectroscopy

Mean residue ellipticity, $[\Theta]$ ($\text{deg cm}^2 \text{ dmol}^{-1}$), was calculated according to the equation, $[\Theta] = \frac{100\theta}{clN}$ where θ is the measured ellipticity (mdeg), c is the sample concentration (mM), l is the path length (cm), and N is the number of amino acids.

Percent α -helicity ($100f_{helix}$) was calculated using $f_{helix} = \frac{([\Theta]_{222} - [\Theta]_{coil})}{([\Theta]_{helix} - [\Theta]_{coil})}$, where

$[\Theta]_{helix} = -40,000(1 - \frac{2.5}{N}) + 100T$ and $[\Theta]_{coil} = 640 - 45T$, and T is the temperature in $^{\circ}\text{C}$.¹⁷⁶

4.2.6 ^1H Nuclear Magnetic Resonance Spectroscopy

1D ^1H NMR experiments were performed on 10 μM α -syn peptide samples (P4, P6, P10 and P15) in the absence (10 mM NaPi, 100 mM NaCl, pH 7.4; 2.6% D_2O) and presence of 1:1 POPA:POPC phospholipid vesicles (lipid-to-protein molar ratio of 300, 3 mM POPA:POPC). Measurements were made using a Bruker DMX-600 spectrometer operating at 600 MHz hydrogen frequency and equipped with a RT

probe. For each experiment 32,000 scans were acquired over the course of 15 h with acquisition time of 70 ms and the spectral width of 12 ppm. Sample temperature was set to 25 °C.

4.2.7 Time-resolved Fluorescence Anisotropy

Tryptophan fluorescence anisotropy decay kinetics were measured using the fourth harmonic (292 nm) of a regeneratively-amplified femtosecond Ti:sapphire (Clark-MXR) pumped optical parametric amplifier laser (Light Conversion) as an excitation source (80 – 120 μ W, 1 kHz) and a picosecond streak camera (Hamamatsu C5680) in photon counting mode for detection. Tryptophan emission between 325 and 400 nm was selected through edge (REF-325) and short-pass (UG-11) filters (CVI Laser). Polarized Trp excited state decays ($I_{\perp}(t)$ and $I_{\parallel}(t)$) were measured simultaneously with an optical fiber array and corrected for differences in collection efficiency of vertically and horizontally polarized light using the Trp model complex, NATA. Fluorescence anisotropy decays were calculated according to:

$$r(t) = \frac{I_{\parallel}(t) - \alpha(t)I_{\perp}(t)}{I_{\parallel}(t) + 2\alpha(t)I_{\perp}(t)} \quad (4.1)$$

where $r(t)$ is the apparent anisotropy at time t and $\alpha(t)$ is the ratio of the polarized emission, $\frac{I_{\parallel}(t)}{I_{\perp}(t)}$, of NATA. Prior to measurement, all protein and peptide samples (5 μ M in 10 mM NaPi, 100 mM NaCl buffer, pH 7.4) and samples containing vesicles (lipid-to-protein molar ratio of 300, 1.5 mM POPA:POPC) were deoxygenated on a Schlenk line by 3 sets of 5 repeated evacuation/Ar fill cycles over 30 min. All buffer solutions were filtered (0.22 μ m membrane) to remove any particulate matter. A

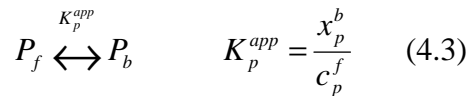
collection temperature of 25 °C was maintained using a temperature controlled cuvette holder. To ensure good signal to noise, all kinetics data were collected such that at least 10,000 counts were achieved in the highest channel for each polarization. Our instrument response time is ~150 ps and uncertainty in r_0 is ~0.02. Steady-state fluorescence spectra were measured before and after time-resolved anisotropy experiments to verify minimal photodamage. Anisotropy decays were analyzed according to the following equation,

$$r(t) = r_0 e^{(-t/\phi_c)} \quad (4.2)$$

where r_0 is the apparent anisotropy at $t = 0$ and ϕ_c is the rotational correlation time resulting from depolarization.

4.2.8 Peptide-membrane Equilibrium

α -Syn peptide and F4W membrane binding data were modeled according to the following two-state equilibrium, a partitioning of the polypeptide between the free and membrane-bound state:



where P_f and P_b are the free and bound protein states, respectively, K_p^{app} is the apparent partition constant, x_p^b is the mole fraction of bound protein, and c_p^f is the concentration of the free protein. The mole fraction of bound protein is given by

$x_p^b = \frac{c_p^b}{c_L^o}$ where c_p^b is the total bound protein and c_L^o is the total lipid concentration.

Substitution of x_p^b and $c_p^f = c_p^o - c_p^b$, where c_p^o is the total protein concentration, into eq. (4.3) yields:

$$K_p^{app} = \frac{c_p^b}{(c_p^o - c_p^b)c_L^o} \quad (4.4).$$

As changes in Trp mean wavelength, $\langle \lambda \rangle$ are proportional to $\frac{c_p^b}{c_p^o}$, eq. 4.4 can be solved, yielding an equation amenable to data fitting:

$$\langle \lambda \rangle = \frac{K_p^{app} c_L^o}{1 + K_p^{app} c_L^o} \quad (4.5),$$

with $\langle \lambda \rangle$ determined according to:

$$\langle \lambda \rangle = \frac{\sum_i I_i \lambda_i}{\sum_i I_i} \quad (4.6).$$

Here, I_i and λ_i are the emission intensity and wavelength, respectively, for $i = 325 - 400$ nm. To account for the fact that only lipids in the outer monolayer are available for protein association, K_p^{app} is replaced by $0.6K_p^{app}$. Data fitting was performed using IGOR Pro (Wavemetrics). Gibbs free energy was calculated according to:

$$\Delta G = -RT \ln(55.5 K_p^{app}) \quad (4.7),$$

where 55.5 is the molarity of water.

4.3 Results and Discussion

4.3.1 Membrane Affinities and Gibbs Free Energies for N-terminal Peptides and Full Length α -Synuclein

The amino acid sequence of P15 (MDVWMKGLSKAKEGV) contains three lysine residues, as well as one of seven imperfect amphipathic amino acids repeats (KXKEGV) that are reminiscent of amphipathic sequences found in membrane binding exchangeable apoPs.^{83,178} The propensity for the isolated P15 polypeptide to associate and to adopt α -helical secondary structure upon membrane interaction can be rationalized by the preference of lysine residues (K6, K10, and K12) to flank the anionic PA headgroups creating an interface between water-exposed, charged residues (D2 and E13) and lipid-facing, nonpolar residues (V3, W4, G7, L8, A11, and V14). Indeed, N-terminal α -syn residues 6 – 15 are predicted by NMR chemical shift mapping to have a preference for α -helical formation.¹⁴⁰ The shorter peptides studied, P4, P6, and P10, contain zero, one, and two lysines, respectively. Though P10 is predicted to form an α -helix based on primary structure analysis,¹⁷⁹ P4 and P6 do not. Regardless of the exact conformations adopted, herein we assess the probability of these peptides to partition into the bilayer.

To address the possibility that N-terminal residues could serve as membrane anchors, we compared the fluorescence properties from single Trp (W4) containing N-terminal α -syn peptides (P4, P6, P10, and P15) as a function of varying concentrations of phospholipid vesicles (0 – 2.5 mM POPA:POPC in 10 mM NaPi, 100 mM NaCl buffer at pH 7.4) to that of the full length protein (F4W) (Figure 4.2). W4 is an excellent probe of protein-bilayer interactions because not only is the indole side-chain exquisitely responsive to local environment and conformation,^{153,154,156,157} but has been established as a high affinity membrane binding site in the full length protein.¹⁰²

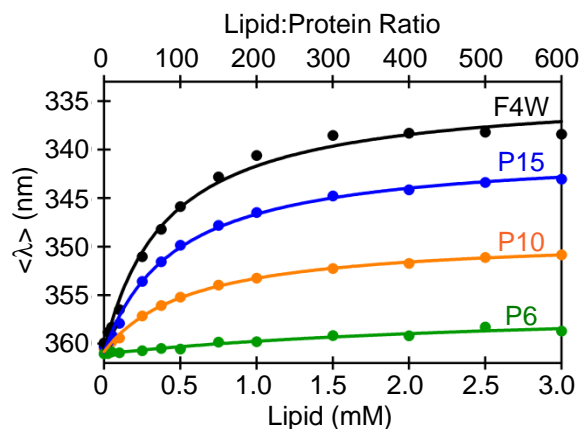


Figure 4.2 Comparison of vesicle binding of single Trp containing full-length α -syn (F4W) and N-terminal peptides. Mean wavelength ($\langle \lambda \rangle$) as a function of lipid-to-protein ratio (5 μ M α -syn polypeptides, 0 – 3 mM 1:1 POPA:POPC in 10 mM NaPi, 100 mM NaCl buffer, pH 7.4, 25 $^{\circ}$ C) for F4W (black) and α -syn residues 1 – 15 (P15; blue), 1 – 10 (P10; orange), 1 – 6 (P6; green) fragments. Fits to membrane partition equilibrium model are shown as solid lines.

Prior to vesicle addition, the steady-state fluorescence spectra for all peptides and the full-length protein (5 μ M polypeptide in 10 mM NaPi, 100 mM NaCl buffer at pH 7.4) are similar with mean wavelengths ($\langle \lambda \rangle$) consistent with a water-exposed Trp side-chain ($\langle \lambda \rangle = 361$ nm; for the model complex, NATA, $\langle \lambda \rangle = 365$ nm). However, in the presence of vesicles, spectral changes are observed as a function of polypeptide length reflecting different environments for the W4 side-chain (Figure 4.2). Specifically, for P6, P10, and P15, increases in integrated intensity (I) and spectral blue shifts (P15 > P10 > P6) suggest increased side-chain rigidity as W4 interacts with the hydrophobic membrane interior (Table 4.1). In contrast, even in the presence of high vesicle concentrations (2.5 mM POPA:POPC), no significant change in mean wavelength ($\langle \lambda \rangle = 361$ nm) or integrated intensity were observed in the P4 peptide indicating minimal deviations in the W4 microenvironment. Changes in I (~2.0 fold increase) and $\langle \lambda \rangle$ (17 nm blue shift) for P15 are highly reminiscent of the

full length protein (~2.0 fold increase, 22 nm blue shift) highlighting that the association of the first 15 residues result in similar W4 microenvironments for the two polypeptides.

Table 4.1 Steady-state Trp4 spectral and equilibrium vesicle binding properties for full-length and N-terminal α -syn peptides.

Peptide	α -Helicity ^a	$\langle\lambda\rangle_{\text{aqueous}}$ (nm) ^b	$\langle\lambda\rangle_{\text{lipid}}$ (nm) ^c	I_{rel} (a.u.) ^d	K_p^{app} (M ⁻¹) ^e	ΔG (kcal/mol) ^f
P4	NA	363	365	1.0	n.d.	n.d.
P6	NA	361	359	1.2	600	-6.3
P10	< 15%	361	351	1.9	2900	-7.1
P15	~56%	360	343	1.7	3600	-7.2
Full length (F4W)	~67% ¹⁰²	360	338	1.9	4100	-7.3

^a Percent α -helical content at vesicle saturation was determined from circular dichroism (mean residue ellipticity at 222 nm ($[\Theta]_{222\text{nm}}$)) of polypeptides (10 μM in 10 mM NaPi, 100 mM NaCl buffer at pH 7.4). For P10, saturating α -helical content was approximated from $[\Theta]_{222\text{nm}}$ at high vesicle concentration (2 mM). For P15, $[\Theta]_{222\text{nm}}$ lipid titrations were fit according to membrane-partition equilibrium (eq. 4.3) to determine the percent α -helical content at vesicle saturation. Multiple independent measurements of $[\Theta]$ for polypeptides ($n \geq 2$) were compared to ensure reproducibility. For example, at a lipid-to-protein ratio of 75, $[\Theta]_{222\text{nm}}$ for P15 is $-6290 \text{ deg cm}^2 \text{ dmol}^{-1}$ with a standard deviation of ± 10 ($n = 2$).

^b Steady-state W4 fluorescence mean wavelength ($\langle\lambda\rangle$) for polypeptides (5 μM in 10 mM NaPi, 100 mM NaCl buffer at pH 7.4). $\langle\lambda\rangle$ was determined according to the eq. 4.6. Error in $\langle\lambda\rangle$ due to instrument fluctuations is estimated to be ± 1 nm.

^c $\langle\lambda\rangle$ for polypeptides in the presence of 1:1 POPA:POPC vesicles (5 μM peptide and 3 mM 1:1 POPA:POPC in 10 mM NaPi, 100 mM NaCl buffer at pH 7.4).

^d Relative emission intensity, I_{rel} , is given by the following equation: $I_{\text{rel}} = \frac{I_{\text{lipid}}}{I_{\text{aqueous}}}$, where I_{lipid} and

I_{aqueous} are the integrated steady state emission spectrum (325 – 400 nm) of α -syn polypeptides in the presence of vesicles (3 mM 1:1 POPA:POPC) and in buffer (5 μM in 10 mM NaPi, 100 mM NaCl buffer at pH 7.4), respectively.

^e Apparent membrane partition constants (K_p^{app} , M⁻¹) extracted from fits to steady-state fluorescence data using eq. 4.5. Fitting error in K_p^{app} is estimated to be $\sim 500 \text{ M}^{-1}$.

^f Gibbs free energies (ΔG) is calculated using eq. 4.7. Propagated error in ΔG (kcal/mol) is ± 0.1 for F4W, P15, and P10 and ± 0.5 for P6.

Using $\langle\lambda\rangle$ data, we applied a membrane partition equilibrium model¹⁸⁰ to extract apparent membrane partition constants (K_p^{app}) and Gibbs free energies (ΔG)

for F4W and N-terminal α -syn peptides (Table 4.1). Despite differences in absolute $\langle\lambda\rangle$, reflecting variations in W4 microenvironments, both K_p^{app} and ΔG values for both P10 and P15 were quite similar to that of the full length protein ($K_p^{app} = 4100$, 3600, and 2900 M^{-1} ; $\Delta G = -7.3$, -7.2 , and -7.1 kcal/mol for full length α -syn, P15, and P10, respectively). However, in the case of P6, we observe substantial decreases in K_p^{app} and ΔG (600 M^{-1} and -6.3 kcal/mol). In general, the measured free energies for all variants are comparable to those of membrane associating peptides (~ -2.3 to -8.9 kcal/mol).¹⁸⁰ While the ΔG difference for P6 and P10 (ΔG (P6 \rightarrow P10) = -0.8) is consistent with the addition of one lysine in P10 (contributes approximately -1 kcal/mol due to favorable electrostatic sidechain-head group interactions),¹⁸¹ the difference between P10 and P15 is very small (ΔG (P10 \rightarrow P15) = -0.1 kcal/mol) even though P15 also contains one extra lysine. Moreover, ΔG of P15 is comparable to that of the full length protein (ΔG (P15 \rightarrow F4W) = -0.1 kcal/mol).

To examine the possible effect of secondary structure formation (*i.e.* random coil \rightarrow α -helix) on free energy differences, CD spectra were collected for the P10 and P15 peptides in the absence and presence of varying concentration of lipid vesicles (10 μ M polypeptide and 0 – 2.5 mM POPA:POPC in 10 mM NaPi, 100 mM NaCl buffer at pH 7.4). Interestingly, at saturating vesicle concentrations, less than 15% α -helical content is present for P10 as compared to $\sim 56\%$ in the case of P15 (Figure 4.3). It is plausible that enhancement in ΔG resulting from the addition of K12 in P15 is counterbalanced by some losses in entropy resulting from helical structural formation. Moreover, a similar ΔG value for P15 and the full length protein indicate

that the individual amphipathic repeats (there are seven in total) can act as independent binding sites and one repeat alone may provide enough stabilization for membrane association. This suggestion is supported by work demonstrating that other, isolated α -syn polypeptides can indeed also bind to membranes.^{114,176} Regardless of the exact contributions to free energy changes, the CD results demonstrate the importance of the full amphipathic repeat sequence, KAKEGV, in α -helical formation. Using CD data, K_p^{app} values were determined for P15 and the full-length protein ($K_p^{app} = 1600 \text{ M}^{-1}$ and 2000 M^{-1} , respectively). These K_p^{app} values are a factor of two smaller than those extracted from fluorescence data, indicating that Trp4 partitions into the bilayer prior to the development of secondary structure.

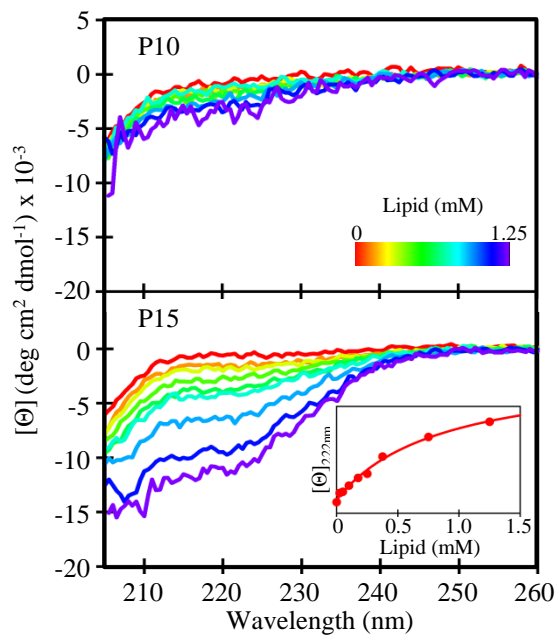


Figure 4.3 Vesicle induced secondary structural formation of P10 and P15 peptides. Circular dichroism spectra for P10 (top) and P15 (bottom) (10 μM peptide, 10 mM NaPi, 100 mM NaCl buffer, pH 7.4, 25 $^{\circ}\text{C}$) as a function vesicle addition (0 – 1.25 mM 1:1 POPA:POPC). (Inset) The P15 membrane binding curve generated from mean residue ellipticity ($[\Theta]$) at 222 nm. The fit to membrane partition equilibrium model is shown as a solid line.

Though previous work demonstrate that the W4 mutation does not modulate membrane induced secondary structural formation in full length α -syn,¹⁰² to ensure that the mutation also had a minimal effect in the case of the shorter peptides, additional CD experiments were conducted. Figure 4.4 shows the CD spectra for the P15 peptide (red) as well 1 – 15 wild type peptide (black) in the absence and presence of varying concentrations of vesicles (10 μ M peptide alone and in the presence of 0.2 and 0.5 mM 1:1 POPA:POPC vesicles in 10 mM NaPi, 100 mM NaCl buffer at pH 7.4). It is clear that both peptides indeed bind membranes as evidenced by increases in α -helical content in the presence of vesicles. Moreover, analogous 1D 1 H NMR experiments were also performed and confirm that the presence of the W4 does not perturb membrane binding properties (data not shown).

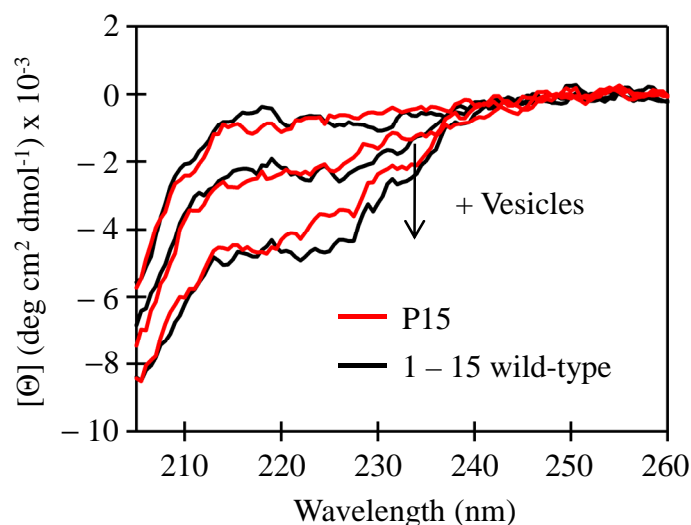


Figure 4.4 Comparison of vesicle induced secondary structural formation in the P15 and 1 – 15 wild-type peptides. Circular dichroism spectra for P15 (red) and the 1 -15 wild-type peptide (black) (10 μ M peptide, 10 mM NaPi, 100 mM NaCl buffer, pH 7.4, 25 $^{\circ}$ C) as a function vesicle addition (0, 0.2, and 0.5 mM 1:1 POPA:POPC).

4.3.2 Tryptophan Microenvironment at the Bilayer Interface

Further insights into Trp side-chain mobility and vesicle association as a function of polypeptide length were gained through time-resolved anisotropy experiments. In the absence of vesicles, all α -syn peptides and F4W (5 μ M polypeptide in 10 mM NaPi, 100 mM NaCl buffer at pH 7.4) exhibit small initial anisotropies ($r_o = 0.03 - 0.06$, instrument response time ~ 150 ps) with ns rotational correlation times ($\phi_C = 0.5 - 0.9$ ns) and zero residual anisotropy (r_∞) (Figure 4.5). These values are consistent with a solvent-exposed and freely rotating Trp side-chain. Upon vesicle addition (1.5 mM POPA:POPC), all peptides and F4W show significant increases in r_o , r_∞ , and ϕ_C , indicative of peptide-vesicle interaction and restriction in rotational freedom of W4 upon membrane association. In the presence of vesicles, r_o was greatest for F4W, followed by P15, P10, P6, and P4 (0.16, 0.14, 0.14, 0.11, and 0.09, respectively). Minimal decay from r_o was observed on the timescale of F4W fluorescence lifetime in the presence of vesicles ($\langle \tau \rangle = 3.6$ ns¹⁰²).

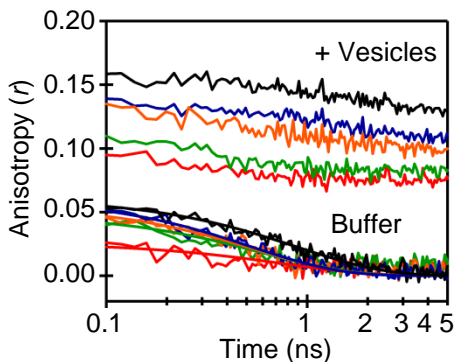


Figure 4.5 Effect of phospholipid vesicles on W4 time-resolved anisotropy of F4W and N-terminal peptides. Time-resolved anisotropy decays for F4W (black) and α -syn residues, 1 – 15 (P15; blue), 1 – 10 (P10; orange), 1 – 6 (P6; green), and 1 – 4 (P4; red) in the absence and presence of phospholipid vesicles (5 μ M α -syn polypeptides, 0 and 1.5 mM 1:1 POPA:POPC in 10 mM NaPi, 100 mM NaCl buffer, pH 7.4, 25 $^{\circ}$ C). Data represent the average of $n \geq 3$ measurements. Single exponential fits to anisotropy decays measured in solution are shown as solid lines.

While anisotropy data are in accord with steady-state fluorescence results indicating the membrane association of F4W, P15, P10, and P6, they reveal that P4 also is interacting with the vesicles. Particularly, increases in r_o and r_∞ upon vesicle addition show that P4 is part of a larger, vesicle-bound complex that has a slower tumbling time than P4 alone in solution. It is possible that a steady-state spectral shift was not observed because though P4 is bound, Trp4 does not embed into the hydrophobic environment of hydrocarbon chain. Furthermore, the expected increase in intensity upon restriction of the indole rotational motion could be offset by the fluorophore being in close proximity of the negatively charged head groups which would lead to a quantum yield decrease.⁵²

4.3.3 N-terminal Peptide Membrane Binding Probed by 1-Dimensional ¹H Nuclear Magnetic Resonance

1D ¹H NMR experiments were performed on P4, P6, P10, and P15 to evaluate the participation of all polypeptide residues in membrane association. [Figure 4.6](#) shows the 1D ¹H NMR data for polypeptide alone (10 μ M peptide, 10 mM NaPi, 100 mM NaCl, pH 7.4; 2.6% D₂O) and upon the addition of vesicles (lipid-to-protein molar ratio of 300, 3 mM POPA:POPC). All spectra of free peptides show characteristic tryptophan peaks in both the 7 – 7.75 ppm region (N-H bond) and around 10.1 ppm (aromatic H). We note that C-terminal amidation of the peptides resulted in appearance of two additional peaks in the 7 – 7.75 ppm region.

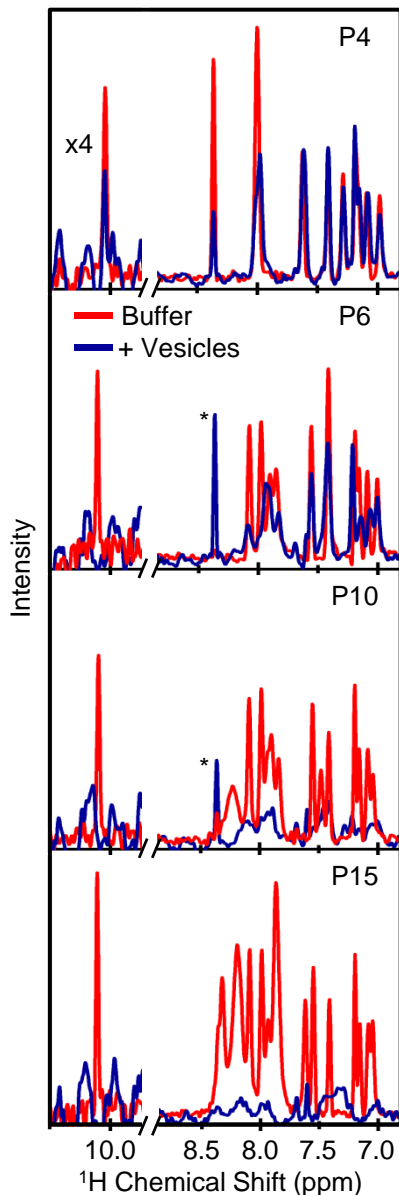


Figure 4.6 1D ^1H NMR spectra of N-terminal α -syn peptides. (Top-to-Bottom) NMR spectra for α -synuclein polypeptides, P4, P6, P10, and P15 for peptides alone (red) (10 μM peptide, 10 mM NaPi, 100 mM NaCl, pH 7.4; 2.6% D_2O) and upon the addition of vesicles (blue) (lipid-to-protein molar ratio of 300, 3 mM POPA:POPC). The sharp peak denoted by an asterisk at 8.37 ppm observed in some of the lipid-containing samples is attributable to a phospholipid contaminant. The intensity of Trp aromatic H region has been expanded for clarity.

Polypeptide length dependent changes in the NMR spectra are clearly apparent upon vesicle addition. In accordance with anisotropy data, P4 ^1H chemical

shifts change upon the addition of vesicles, demonstrating that indeed this peptide is vesicle-bound. The largest differences in peak heights are in the amide region indicative of association of the P4 peptide-backbones with the vesicles. Though it is evident that P4 is bound, observed changes are markedly reduced as compared to the other peptides, a result consistent with steady-state fluorescence data. In the case of P6, the whole spectrum is noticeably affected by the presence of vesicles. The broadening and shifting of all peaks suggest that the interaction is occurring in the fast-exchange regime and likely at all peptide sites. Similar, yet more pronounced, trends are observed for P10 and P15, with peaks broadened and disappearing upon vesicle binding. While it is difficult to definitively verify fast exchange for P15 due to poor signal-to-noise, our data indicate that P15 has a higher affinity for vesicles than P10.

4.3.4 Trp4 side-chain Bilayer Penetration

It is well established that the penetration of Trp residues into a lipid bilayer can be monitored *via* fluorescence quenching by molecules such as nitroxide or bromine that are incorporated at specific sites in the lipid hydrocarbon chain.⁵³⁻⁵⁶ To directly probe α -syn polypeptide-hydrocarbon interactions, we incorporated brominated lipids into vesicles and measured Trp fluorescence upon addition of F4W and single Trp containing α -syn fragments. We compared the steady-state fluorescence of W4 containing polypeptides in the absence and presence of vesicles containing 30% di-bromine-labeled POPC lipids at different sites in the fatty acid chain (5 μ M polypeptide and 1.5 mM POPA:POPC vesicles in 10 mM NaPi, 100 mM NaCl buffer at pH 7.4). [Figure 4.7A](#) shows representative steady-state and time-

resolved fluorescence data for P15 in the presence of 1:1 POPA:POPC vesicles (blue) and 1:1 POPA:POPC vesicles containing 30% Br₆₋₇PC (light blue). Relative quenching was comparable using both methods. Since fluorescence quenching will occur only when Trp is in close proximity (van der Waals contact) to a bromine,⁵³ insertion depths into the membrane can be estimated by using lipids labeled with bromine at different acyl-chain positions (Br₆₋₇PC, Br₉₋₁₀PC, and Br₁₁₋₁₂PC correspond to ~ 11 Å, 8.3 Å, and 6 Å above the bilayer center, respectively,¹⁸² [Figure 4.7B](#)).

The comparison of steady-state W4 fluorescence quenching from vesicles containing brominated lipids (I_{Br}) to unlabeled POPA:POPC vesicles (I_{Lipid}) for F4W and the P15, P10, P6, and P4 peptides is provided in [Figure 4.7C](#). Consistent with steady-state Trp fluorescence measurements, the P4 peptide fluorescence exhibits no significant quenching at all sites tested. While not precluding headgroup interactions, these data confirm that the Trp4 side-chain in P4 is not penetrating into the bilayer hydrocarbon core. In the presence of brominated lipids, decreases in P6 fluorescence are modest yet measurable ($I_{Br}/I_{Lipid} = 0.93 - 0.99$), indicating that at least a small fraction of membrane-bound P6 embeds into the hydrocarbon chain region. In contrast, with the addition of four more residues, including a lysine at position 10, substantial decreases in P10 Trp intensity are observed for all bromine positions. Though quenching at all bromine positions was observed (~ 6 – 11 Å above bilayer center), there is a predominance of conformations in which Trp4 is closer to the head group region as evidenced by modest increases in quenching: Br₆₋₇PC > Br₉₋₁₀PC > Br₁₁₋₁₂PC site ($I_{Br}/I_{Lipid} = 0.63 \pm 0.01, 0.67 \pm 0.02, \text{ and } 0.77 \pm 0.01$, respectively).

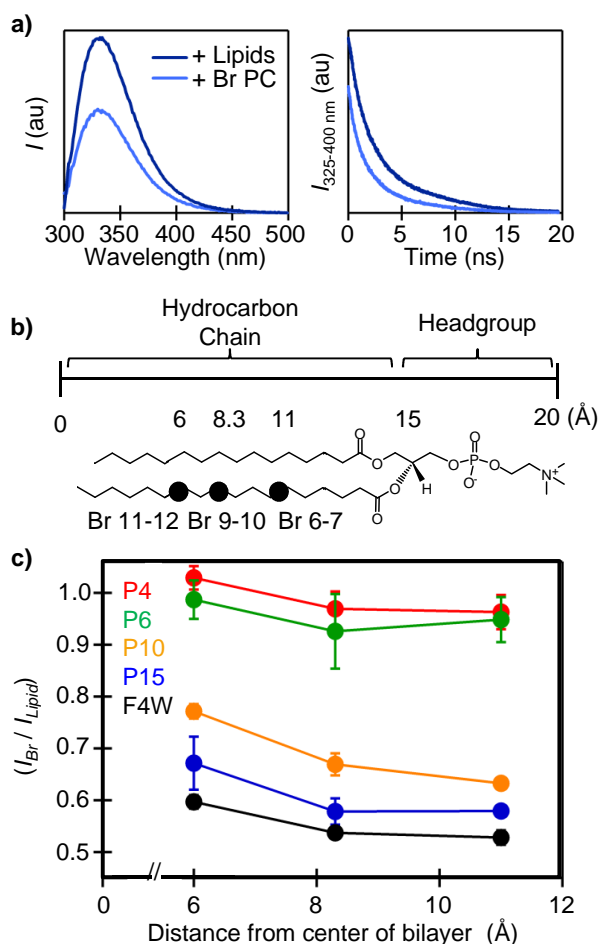


Figure 4.7 Tryptophan side-chain penetration into the vesicle bilayer. (a) Steady-state (left) and time-resolved (right) fluorescence of the P15 α -syn peptide (5 μM in 10 mM NaPi, 100 mM NaCl buffer, pH 7.4, 25 $^{\circ}\text{C}$) in the presence of 1:1 POPA:POPC vesicles (dark blue) and 1:1 POPA:POPC vesicles containing 30% bromine-labeled Br₆₋₇PC lipids (light blue) (5 μM in 10 mM NaPi, 100 mM NaCl buffer, pH 7.4, 25 $^{\circ}\text{C}$, lipid-to-protein molar ratio of 300). (b) Structure of PC phospholipid with positions of bromines highlighted. (c) Relative quenching of W4 steady-state fluorescence for F4W and N-terminal peptides (5 μM in 10 mM NaPi, 100 mM NaCl buffer, pH 7.4, 25 $^{\circ}\text{C}$) in the presence of 1:1 POPA:POPC vesicles containing 30% Br₆₋₇PC, Br₉₋₁₀PC, and Br₁₁₋₁₂PC (1.5 mM total lipid). Relative quenching is reported as I_{Br} / I_{Lipid} , where I_{Br} and I_{Lipid} is the integrated steady-state emission (325 – 400 nm) in the presence of vesicles containing and not containing brominated lipids, respectively. Error bars represent standard deviations ($n \geq 3$).

Similarly to P10, both P15 and the full-length protein exhibit significant quenching upon addition of brominated phospholipids. Though quenching is still

greatest in the presence of Br₆₋₇PC ($I_{Br}/I_{Lipid} = 0.58 \pm 0.01$, 0.53 ± 0.05 , for P15 and F4W, respectively), comparable quenching was observed in the presence of Br₉₋₁₀ ($I_{Br}/I_{Lipid} = 0.58 \pm 0.03$, 0.54 ± 0.01 , for P15 and F4W, respectively). Moreover, substantial quenching was also observed in the presence of Br₁₁₋₁₂PC ($I_{Br}/I_{Lipid} = 0.67 \pm 0.05$, 0.60 ± 0.01 , for P15 and F4W, respectively). These data highlight the importance of lysine residues in promoting peptide penetration into the membrane hydrocarbon region (full length > P15 > P10 >> P6 > P4). Taken together, our fluorescence and CD data demonstrate that the α -helical forming P15 could serve as a minimal model for N-terminal interactions as it nearly captures the properties of the full length protein.

4.4 Summary

Using multiple experimental methodologies, we have investigated the participation of specific N-terminal α -syn residues through the use of single Trp containing synthetic peptides. By comparing various spectroscopic properties of F4W to that of synthetic peptides, we find that the addition of lysine residues enhances membrane binding affinity (full length > P15 > P10 > P6 >> P4) and that at least one imperfect amphipathic repeat sequence (KAKEGV) is required for α -helical formation. While fluorescence spectral features of P4 do not indicate membrane association, both time-resolved anisotropy and 1D ¹H NMR reveal that indeed P4 can bind to vesicles albeit with much lower affinity compared to the other peptides. Time-resolved anisotropy and fluorescence quenching by brominated lipids further demonstrate that the molecular mobility and insertion of the Trp4 side-chain into the

bilayer, respectively, are also peptide length dependent with P15 nearly recapitulating the features of the full-length protein.

Our finding that the minimal sequence required for α -syn-membrane association is within the N-terminal fifteen residues could be of biological relevance. Because the surface of synaptic vesicles is crowded with numerous integral and peripheral membrane proteins, the lipid availability is greatly reduced and even considered “hardly visible”;¹⁸³ it is likely that α -syn would not be able to bind in a fully extended (residues 1 – 100) α -helical conformation as is the case of the α -syn-synthetic vesicle binding *in vitro*. The possible binding of an isolated N-terminal sequence of α -syn *in vivo* is further supported by recent work demonstrating that deletion of even one N-terminal amino acid can significantly enhance cell viability.¹⁷⁷ Moreover, the association of α -syn at the far N-terminus would allow for interactions with other biomolecules at more central and C-terminal protein sites. For example, it has been suggested that α -syn promotes SNARE complex assembly *via* N-terminal membrane association and C-terminal interaction with the SNARE protein, synaptobrevin.⁹⁴ Another recent example is the proposal that α -syn can interact with glucocerebrosidase in the lysosome where the N-terminal portion of the polypeptide is membrane bound and *via* its C-terminal tail associates with the enzyme.¹⁸⁴ Considering these recent works, future experiments using P15 as a minimal model of α -syn-phospholipid interaction site and natural membranes such as synaptic vesicles will allow us to gain residue level insights into its biological function.

Chapter 5: Structure of the α -Synuclein Membrane Interface: Insights from Neutron Reflectometry*

5.1 Introduction

Similar to electrons or x-rays, the interaction of neutrons with a material can provide pertinent structural information. Neutrons are particularly well suited for the study of biological materials because, unlike electrons and x-rays, neutrons have highly disparate scattering length densities (nSLD) for hydrogen and its isotope deuterium with de Broglie wavelengths on a molecular length scale ($\sim 5 \text{ \AA}$).⁶³ Thus, organic interface layers which contain different number of hydrogen atoms, such as the lipid head groups and hydrocarbons in a bilayer lipid membrane, can be readily distinguished using neutron reflectometry (NR).

In this chapter, results from experiments employing NR and a surface-stabilized sparsely tethered bilayer lipid membrane (stBLM)^{64,185} to examine α -syn membrane interactions are presented. Though membrane-bound α -syn has been the focus of substantial research efforts due to its likely involvement in PD pathogenesis,^{40,186} unlike other approaches, NR experiments provide the unique opportunity to simultaneously measure both membrane-bound protein structure as well as protein induced changes in membrane properties. Moreover, while oligomeric and fibrillar forms of α -syn have been shown to induce membrane

* Research was performed in part at the National Institute of Standards and Technology Center (NIST) for Nanoscale Science and Technology. Thanks to Frank Heinrich for overseeing neutron data collection and for performing data analysis, Grzegorz Piszczek (Biophysics Facility, NHLBI), Duck-Yeon Lee (Biochemistry Core Facility, NHLBI), and Ephrem Tekle (Laboratory of Biochemistry, NHLBI) for technical assistance, Thai Leong Yap for providing the dye labeled α -synuclein, and D. J. Vanderah (NIST) for synthesizing the HC18 tether molecule.

perturbations and even pore formation,¹⁸⁴ the high sensitivity of NR facilitates measurement of the effects of monomeric α -syn on membrane structure.

Using a stBLM composed of 1:1 molar ratio of 1-palmitoyl-2-oleoyl-*sn*-glycero-3-phosphate (POPA) and 1-palmitoyl-2-oleoyl-*sn*-glycero-3-phosphocholine (POPC) and NR, we find that α -syn associates with the membrane at both the head group and hydrocarbon chain region, extends into the bulk solvent, and also induces membrane thinning. In addition, NR was employed to elucidate the effects of α -syn concentration on protein and membrane structure. In these experiments, uniformly deuterated α -syn protein was used to ensure greatest contrast between the protein and the bilayer. Upon addition of different concentrations of α -syn, changes in protein volume occupancy in the headgroup/hydrocarbon and bulk solvent regions as well as degree of membrane thinning were observed. These results may be of physiological relevance because α -syn gene triplication⁷² and duplication⁷³ are linked to early onset PD and changing lipid-to-protein stoichiometry modulates α -syn aggregation kinetics *in vitro*.

5.2 Materials and Methods

5.2.1 Materials

Phospholipids (1-palmitoyl-2-oleoyl-*sn*-glycero-3-phosphate (POPA) and 1-palmitoyl-2-oleoyl-*sn*-glycero-3-phosphocholine (POPC)) were purchased from Avanti Polar Lipids (Alabaster, AL) and used as received. N-acetyl-tryptophanamide (NATA) and β -mercaptoethanol (β -ME) were obtained from Sigma-Aldrich (St. Louis, MO). D₂O was purchased from Cambridge Isotopes Laboratory (Andover,

MA) and tetramethylrhodamine-5-maleimide from Invitrogen. Polished [100]-Si wafers (75 mm in diameter) were obtained from EL-CAT Inc. (Waldwick, NJ).

5.2.2 Recombinant Protein Expression, Purification, and Labeling

Wild-type (WT), F4W, F94W, and A90C α -synucleins were expressed and purified as previously reported.¹⁰² For A90C, all lysis and purification buffers also contained 0.5 mM dithiothreitol (DTT) to prevent disulfide bond formation. Uniformly deuterated WT α -syn was expressed and purified according to previously reported procedures¹⁰² with minor modification. Cell pellet from 1 mL of starter culture in Luria Broth (LB) was resuspended in 20 mL minimal media¹⁸⁷ and incubated (30 °C, 165 RPM) overnight. Cell pellet was subsequently resuspended in D₂O based minimal media supplemented with d-glucose (1 g/L) and d-cel-tone (3 g/L) (Cambridge Isotope Laboratories, Inc.). Large growths (2.7 L total) were induced with IPTG (1 mM) and cells harvested after ~6 h. Uniformly deuterated α -syn was purified according to published methods.¹⁰²

Protein concentration was determined using a molar extinction coefficient estimated on the basis of amino-acid content: $\epsilon_{280\text{ nm}} = 5,120\text{ M}^{-1}\text{cm}^{-1}$ (WT, A90C) and $\epsilon_{280\text{ nm}} = 10,810\text{ M}^{-1}\text{cm}^{-1}$ (F4W, F94W). The purity of protein samples was assessed by SDS-PAGE on a Pharmacia Phastsystem (Amersham Biosciences) and visualized by silver-staining methods. The protein molecular weights were confirmed by ESI-MS (Biochemistry Core Facility, NHLBI). All purified proteins were concentrated using a YM-3 filter (MWCO 3kD, Millipore) and stored at -80 °C. For uniformly deuterated α -syn, a molecular weight of 15,472 was measured reflecting ~76% deuteration of available hydrogen.

Tetramethylrhodamine (Rho) A90C α -syn (A90C-Rho) was labeled and purified according to published protocol¹⁸⁴ with minor modification. A stock of Rho dye in dimethyl-sulfoxide was prepared and Rho labeled protein concentration determined using an $\epsilon_{511 \text{ nm}} = 90,000 \text{ M}^{-1} \text{ cm}^{-1}$.

5.2.3 Phospholipid Vesicle Preparation

Phospholipid vesicles were made from a 1:1 molar ratio of POPA and POPC. Chloroform solutions of 1:1 POPA and POPC were dried under a nitrogen stream for 20 min followed by vacuum desiccation for 45 min to ensure complete removal of organic solvent. Dried samples were then resuspended in 10 mM NaPi, 100 mM NaCl buffer, pH 7.4 to a final concentration of 5 mg/mL by bath sonication for 5 – 10 min. Vesicles were prepared *via* ultrasonication in a water bath (45 minutes, 50% duty cycle, microtip limit, Branson 450 Sonifier). Vesicle solutions were diluted to a final concentration of 2.5 mg/mL, equilibrated overnight (14 – 24 h) at 37 °C, and prepared freshly for each experiment. Average vesicle hydrodynamic radius was determined to be 45 – 55 nm by dynamic light scattering (Wyatt DynaPro NanoStar; fifty 5 s acquisitions, 25 °C).

5.2.4 Steady-state Spectroscopic Measurements

Spectroscopic measurements were made as follows: absorption, Cary 300 Bio spectrophotometer; CD, Jasco J-715 spectropolarimeter (200 – 260, 1 nm steps, 1 nm bandwidth, 0.5 s integration time, and 50 nm/min, 1 mm cuvette pathlength), and luminescence, Fluorolog-3 spectrofluorimeter ($\lambda_{\text{ex}} = 295 \text{ nm}$, $\lambda_{\text{obs}} = 300 - 500 \text{ nm}$, 0.25 s integration time, 1 and 2 nm excitation and emission slit widths, respectively).

All measurements were collected at 25 °C using temperature controlled cuvette holders except for absorbance experiments. For all spectra measured in the presence of vesicles, background scans were collected and subtracted. Prior to experiments, all α -synucleins were exchanged into 10 mM NaPi, 100 mM NaCl, pH 7.4 buffer using a PD-10 column (GE Healthcare). All protein solutions containing vesicles were incubated for at least 30 min at RT prior to measurement.

Mean residue ellipticity, $[\Theta]$ (deg cm² dmol⁻¹), was calculated according to the equation, $[\Theta] = \frac{100\theta}{clN}$ where θ is the measured ellipticity (mdeg), c is the sample concentration (mM), l is the path length (cm), and N is the number of amino acids.

Percent α -helicity was calculated using the equation $\frac{[\Theta]_{222\text{nm}} - 3,000}{-39,000} \times 100$.

Reference values of $[\Theta]_{222\text{nm}} = 0$ and $-36,000$ (deg cm² dmol⁻¹) were used for 0% and 100% helicity respectively.¹⁶¹

5.2.5 Preparation of Sparsely Tethered-lipid Bilayer Membranes for Neutron Reflectometry

Polished silicon wafers were coated with Cr adhesion layers (≈ 20 Å) and Au films (≈ 150 Å) by magnetron sputtering (Auto A306; BOC Edwards, UK, and Denton Discovery 550, Denton Vacuum, LLC, USA). A self-assembled monolayer (SAM) comprised of the lipid tether compound HC18 (Z20-(Z-octadec-9-enyloxy)-3,6,9,12,15,18,22-heptaooxatetracont-31-ene-1-thiol) was produced by immersing the Au-coated wafers in ethanolic solutions of HC18 and β ME (20:80 molar ratio, 0.2 mM final concentration).⁶⁴ After incubation (> 12 h) the wafers were thoroughly rinsed with absolute ethanol and dried under nitrogen.

Sparsely tethered bilayer lipid membranes (stBLM) were then formed by the rapid solvent exchange (RSE) procedure described elsewhere.⁶⁴ Briefly, the Si-wafer containing the SAM was assembled in a flow cell designed at the NIST Center for Neutron Research (Gaithersburg, MD). Stocks of lyophilized phospholipids were dissolved to 10 mg/mL (POPA in 95% methanol, 4% H₂O, and 1% chloroform; POPC in methanol) and mixed to a 1:1 molar ratio. The organic solution of phospholipid was injected into the flow cell and allowed to incubate for 10 min at RT. Finally, RSE was performed to complete stBLM formation process. For all reflectivity measurements, the stBLM was kept immersed in aqueous buffer solution (10 mM NaPi, 100 mM NaCl, pH 7.4).

5.2.6 Neutron Reflectivity Measurements

Neutron reflectivity measurements were performed at the NG1 reflectometer at the NIST Center for Neutron Research (NCNR).¹⁸⁸ A momentum transfer, q_z , range between 0 and at least 0.25 Å⁻¹ was used for all measurements. The stBLM was first measured in aqueous buffer (10 mM NaPi, 100 mM NaCl, pH 7.4) containing three isotopically different compositions (100% D₂O, 100% H₂O, and 2:1 H₂O:D₂O). Then, the stBLM was measured in the presence of aqueous buffers containing α -syn (3 μ M in 10 mM NaPi, 100 mM NaCl, pH 7.4, 100% H₂O or 100% D₂O). For each solution condition (contrast), adequate counting statistics were obtained after 6 – 9 h. The flow cell design allows for *in situ* isotopic solvent contrast exchange; therefore, subsequent measurements were performed on the same sample area. The entire flow cell was maintained at RT.

5.2.7 Neutron Reflectometry Data Analysis

The neutron scattering length density (nSLD) profile is modeled using a combination of a box model for the solid substrate and a composition space model¹⁸⁹ for the stBLM and the peptide. The composition space model describes the surface architecture in terms of spatial distributions of sub-molecular groups rather than slabs of constant nSLD like in the conventional box model.¹⁹⁰ The composition space model requires a minimum number of fit parameters, because it incorporates a maximum of external information about the system (*e.g.* chemical connectivity, molecular volumes, and scattering lengths). Individual sub-molecular groups implemented in the model are: β -ME, tether PEG chains, tether glycerol groups, substrate-proximal and substrate-distal PC and PA headgroups, substrate-proximal and substrate-distal hydrocarbon chains of lipid and tether molecules, and the peptide. Fit parameters are the bilayer hydrocarbon thickness, bilayer completeness, tether surface density, tether thickness, and β -ME surface density.

The peptide is modeled as two adjacent regions of constant volume occupancy. The interface between the two regions aligns with the substrate-distal headgroup interface to the bulk solvent; one region penetrates the lipid bilayer and the second region extends into the bulk solvent. Length and volume occupancy of the two regions are separate fit parameters. Reflectivity is computed using the optical matrix method¹⁸⁹ after translating the composition space model into a box model consisting of slabs of 0.5 Å width and zero roughness. Data modeling and optimization of model parameters was performed using the *ga_refl* software package¹⁸⁸ developed at the NCNR. Optimization of model parameters is achieved

by the combined use of a genetic algorithm, a simplex amoeba algorithm for efficient searching of parameter space, and a Levenberg-Marquardt non-linear least square algorithm to refine the fit. All reflectivity curves measured on the same wafer during the course of an experiment were fitted simultaneously to the same model, sharing fit parameters, for example, for the solid substrate.

An established Monte Carlo error analysis procedure¹⁸⁵ was used to determine the fit parameter confidence limits by multiple generation of simulated reflectivity consistent with the measured data based upon the statistical uncertainties of the measured data points. Simulated reflectivity curves were subsequently fitted to the same model. Using a statistic analysis of the obtained set of parameter values, a bias-free and objective estimate of the uncertainties of the resulting nSLD profiles is obtained.

5.2.8 Preparation of Supported Bilayer Membranes for Fluorescence Correlation Spectroscopy

Cleaned Lab-Tek eight-well chambered coverglass (Nunc) was used as the supported bilayer membrane (SBM) substrate. Chambers were first cleaned by rinsing with filtered and deionized water followed by 70% ethanol and water. The chamber was then submerged in a beaker containing a solution of 2% Hellemax (Hellma Analytics) in water. The beaker was then placed in a pre-heated (50 °C) water bath and subjected to three cycles of 5 min sonication followed by 5 min incubation. The coverglass was then rinsed thoroughly with water and shaken to remove excess water. Before drying, a lipid solution (200 μ L, 0.1 mM 1:1 POPA:POPC vesicles, 5 mM CaCl₂) was applied to the cleaned chamber.

Importantly, the CaCl_2 was added to the lipid solution immediately prior to application to the cleaned coverglass. After incubating for 30 min at RT to facilitate formation of the SBM, the SBM was washed by repeated buffer exchange (10 mM NaPi, 100 mM NaCl, pH 7.4) using a micropipette. During washing, the micropipette was never placed closer than 1 mm from the coverglass to avoid any damage to the SLB.

5.2.9 Fluorescence Correlation Spectroscopy

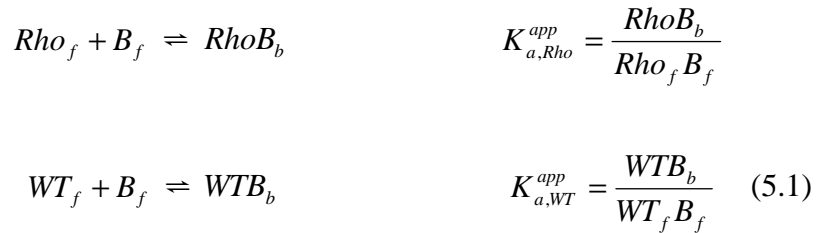
Fluorescence Correlation Spectroscopy (FCS) measurements were performed using a LSM 5 Pascal microscope (Carl Zeiss) based instrument. An argon laser (514 nm) and a 1.3 N.A. 40 \times Plan-Neofluar objective (Carl Zeiss) were used for sample excitation and emission collection, respectively. In all experiments the excitation focal volume was placed in solution above the SLB. Rho emission was selected using a band pass filter (560 – 615 nm) and focused onto an avalanche photodiode detector. Coincidence autocorrelation of data was performed using a PicoHarp 300 (PicoQuant) in time-tagged T2 mode. At least five, 20 s acquisitions were made for each condition.

Prior to A90C-Rho measurements, autocorrelation curves ($G(\tau)$) were collected for varying concentrations of Rhodamine 6G (5.5 – 50 nM in H_2O) to determine the excitation focal volume. Solutions of 500 μL were used for all sample measurements and was achieved by filling the coverglass chamber fully (~720 μL) and then removing 220 μL . For α -syn membrane binding concentration experiments, autocorrelation curves for A90C-Rho in the absence (15 nM 90C-Rho α -syn, 10 mM NaPi, 100 mM NaCl) and presence of WT protein (100 nM – 5.65 μM , 10 mM NaPi,

100 mM NaCl) were collected. For each set of A90C-Rho data, the same SLB was used. At each concentration, samples were incubated at least 10 min prior to data collection. Membrane binding curves were determined by calculating the average number of A90C-Rho proteins in the focal volume according to the equation $G(0) = 1/N$, where $G(0)$ is the value of the autocorrelation function at $\tau = 0$ and N is the average number of particles in the focal volume. In these experiments, $G(0)$ was measured at 0.01 ms to ensure minimal contributions from inter-molecular processes, and triplet formation.¹⁹¹

5.2.10 Protein-bilayer Membrane Equilibrium

FCS membrane binding equilibrium data were modeled according to the simple law of mass action for identical and independent binding sites.^{163,164} Estimation of apparent association constants were extracted according to the following two-state equilibria for the WT protein and the A90C-Rho labeled synuclein:



where Rho_f and WT_f is the free A90C-Rho and WT α -syn concentration, respectively, B_f is the free binding sites, and $RhoB_b$ and WTB_b is the bound A90C-Rho and WT α -syn concentration (occupied binding sites), respectively. The total binding sites (B_t) is defined as $B_{max} L$, where B_{max} is the maximum binding sites per

lipid molecule, and L is the total lipid concentration. Assuming that the affinity of A90C-Rho and WT for the bilayer is equal, $K_{a,Rho}^{app} = K_{a,WT}^{app}$, and that $Rho_t = Rho_f + RhoB_b$, $WT_t = WT_f + WT B_b$, and $B_t = B_f + RhoB_b + WT B_b = B_{max} L$ we can obtain the following fitting equation:

$$N = \frac{1}{2(Rho_t + WT_t)} \left(\frac{-LB_{max} Rho_t + Rho_t \left(-\frac{1}{K_a^{app}} + Rho_t + WT_t\right) + \sqrt{Rho_t^2 \left(4\frac{1}{K_a^{app}}(Rho_t + WT_t) + \left(-LB_{max} - \frac{1}{K_a^{app}} + Rho_t + WT_t\right)^2\right)}}{2} \right) \quad (5.2)$$

where N is the number free A90C-Rho α -syn (which is proportional to Rho_f) measured in FCS experiments and A is a scalar fitted to correct for the amplitude of the data. The fitting equation was solved for using Mathematic (Wolfram) and fitting was performed using IGOR Pro 6.01 (Wavemetrics).

5.3 Results and Discussion

5.3.1 Fluorescence Correlation Spectroscopic Characterization of α -Synuclein Membrane Binding to a Planar Bilayer Membrane

While the binding properties of α -syn to phospholipid vesicles of varying size and composition have been thoroughly investigated,^{64,185} to assess binding to a planar membrane geometry similar to that used in NR experiments, a supported lipid bilayer (SLB) was produced for use in fluorescence correlation spectroscopy (FCS) experiments. In FCS, time-dependent intensity fluctuations resulting from fluorescent molecules diffusing in and out of a small focal volume can be measured.⁵⁹ Autocorrelation of these fluctuations facilitates determination of diffusion coefficients as well as sample concentration.⁵⁹

To generate α -syn SLB binding curves using FCS, autocorrelation curves were collected for singly labeled tetramethylrhodamine A90C α -syn (A90C-Rho) exposed to the SLB in the absence (15 nM 90C-Rho α -syn, 10 mM NaPi, 100 mM NaCl) and presence of WT protein (100 nM – 5.65 μ M, 10 mM NaPi, 100 mM NaCl). In these experiments the FCS focal volume was placed in solution above the SLB. A POPA:POPC lipid composition was chosen for the SLB to facilitate comparison to our prior work using 1:1 POPA:POPC vesicles¹⁰² and because α -syn has been demonstrated by numerous groups to have a high affinity for POPA.^{116,192}

At low α -syn concentrations (15 nM A90C-Rho), most of the proteins are bound to the SLB and thus a low concentration is measured in solution. As non-fluorescent WT protein is added, bound A90C-Rho proteins exchange with WT leading to an increase in A90C-Rho proteins diffusing through the focal volume. [Figure 5.1](#) shows the autocorrelation curves ($G(\tau)$) generated for 15 nM 90C-Rho (red) and upon addition of varying concentrations of WT protein (100 nM – 5.65 μ M). As expected, the amplitude of the ($G(\tau)$) curves decreases as WT protein is added while the characteristic diffusion time (approximately the half amplitude of $G(\tau)$ ¹⁹¹) of the A90C-Rho species in solution remains constant at all concentrations (~105 – 115 μ s).

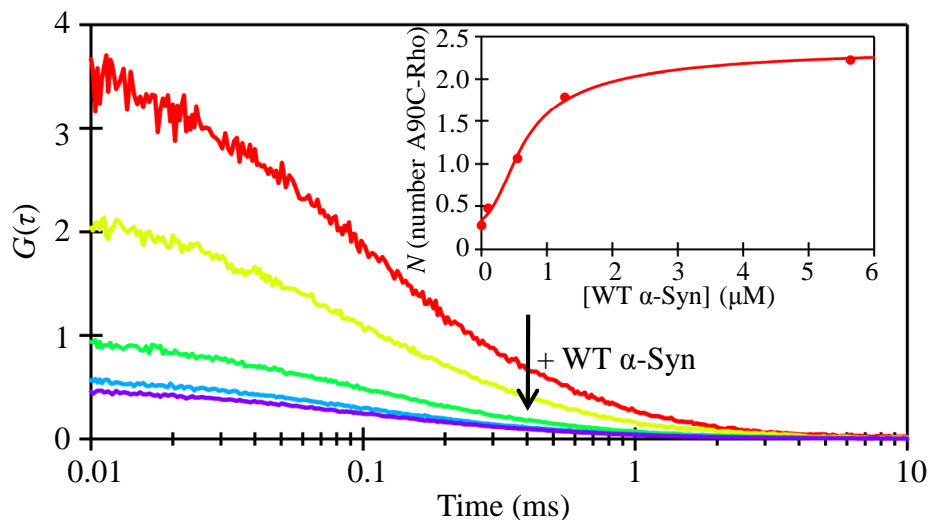


Figure 5.1 Fluorescence correlation spectroscopy (FCS) autocorrelation curves ($G(\tau)$) for singly labeled tetramethylrhodamine (Rho) A90C α -syn (A90C-Rho) exposed to a supported lipid bilayer (1:1 POPA:POPC) in the absence (15 nM A90C-Rho α -syn, 10 mM NaPi, 100 mM NaCl) and presence of WT protein (100 nM – 5.65 μ M). (Inset) Number of Rho α -synucleins in FCS focal volume as a function of total protein concentration. The fit of the data is shown as a solid line.

The average number of fluorescent proteins diffusing through the focal volume, N ($N = 1/G(0)$) as a function of total protein concentration is shown in the inset of Figure 5.1. Fitting this data using a law of mass action for identical independent binding sites yields an apparent association constant (K_a^{app}) of $\sim 2 \times 10^7$ M^{-1} . This value is highly consistent with that previously determined for POPA:POPC unilamellar vesicles (~ 100 nm diameter, $K_a^{app} \sim 1 \times 10^7$ M^{-1}),¹⁰² reflecting that effects due to curvature are minimized in this size regime.

5.3.2 Neutron Reflectometry as a Dual Probe of α -Synuclein and Membrane Structure

To simultaneously probe α -syn and phospholipid bilayer structure neutron reflection measurements were performed.^{64,185,188} Specifically, the neutron reflection of a stBLM composed of 1:1 molar ratio of POPA:POPC in the presence and absence

of α -syn (3 μ M in 10 mM NaPi, 100 mM NaCl) was measured. A minimum of two reflectivity curves were collected for each condition using isotopically different solvents (*e.g.* H₂O or D₂O based buffer). [Figure 5.2a](#) shows the neutron reflection for the stBLM alone and in the presence of α -syn in H₂O (red) and D₂O (blue) buffers. For both solvents, residuals between reflectivity curves with and without peptide exceed five standard deviations at low momentum transfer values and average 1 – 3 standard deviations up to a momentum transfer $q_z = 0.15 \text{ \AA}^{-1}$. These significant changes in the measured reflectivity upon the addition of protein manifest in a modulation of the amplitude and the frequency of the Kiessig fringes. These fringes occur due to the interference of neutrons reflected from each of the different organic interface layers and are therefore related to thickness of each layer. Fits of the data based on a composition space model¹⁸⁹ (see Materials and Methods) are shown as solid lines. Along with a schematic view of the stBLM, [Figure 5.2b](#) shows a cross-sectional profile of the organic interface extracted from the best fit to the data. For simplicity, a number of sub-molecular groups that were modeled separately have been combined in this representation.

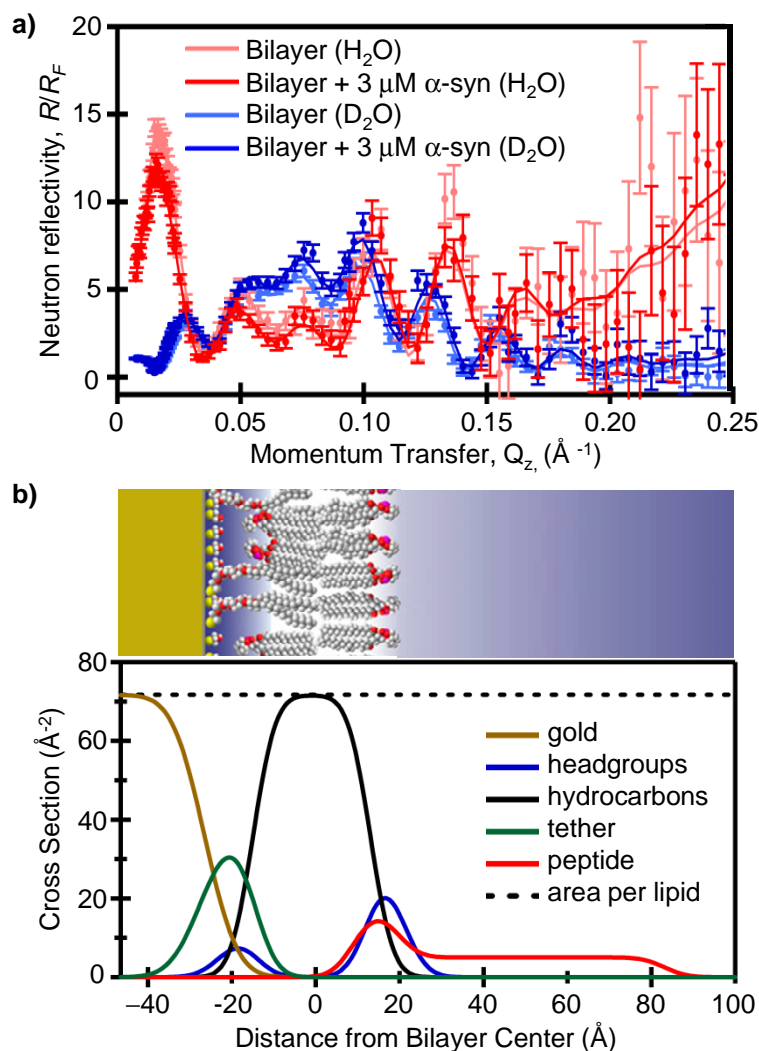


Figure 5.2 Neutron reflection of a sparsely tethered POPA:POPC bilayer lipid membrane (stBLM) and changes resulting from the addition of α -syn. (a) Neutron reflectivity (R/R_F) for a POPA:POPC stBLM in the absence and presence of α -syn (3 μM in 10 mM NaPi, 100 mM NaCl, pH 7.4) in H_2O and D_2O . Composition space model fits to the data are shown as solid lines. Error bars represent the 68% confidence intervals for the measured reflectivity based on Poisson statistics. (b, Top) Schematic of stBLM with additional solid substrate portions (Si, SiOx, Cr, and Au) partially omitted. (b, Bottom) Simplified molecular distributions for each of the organic interface layers of the POPA:POPC stBLM and α -syn obtained from best-fit of reflectivity data to the composition space model. The dotted line denotes a reference value for area per lipid. Data for Si substrate and the SiOx, Cr, and Au layer are partially omitted

Table 5.1: Neutron reflectometry fitting parameters for a POPA:POPC stBLM in the absence and presence of α -syn (3 μ M in 10 mM NaPi, 100 mM NaCl, pH 7.4).

PARAMETER	NEAT BILAYER ^a	+ 3 μ M α -SYNUCLEIN ^a
Solid Substrate		
thickness SiOx (\AA)	21.8 ^{+1.0} _{-1.1}	
nSLD SiOx (\AA^{-2})	3.64×10^{-6} (fixed)	
thickness Au (\AA)	162.2 ^{+0.5} _{-0.4}	
nSLD Au (\AA^{-2})	$4.51^{+0.01}$ _{-0.01} $\times 10^{-6}$	
stBLM, Tether Region		
thickness tether (\AA)	12.3 ^{+0.3} _{-0.4}	
number of β -mercaptoethanol molecules per tether molecule	$0.79^{+0.02}$ _{-0.02}	
stBLM, Lipid Bilayer Region		
molar fraction of tether hydrocarbon chains in inner bilayer leaflet	$0.64^{+0.10}$ _{-0.12}	
thickness inner bilayer leaflet (\AA)	$14.4^{+1.2}$ _{-1.2}	Change: $-0.72^{+0.20}$ _{-0.24}
thickness outer bilayer leaflet (\AA)	$14.8^{+1.1}$ _{-1.0}	Change: $-0.72^{+0.20}$ _{-0.24}
bilayer completeness	$0.95^{+0.01}$ _{-0.01}	$1.00^{+0.01}$ _{-0.01}
Peptide, High Density Region^b		
thickness (\AA)	NA	$13.1^{+7.6}$ _{-3.4}
penetration into the hydrocarbon region (\AA)	NA	$4.2^{+5.5}$ _{-2.2}
volume occupancy of peptide	NA	$0.15^{+0.12}$ _{-0.09}
Peptide, Low Density Region^c		
thickness (\AA)	NA	$63.1^{+4.7}$ _{-5.0}
volume occupancy of peptide	NA	$0.068^{+0.008}$ _{-0.009}

^a The 68.2% confidence intervals for each fit parameter are designated in super- and subscripts.

^b The high density peptide region is located near substrate-distal headgroups and penetrates into the hydrocarbon chains of the bilayer.

^c The low density region is located above the outer headgroups and describes peptide which is extended into the bulk solvent phase.

Using a Monte Carlo resampling procedure, bilayer and protein fit parameters (layer thickness, neutron scattering length density (nSLD), volume occupancy) and the associated 68.2% confidence intervals were computed (Table 5.1). Prior to incubation with protein, substrate and neat bilayer parameters fall within expected values with an inner and outer bilayer leaflet thickness of $14.4^{+1.2}_{-1.2}$ \AA and $14.8^{+1.1}_{-1.2}$ \AA ,

respectively. Upon protein addition, reflectivity data indicate that substantial α -syn (15₋₉¹²% volume occupancy) is associating with the membrane at both the head group and hydrocarbon region (13.1_{-3.4}^{7.6} Å thick protein region penetrating 4.2_{-2.0}^{5.5} Å into the outerleaflet hydrocarbons). α -Syn (6.8_{-0.9}^{0.8}% volume occupancy) was also found to extend well into the bulk solvent region (63.1_{-5.0}^{4.7} Å). The association of α -syn also resulted in sizable reduction (1.44_{-0.48}^{0.40} Å) in membrane bilayer thickness.

Though exact protein conformation(s) cannot be determined, neutron reflectivity data are consistent with a scenario in which α -syn is anchored to the membrane by key interaction sites leaving other protein regions solvent exposed. Moreover, given the thickness of the high density protein region situated in the headgroups and hydrocarbons (\sim 13.1_{-3.4}^{7.6} Å), it is plausible that membrane associated α -syn is in an α -helical conformation. These data support recent NMR results³⁹ in that N-terminal residues could be associated to the membrane while more central and C-terminal residues remain solvent accessible. Surprisingly, though α -syn has been implicated as a membrane curvature sensor, in which tighter binding is observed in the presence of smaller, more highly curved phospholipid vesicles,¹¹⁶ we find α -syn has a relatively high surface coverage (\sim 15% at the head group and hydrocarbon region) in the presence of 3 μ M protein as compared to previous work employing lipid vesicles (average diameter 80 nm, \sim 7%) of identical phospholipid composition.¹⁰² It is plausible that due to the larger size of the vesicles used, curvature effects are attenuated as has been observed in a recent study on the effect of membrane curvature on α -syn membrane binding.¹⁹²

The observation that bilayer thickness is reduced upon α -syn association is intriguing because protein induced membrane perturbations have been linked to disease pathology.¹²⁵⁻¹²⁸ Specifically, it was shown that protofibrillar α -syn can induce transient permeabilization in anionic membranes and thus may be related to cell toxicity and disease by altering the calcium flux into the cytosol, depolarization of mitochondrial membranes, and/or leakage of intra-vesicular neurotransmitter molecules, such as dopamine.¹²⁹ Numerous subsequent *in vitro* studies corroborate a possible role for α -syn in membrane perturbation and/or permeabilization.^{119,130-136} Notably, though membrane perturbation is generally found in the presence of oligomeric or protofibrillar α -syn, we observe bilayer thinning upon the addition of monomeric α -syn. While the completeness of the stBLM was maintained during the course of our experiments (~95% – 100% completeness), it is plausible that measured membrane thinning could represent a first step leading to disruption or even permeabilization of the bilayer as found under certain solution conditions.

5.3.3 Using Neutron Reflectometry to Examine the Effects of α -Synuclein Concentration on the Protein-membrane Interface

Elucidating how changes in lipid-to-protein stoichiometry affect protein and membrane properties is important because changes in α -syn concentration in the body are linked to early-onset PD.^{72,73} Moreover, α -syn aggregation kinetics are modulated by the presence of varying concentrations of lipid vesicles *in vitro*.¹¹⁷⁻¹¹⁹ To gain insights into the role of membrane-protein stoichiometry in modulating membrane-bound α -syn structure and membrane properties, NR was performed on a stBLM (1:1 molar ratio POPA:POPC) in the presence of varying concentrations of α -syn (10 nM

– 5 μ M in 10 mM NaPi, 100 mM NaCl). For enhanced contrast between the stBLM and the protein, uniformly deuterated α -syn was produced and used in these experiments (~76% estimated by ESI-MS). Again, a minimum of two reflectivity curves were collected for each condition using isotopically different solvents.

Prior to NR experiments, the effect of deuteration on α -syn membrane binding was assessed by using CD spectroscopy. Specifically, we compared changes in α -helical content (change in mean residue ellipticity at 222 nm; $\Delta[\Theta]_{222\text{nm}}$) of the deuterated and protonated protein in the presence of varying concentrations of POPA:POPC unilamellar vesicles. As shown in Figure 5.3, $\Delta[\Theta]_{222\text{nm}}$ for the deuterated protein (red) is comparable to that of the protonated protein (black).

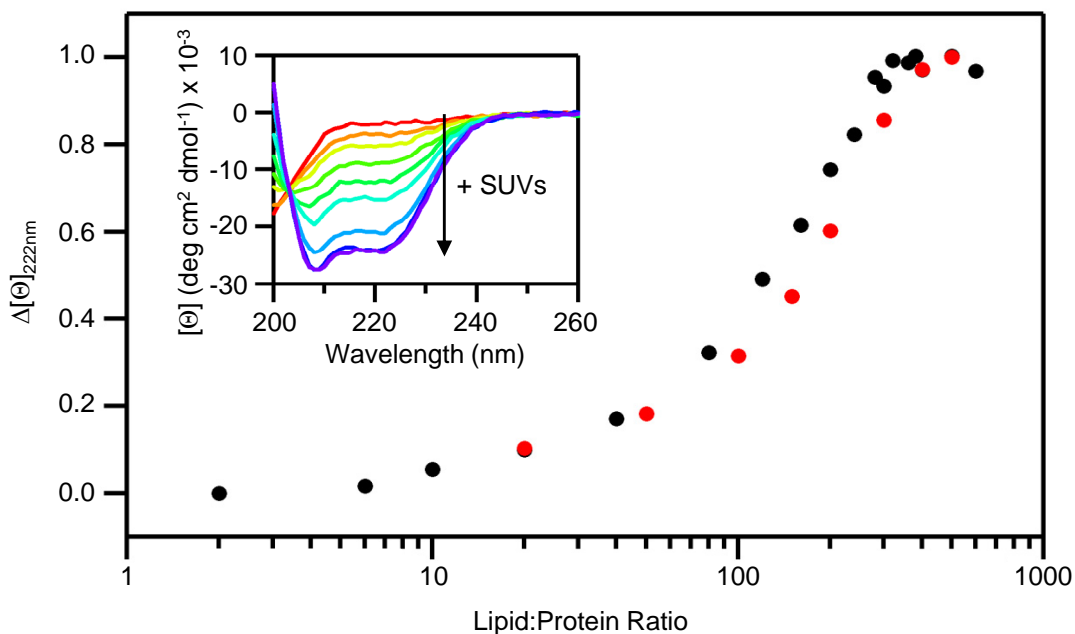


Figure 5.3 Comparison of membrane induced secondary structure for protonated (black) and uniformly deuterated (red) WT α -syn in 10 mM NaPi, 100 mM NaCl, pH 7.4 buffer with addition of lipid vesicles (1:1 molar ratio POPA:POPC). (Inset) Circular dichroism spectra for uniformly deuterated α -syn with additions of POPA:POPC vesicles.

Figure 5.4 shows the neutron reflection for the stBLM alone and in the presence of deuterated α -syn (5 μM in 10 mM NaPi, 100 mM NaCl, pH 7.4 H₂O buffer). Reflectivity curves for the other concentrations tested (10 nM, 50 nM, 250 nM, and 1 μM) fall within these curves, but have been omitted for clarity. Once again, significant changes in the measured reflectivity upon the addition of protein are present and manifest in modulation of the amplitude and the frequency of the Kiessig fringes. Fits of the data based on a composition space model¹⁸⁹ are shown as solid lines.

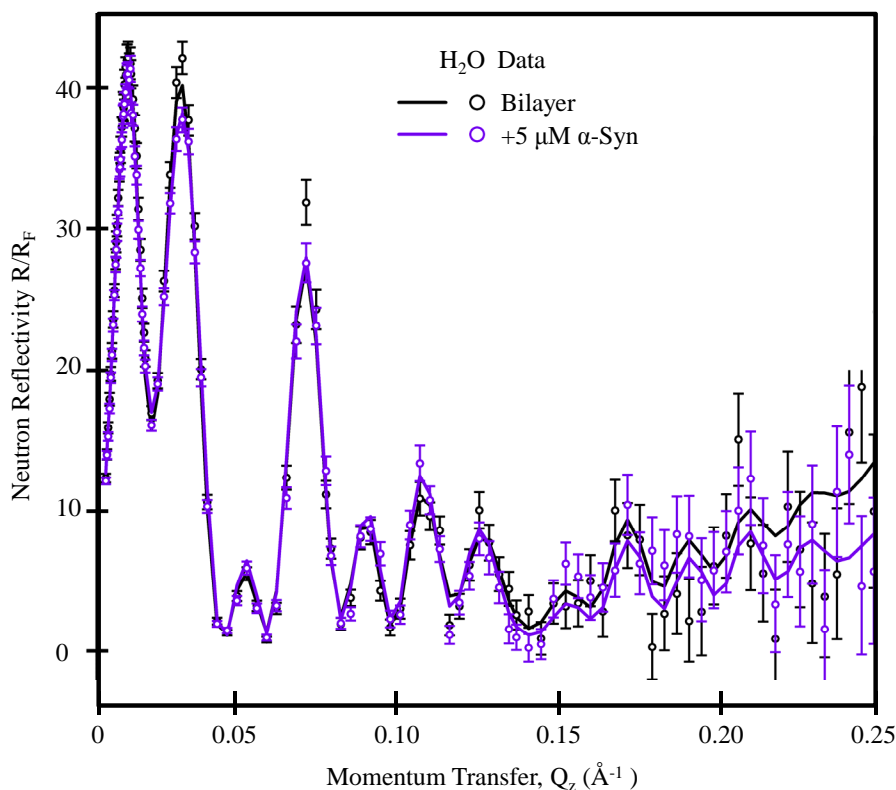


Figure 5.4 Neutron reflectivity (R/R_F) for a POPA:POPC stBLM in the absence and presence of deuterated α -syn (5 μM in 10 mM NaPi, 100 mM NaCl, pH 7.4) in H₂O. Composition space model fits to the data are shown as solid lines. Error bars represent the 68% confidence intervals for the measured reflectivity based on Poisson statistics.

Using best fits to NR data,¹⁸⁹ a cross-sectional profile of the organic interfaces at each α -syn concentration was generated. Simplified molecular distributions for the POPA:POPC stBLM in the presence of varying concentrations of α -syn (10 nM – 5 μ M, in 10 mM NaPi, 100 mM NaCl, pH 7.4) are shown in Figure 5.5. Fit parameters extracted from the best fits to the data can be found in Table 5.2. Prior to incubation with protein, substrate and neat bilayer parameters fall within expected values with an inner and outer bilayer leaflet thickness of $18.59_{-1.21}^{1.1}$ Å and $14.96_{-1.43}^{2.5}$ Å, respectively. Consistent with previous NR measurements, upon protein addition, membrane-associated α -syn extends into the hydrocarbon core as well as into the bulk solvent region. Membrane thinning was also observed at all concentrations.

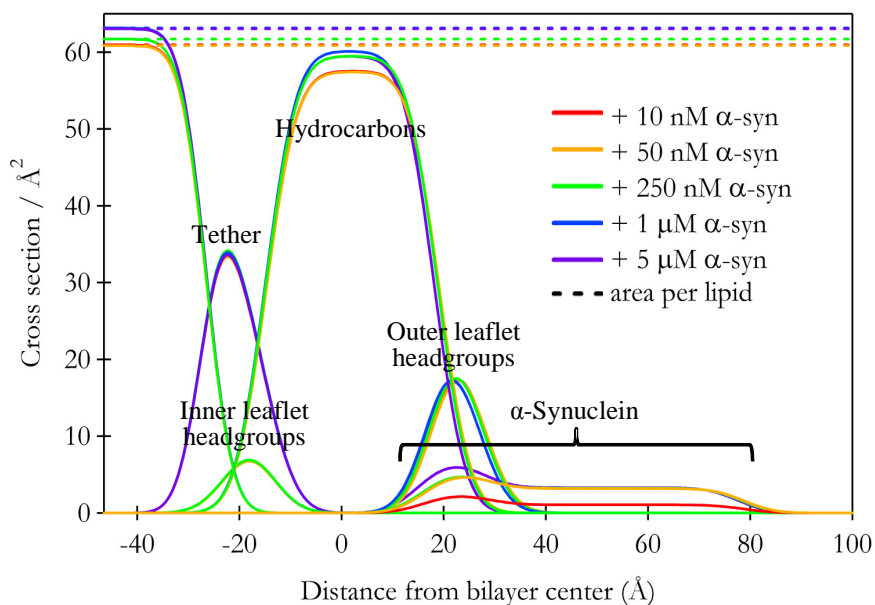


Figure 5.5 Simplified molecular distributions for each of the organic interface layers of the POPA:POPC stBLM in the presence of varying concentrations of α -syn (10 nM – 5 μ M, in 10 mM NaPi, 100 mM NaCl, pH 7.4)

Table 5.2: Neutron reflectometry fitting parameters for a POPA:POPC stBLM in the presence of varying concentrations of α -syn (0 – 5 μ M in 10 mM NaPi, 100 mM NaCl, pH 7.4).

PARAMETER	NEAT BILAYER ^a	α -SYNUCLEIN ^a				
		10 nM	50 nM	0.25 μ M	1 μ M	5 μ M
Solid Substrate						
thickness SiOx (Å)		14.68 ^{+0.19} _{-0.19}				
nSLD SiOx (Å ⁻²)		3.64 × 10 ⁻⁶ (fixed)				
thickness Au (Å)		135.88 ^{+0.37} _{-0.38}				
nSLD Au (Å ⁻²)		4.303 ^{+0.042} _{-0.042} × 10 ⁻⁶				
stBLM, Tether Region						
thickness tether		12.73 ^{+0.69} _{-0.56} Å				
number of β -mercaptoethanol molecules per tether molecule		0.87 ^{+0.57} _{-0.22}				
stBLM, Lipid Bilayer Region						
thickness inner bilayer leaflet (Å)	18.59 ^{+1.1} _{-1.21}	Change				
thickness outer bilayer leaflet (Å)	14.96 ^{+2.2} _{-1.43}	-0.286 ^{+0.198} _{-0.176}	-0.308 ^{+0.264} _{-0.209}	-0.561 ^{+0.242} _{-0.176}	-0.891 ^{+0.253} _{-0.168}	-0.946 ^{+0.297} _{-0.209}
bilayer completeness	0.952 ^{+0.017} _{-0.011}	0.941 ^{+0.017} _{-0.016}	0.941 ^{+0.017} _{-0.016}	0.967 ^{+0.017} _{-0.013}	0.950 ^{+0.020} _{-0.017}	0.945 ^{+0.018} _{0.018}
Peptide, High Density Region^b						
thickness (Å)	NA	15.26 ^{+3.3} _{-6.0}				
penetration into the hydrocarbon core (Å)	NA	5.7 ^{+3.3} _{-6.0}				
volume occupancy of peptide	NA	0.046 ^{+0.057} _{-0.046}	0.078 ^{+0.062} _{-0.071}	0.089 ^{+0.057} _{-0.081}	0.101 ^{+0.053} _{-0.077}	0.117 ^{+0.054} _{-0.077}
Peptide, Low Density Region^c						
thickness (Å)	NA	56 Å (fixed)				
volume occupancy of peptide	NA	0.019 ^{+0.022} _{-0.019}	0.042 ^{+0.015} _{-0.022}	0.043 ^{+0.015} _{-0.022}	0.045 ^{+0.016} _{-0.022}	0.046 ^{+0.016} _{-0.022}

^a The 68.2% confidence intervals for each fit parameter are designated in super- and subscripts.

^b The high density peptide region is located near substrate-distal headgroups and penetrates into the hydrocarbon chains of the bilayer.

^c The low density region is located above the outer headgroups and describes peptide which is extended into the bulk solvent phase

While not precluding local protein conformational changes, values for average α -syn bilayer penetration (5.7^{+3.3}_{-6.0} Å) and extension into the bulk solvent (56 Å) were consistent for all protein concentrations tested. However, significant differences in the volume fraction occupancy in each of the regions were observed

upon increased α -syn. Relative trends in volume fraction of α -syn in the headgroup/hydrocarbon and bulk solvent region as well as in bilayer thinning are provided in Figure 5.6. In this representation all data are normalized to values for the lowest and highest protein concentration to facilitate comparison (for absolute values, see Table 5.2). At 10 nM α -syn, the volume fraction of protein in the hydrocarbon/headgroup and bulk solvent region is $0.046_{-0.046}^{0.057}$ and $0.019_{-0.019}^{0.022}$, respectively. As the protein concentration is increased (10 nM – 5 μ M), the volume fraction in the hydrocarbon and headgroups increases ($0.046_{-0.046}^{0.057}$ – $0.117_{-0.077}^{0.054}$) though not fully saturating. In contrast, the volume fraction extending into the bulk solvent nearly saturates by 50 nM at a value of $0.042_{-0.022}^{0.015}$ as compared to $0.046_{-0.022}^{0.016}$ at 5 μ M.

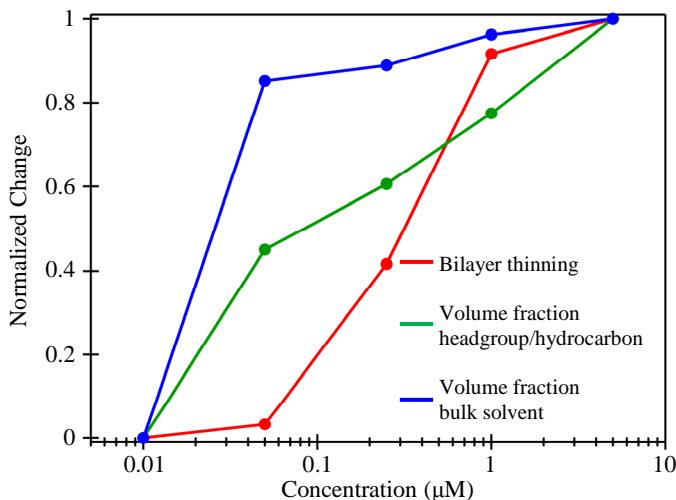


Figure 5.6 Comparison of volume fraction of membrane bound α -synuclein extending into the bulk solvent (blue) and occupying the headgroup/hydrocarbon region (green) as well as the degree of membrane thinning (red) as a function of α -synuclein concentration.

Though no direct correlations between membrane thinning and the volume fraction of α -syn in the hydrocarbon/headgroup region are present, significant membrane thinning is only observed when occupancy in the bulk solvent region reaches near saturating values (> 50 nM α -syn). Since volume occupancy in the hydrocarbon/headgroup region continues to increase at concentrations above 50 nM, it is plausible that as proteins concentrate at the vesicle surface, sufficient neutralization of the anionic membrane ensues promoting a fraction of membrane-bound proteins into conformations that do not extend into the bulk solvent region. Alternatively, as the membrane thins, greater penetration of membrane-bound proteins may ensue and manifest in increased occupancy in the hydrocarbon/headgroup region. Regardless of the exact conformations, these data do suggest that even small changes in the soluble monomeric α -syn concentration can promote membrane thinning. It is possible that similar small changes in α -syn concentration *in vivo* could also promote membrane permeabilization which has been linked to cell toxicity and PD pathogenesis.

5.4 Summary

Using NR and A POPC:POPC stBLM, we have examined membrane-bound α -syn structure as well as changes in phospholipid bilayer properties resulting from protein binding. We find that α -syn associates with the membrane at both the headgroup and hydrocarbon chain region, extends into the bulk solvent, and induces membrane thinning. These data provide the first structural evidence at the molecular level for membrane perturbation by monomeric α -syn. Since changes in α -syn concentration have been linked to early-onset PD,^{72,73} addition NR experiments were

performed to examine the effects of lipid-to-protein stoichiometry on protein and membrane structure. In these experiments uniformly deuterated α -syn was used to ensure greatest contrast between the protein and the bilayer. NR data reveal α -syn concentration dependent (10 nM – 5 μ M) changes in membrane thinning ($0.52_{-0.32}^{0.36}$ – $1.72_{-0.30}^{0.54}$ Å) as well as protein volume occupancy in the headgroup/hydrocarbon ($0.046_{-0.046}^{0.057}$ – $0.117_{-0.077}^{0.054}$) and bulk solvent ($0.019_{-0.019}^{0.022}$ – $0.046_{-0.022}^{0.016}$) regions.

Chapter 6: Effects of pH on Aggregation Kinetics of the Repeat Domain of a Functional Amyloid, Pmel17*

6.1 Introduction

Though amyloid structure is mostly recognized for its involvement in human diseases such as Alzheimer's and Parkinson's disease, it is striking to find that amyloid fibrils can also serve essential biological roles.⁸⁻¹² A central question is why functional amyloids are benign whereas their disease-related counterparts are not. Specifically, it is not clear if functional amyloidogenic proteins are not cytotoxic because they circumvent conformationally altered (misfolded) fibrillar precursors such as spheres and annuli,¹⁴ or because their amyloid formation and degradation are efficiently regulated by the cell. Because such issues remain poorly understood, detailed studies on amyloid formation kinetics as well as the solution conditions and biomolecules that impact this assembly are required.

Elucidating the aggregation kinetics and fibrillar structures of the functional amyloid, Pmel17, whose fibrils serve as the structural scaffolding required for melanin deposition in human skin and eyes, is of particular interest. Moreover, because melanosomes, organelles where Pmel17 fibrils are formed, are acidic

* Adapted from Pfefferkorn, C. M.; McGlinchey, R. P.; Lee, J. C. Effects of pH on aggregation kinetics of the repeat domain of a functional amyloid, Pmel17. *Proc. Nat. Acad. Sci. U.S.A.* 107 (2010) 21447 – 21452. Thanks to Mathew Daniels and Patricia Connelly (Electron Microscopy Core Facility, NHLBI) for helpful discussion, and Greg Piszczek (Biophysics Facility, NHLBI) for technical assistance.

compartments that change pH during maturation, understanding the role of solution pH in fibril formation is also of particular interest.¹⁹³

Melanin is synthesized in melanosomes, organelles related to both endosomes and lysosomes, and stored in melanocytes, cells responsible for pigmentation.¹³ The rate limiting step in melanin synthesis is catalyzed by tyrosinase. In this reaction, tyrosine is converted to dihydroxyphenylalanine (DOPA) which is then transformed to dopaquinone and readily oxidized to 5,6-dihydroxyindole followed by indole-5,6-quinone. Melanin is the polymerized product. Importantly, Pmel17 fibrils have been proposed to sequester and detoxify these potent cytotoxic precursors.¹⁹⁴

The melanosome maturation process has been shown to involve four distinct stages that have been characterized in detail at the ultrastructural level by TEM.¹⁹⁵ Fibrous structures begin to form in stage I with aggregation completed by stage II.¹³ Melanin is produced and deposited during later stages, III and IV.¹³ While melanosome ultrastructure is known, the molecular nature of Pmel17 fibrils and how intramelanosomal solution conditions mediate fibril formation remain to be elucidated. Interestingly, it is known that solution pH changes with melanosome maturation with early stages I and II being the most acidic and later stages III and IV reaching near neutral pH.^{196,197} The activity of tyrosinase is also pH dependent *in vitro*,¹⁹⁸ with the final step in melanin polymerization slowed under acidic conditions.¹⁹⁹ Tyrosinase enzymatic assay results suggest that melanin synthesis indeed is more likely to occur in the mature melanosomes near neutral pH. Because pH mediates melanin synthesis and has been shown to affect the aggregation of

disease-related amyloidogenic polypeptides *in vitro*,⁸ we suggest that solution pH also could influence Pmel17 fibril formation within the melanosome.

The Pmel17 gene was first discovered in mice in 1930;²⁰⁰ although, it was not until 1991 when it was named and mapped to the *silver* locus.²⁰¹ Because its over-expression in non-pigmented cells produces late endosomes exhibiting indistinguishable fibrous striations from those found in melanosomes,²⁰² Pmel17 was implicated as the main protein component in melanosomal fibrils. Furthermore, when fibrils are not present, mice present a silver genotype, hence corroborating the biological function of Pmel17 in normal melanin production.²⁰³ The 668-residue polypeptide, Pmel17, is composed of a large luminal domain containing several sub-domains with short C-terminal transmembrane (35 residues) and cytoplasmic segments (30 residues).²⁰³ Posttranslational proteolytic processing of Pmel17 is critical for function producing respective C- and N-terminal fragments, M β and M α ,²⁰⁴ the latter reported to form amyloid *in vitro*.¹⁹⁴ *In vivo*, subsequent cleavage of M α results in M α N and M α C, where the C-terminal fragment, M α C is believed to contain the fibril-forming region; however, neither the precise sequence of M α N or M α C is fully identified.²⁰⁵⁻²⁰⁸ Though there is no current consensus as to which polypeptide domain solely or partly constitutes the amyloid core of the Pmel17 filaments, recent results have shown that both isolated luminal regions, the repeat domain, RPT, residues 315 – 444 (Figure 6.1)²⁰⁹ and the polycystic kidney disease-1 like domain, residues 201 – 314²¹⁰ are sufficient for amyloid formation *in vitro*. While both domains are known to be important for fibril formation *in vivo*,²¹¹ RPT is used as a model system to study Pmel17 amyloid formation kinetics in this work

because prior observation revealed that RPT fibril stability is particularly pH sensitive.²⁰⁹ Further, the inability of a closely related, melanosomal glycoprotein, NMB, which lacks a RPT domain, to form fibers also points to the role of this sequence in amyloid formation.²¹²

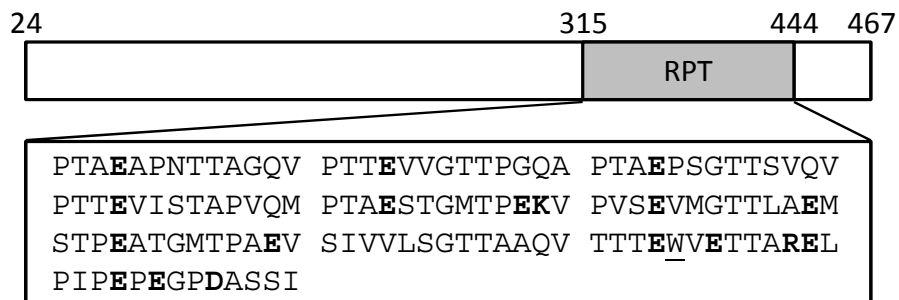


Figure 6.1 A schematic representation of the N-terminal domain ($M\alpha$) of Pmel17 with the repeat domain (RPT, residues 315 – 444) highlighted. The amino acid sequence of RPT is shown with ionizable sidechains in bold. The native fluorophore, W423, utilized in this study is underlined.

In this chapter, we investigate the aggregation kinetics and fibrillar structures of the crucial polypeptide fragment, the repeat domain (RPT) of Pmel17. Specifically, RPT conformational changes from soluble and unstructured monomer to aggregated, β -sheet-containing fibrils are monitored. To mimic the changing acidic pH conditions of the maturing melanosome,^{193,196,213} RPT amyloid formation kinetics and the conversion of fibril morphology as a function of solution pH (4 – 7) were measured. Since tryptophan emission is highly sensitive to solvent polarity, local conformational changes, and protein-protein interactions,^{44,59} the only intrinsic tryptophan (W423) is exploited as a site-specific fluorescent probe of amyloid structure and aggregation kinetics. W423 is exquisitely sensitive to soluble and

fibrillar RPT conformation with spectral properties (integrated intensity (I) and mean wavelength $\langle\lambda\rangle$) exhibiting distinct temporal changes under the various solution conditions examined. Complementary techniques, TEM and CD spectroscopy, also were employed to characterize fibrillar ultrastructures and secondary structural content, respectively.

6.2 Materials and Methods

6.2.1 Materials

N-acetyl-tryptophanamide (NATA) and acrylamide were obtained from Sigma-Aldrich (St. Louis, MO).

6.2.2 Protein Expression and Purification

Protein expression and purification were carried out as previously described with the following modification.²⁰⁹ Cell lysis buffer contained 8 M guanidinium hydrochloride, 100 mM NaCl, 100 mM K₂HPO₄, pH 7.5, and 10 mM imidazole. All purified proteins (2 – 6 mg/mL) were stored at 4°C until use.

6.2.3 Fibril Formation Kinetics and pH Titration

Purified RPT was filtered through Microcon YM-100 spin filter units (MWCO 100kD, Millipore) and exchanged into the appropriate aggregation buffer (pH 4.0 – 5.6: 20 mM sodium acetate, 100 mM NaCl, pH 6.0: 20 mM MES, 100 mM NaCl and pH 7.0 – 7.3: 20 mM MOPS, 100 mM NaCl) using PD10 (GE Healthcare) desalting columns. The integrity of all protein samples were assessed by SDS-PAGE on a Pharmacia Phastsystem (Amersham Biosciences) visualized by silver-staining

methods. All buffers were filtered (0.2 μm). Final protein solutions (2 – 60 μM , 1.5 – 2.0 mL) were added to and sealed in screw-cap, quartz cuvettes (10 x 10 mm). To initiate RPT aggregation, the cuvettes were put into an incubating microplate shaker (VWR) at 37 $^{\circ}\text{C}$ and 600 rpm.

At various aging times, protein samples (cuvettes) were removed from the incubator for measurements of absorption, fluorescence, and laser light scattering. Absorption and fluorescence ($\lambda_{\text{ex}} = 280 \text{ nm}$, $\lambda_{\text{obs}} = 300 - 500 \text{ nm}$, 0.3 s integration time, 1 nm bandwidths, 25 $^{\circ}\text{C}$, a long pass filter (290 nm) was used to minimize scattering background) spectra were obtained on a CARY 300 Bio spectrophotometer (Varian) and a Fluorolog 3 fluorimeter (Horiba Jobin Yvon), respectively. To verify minimal thermal and/or photodamage ($\leq 5\%$ over the course of 1 week, 29 time points) and to correct for any emission intensity variations (lamp power) all steady-state emission spectra were normalized to the emission of a model fluorophore, N-acetyl-tryptophanamide incubated at 37 $^{\circ}\text{C}$. Laser light scattering experiments were carried out using a home-built apparatus consisting of a CW laser ($\lambda_{\text{ex}} = 450 \text{ nm}$, CrystaLaser) as the excitation source and a photodiode as the detector at a 90° geometry. Scattering intensities (mV) were recorded using a data recorder and averaged over a 30-s period while stirring at ambient temperature. Reported values for scattering were determined according to the following equation:

$$\text{Scattering}_{\text{Norm}} = \frac{I_{\text{RPT}}}{I_{\text{refRPT}}} / \frac{I_{\text{Std}}}{I_{\text{refStd}}} \quad (6.1),$$

where $\text{Scattering}_{\text{Norm}}$ is the normalized scattering intensity of the RPT sample, I_{Std} is the scattering intensity of a standard (polystyrene beads) sample, and I_{refRPT} and I_{refStd}

are the intensities from a reference photodiode monitoring laser power for RPT and standard scattering sample, respectively. Dynamic light scattering data were collected and correlation times, τ_c , determined using a Wyatt DynaPro NanoStar (50 5s acquisitions, 25 °C).

For pH titration experiments, small amounts (5 – 20 μ L) of 1 M sodium hydroxide were added to preaggregated samples of RPT at pH 4.0 (1.5 mL, ([RPT]= 30 μ M for 72 h at 37 °C, 600 rpm) to raise pH from 4 \rightarrow 5 and then subsequently from pH 5 \rightarrow 7. At each pH, a steady-state emission spectrum (uncorrected, dilution effects were negligible < 2%) was collected and a TEM grid was prepared after equilibrium was reached as evidenced by stabilization of the W423 steady-state emission spectrum (within 10 min after NaOH addition, 25°C, stirring).

6.2.4 Fibril Characterization

At various aging times, cuvettes containing protein were opened to extract samples for ThT binding measurements (133 μ L) and for TEM (10 μ L). For ThT experiments, protein samples were diluted (6.7 μ M final concentration) with freshly prepared ThT (20 μ M) in appropriate aggregation buffer (*vide supra*). ThT samples were equilibrated at room temperature and fluorescence measured on a Fluorolog 3 fluorimeter (Horiba Jobin Yvon) (λ_{ex} = 400 nm, λ_{obs} = 450 – 700 nm, 0.25 s integration time, 2 nm bandwidths, 25 °C). TEM was performed using a JEOL JEM 1200EX transmission electron microscope (accelerating voltage 80 keV) equipped with an AMT XR-60 digital camera (Electron Microscopy Core, NHLBI). Sample grids (400-mesh formvar and carbon coated copper, Electron Microscopy Sciences) were glow discharged for 30 s using an EMScope TB500 (Emscope Laboratories) to

increase surface hydrophilicity prior to deposition of protein sample (5 μL). After 1.5 min, excess sample was absorbed with filter paper and stained by two application/wick cycles (30 and 10 s) of 0.5% w/v aqueous uranyl acetate solution. Before and after incubation, CD spectroscopy was performed to verify secondary structural transitions. CD spectra were collected on a Jasco J-715 spectropolarimeter (205 – 260 nm, 1 nm steps, 1 nm bandwidth, 0.5 s integration time, and 50 nm/min, 25 $^{\circ}\text{C}$).

6.2.5 Time-resolved Fluorescence

The fourth harmonic (293 nm) of an optical parametric amplifier (Light Conversion) pumped by a regeneratively amplified femtosecond Ti:sapphire laser (1 kHz, Clark-MXR) and a picosecond streak camera (Hamamatsu) were used as the excitation source and detector, respectively for time-resolved measurements. Trp emission (325 – 400 nm) was selected through using edge (REF-325) and short-pass (UG-11) filters (CVI Laser). For time-resolved anisotropy measurements, polarized Trp (I_{\perp} and I_{\parallel} , 325-400 nm) excited-state decays were collected simultaneously with an optical fiber array. Fluorescence anisotropy decays were calculated and analyzed according to the following equations (Eq. 6.2 and 6.3, respectively) where r_0 is the apparent anisotropy at $t=0$ and ϕ_c is the rotational correlation time resulting from depolarization:

$$r(t) = \frac{I_{\parallel}(t) + I_{\perp}(t)}{I_{\parallel}(t) + 2I_{\perp}(t)} \quad (6.2)$$

$$r(t) = r_0 \exp(-t/\phi_c) \quad (6.3)$$

6.2.6 Tryptophan Quenching

Tryptophan quenching measurements were made on a Fluorolog 3 fluorimeter (Horiba Jobin Yvon; $\lambda_{\text{ex}} = 280$ nm, $\lambda_{\text{obs}} = 300 - 500$ nm, 0.3 s integration time, 1 nm bandwidths, 25 °C) in the presence and absence of increasing amounts of acrylamide (0 - 87.5 mM). Aliquots of an 8 M acrylamide stock solution (deionized water, filtered 0.22 μm) were added in increments (< 5 μL) to 1.5 mL samples to minimize dilution. For all experiments, samples were equilibrated for one minute while stirring at 25 °C prior to measurement. Quenching data were analyzed according to the Stern-Volmer equation, $\frac{I}{I_o} = 1 + K_{\text{SV}}[Q]$, where I_o and I are the fluorescence intensities recorded in absence and presence of acrylamide, K_{SV} is the Stern-Volmer constant, and $[Q]$ is acrylamide concentration.

6.2.7 pH Titration Data Analysis

Mean wavelength $\langle \lambda \rangle$ was determined according to the equation $\langle \lambda \rangle = \frac{\sum_i I_i \lambda_i}{\sum_i I_i}$

where I_i and λ_i is the emission intensity and wavelength, respectively, for $i = 300 - 500$ nm. Integrated intensity (I) of W423 emission was determined according to trapezoidal integration. Using $\langle \lambda \rangle$ data, apparent $\text{p}K_a$ and the number of ionization events involved in the process, n , were extracted from fits to the Henderson-Hasselbalch equation:

$$\langle \lambda \rangle = 1 - \frac{(\langle \lambda \rangle_{\text{neutral}} + \langle \lambda \rangle_{\text{acid}} 10^{n(\text{p}K_a - \text{pH})})}{1 + 10^{n(\text{p}K_a - \text{pH})}} \quad (6.4)$$

where $\langle \lambda \rangle_{neutral}$ and $\langle \lambda \rangle_{acidic}$ are the W423 fluorescence mean wavelengths at neutral (≥ 6.0) and acidic (≤ 4.0) pH, respectively. Data fitting and trapezoidal integration was performed using IGOR Pro 6.01 (Wavemetrics).

6.3 Results and Discussion

6.3.1 RPT Amyloid Structure and Aggregation Kinetics

The RPT primary amino acid sequence is comprised of 10 imperfect 13 residue repeats that are rich in proline, serine, threonine, and glutamic acids (Figure 6.1). RPT contains 16 carboxylates underscoring its propensity to undergo pH induced conformational changes. Because pH and protein conformation likely are linked *in vivo* (*vide supra*), we employed TEM, static light scattering, and a ThT fluorescence assay²¹⁴ to determine the effects of pH on RPT amyloid formation (Figure 6.2). As fibril formation processes generally exhibit sigmoidal kinetic behavior characterized by a lag, growth, and stationary phase,⁷ we made frequent light scattering measurements during each of these phases. TEM was used as a probe of macroscopic morphology before and during the initial growth phase, and then again after aggregation was completed (stationary phase). As it is typical for amyloid formation kinetics, we observed sample-to-sample variations in the lag phase, during which time little or no apparent changes in fibril concentration can be detected.²¹⁵ However, despite greater uncertainties in the absolute lag times, we ascertained that the pH dependent trends (*e.g.* relative aggregation rates and respective spectroscopic signals) as well as corresponding fibril morphologies were comparable and reproducible. Specifically, aggregation kinetics are accelerated from pH 5.5 (20 – 30

h) to 4.0 (< 1 h). We find that fibrils are formed only below pH 6.0, consistent with previous observation that RPT fibrils will dissolve in near neutral and basic solutions.²⁰⁹ Further, the morphology and homogeneity of fibrils formed at pH 4.0 and 5.5 are distinctive from each other and apparently more uniform than those formed under intermediate pH conditions (4.5 – 5.0).

At pH 5.5, aged RPT forms long and homogenous fibrils that have moderate ThT fluorescence and light scattering signals (Figure 6.2, top). TEM images show that no oligomers are formed prior to incubation. At the beginning of the fibril growth phase (after 20 – 30 h of incubation at 37 °C and shaking at 600 rpm), a few large laterally associated small fibrillar species (~ 70 nm in average length) appear. After growth is complete (~ 60 – 100 h), we find primarily straight and long fibrils (> 1 µm) approximately 18 nm in width reflecting significant restructuring between early growth and stationary aggregation phases.

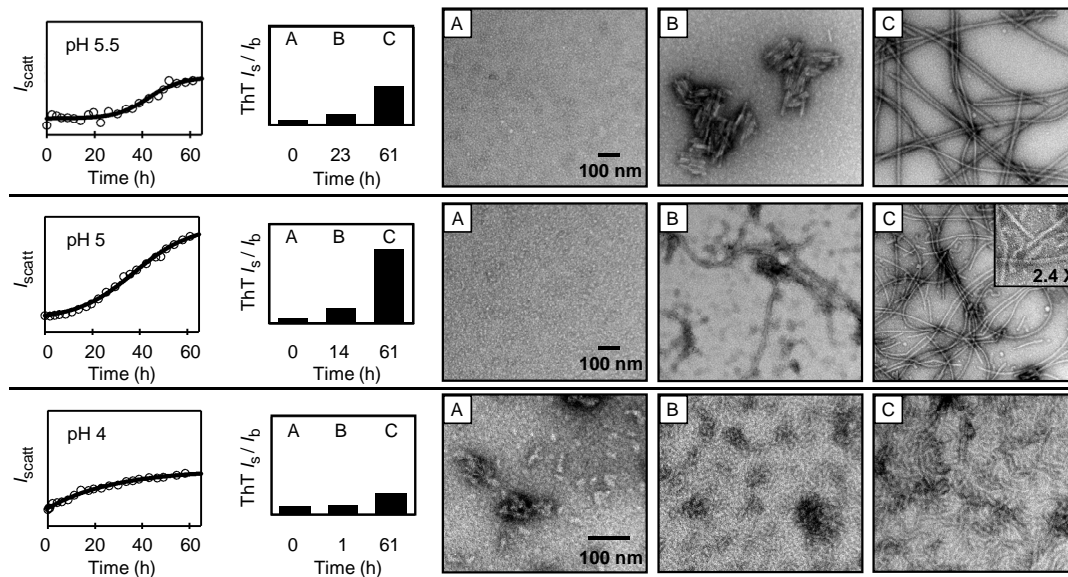


Figure 6.2 pH dependence of RPT aggregation kinetics and amyloid structures. Laser light scattering (left), thioflavin T assay (middle), and transmission electron microscopy images (right) of RPT (30 μ M) as a function of incubation time at 37 $^{\circ}$ C with agitation (600 rpm) in buffers pH 5.5 (top), 5.0 (middle), and 4.0 (bottom) buffers (20 mM sodium acetate and 100 mM NaCl). Laser light scattering intensity is denoted as I_{scatt} and integrated intensity of ThT emission of RPT sample and buffer alone are denoted as I_s and I_b , respectively. ThT and scattering values are in arbitrary units; y-axis range is the same for respective scattering and ThT data.

In slightly more acidic environments (pH 5.0 – 4.5), differences in aggregation kinetics and fibril morphologies are revealed. Greater light scattering and ThT signals are observed as well as increased fibril heterogeneity (Figure 6.2). By the beginning of the growth phase (~ 10 – 15 h) a heterogeneous species appears, containing both fibrillar and amorphous structures of varying sizes and shapes. These early aggregates finally give rise to primarily long (> 1 μ m) and short (~ 125 nm) straight fibers as well as sharply curved fibrous structures (Figure 6.2, right inset). At this intermediate pH, RPT is likely sampling multiple conformations resulting in several distinct intermediates leading to polymorphic fibrils.

In contrast, at the most acidic pH examined (4.0) RPT rapidly aggregates (< 1 h) with large preformed oligomers observed at initial measurement. While the aggregates form immediately, our TEM images show that there is no conversion to the longer fibrils over time (Figure 6.2, bottom). These data indicate that RPT adopts a conformation leading to alternative oligomeric structures that preclude fibril elongation. We note that the initial aggregates exhibit a low initial ThT signal that increases modestly upon aging (~ 90 h). This increase suggests that while there are no long fibrils, the mature aggregates do contain some amyloid-like features. While CD spectroscopy confirms that all aged samples below pH 6.0 exhibit β -sheet secondary structure (Figure 6.3), pH 4.0 samples have a slightly reduced mean residue ellipticity below 217 nm, reflecting increased random coil content.

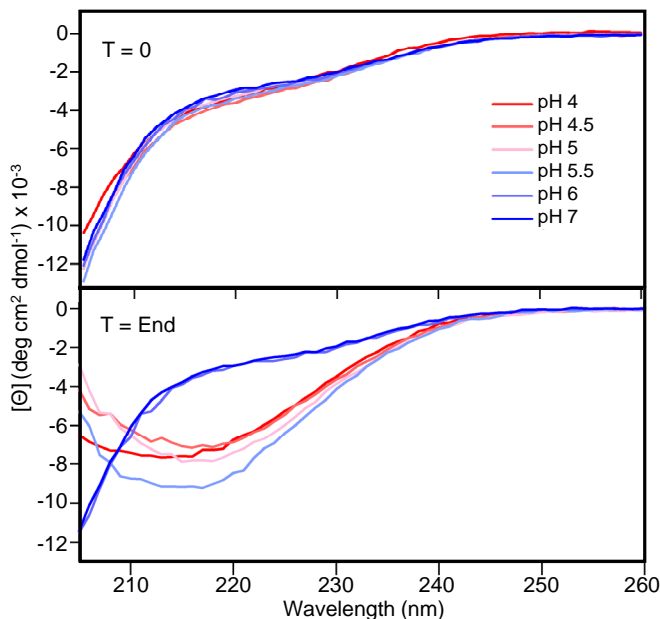


Figure 6.3 Secondary structure of soluble and aged RPT. Circular dichroism spectra for RPT at the beginning ($T = 0$) and end ($T = \text{End}$; > 80 h) of aggregation experiments in different pH buffers (pH 4.0 – 5.5: 20 mM sodium acetate, 100 mM NaCl, pH 6.0: 20 mM MES, 100 mM NaCl and pH 7.0: 20 mM MOPS, 100 mM NaCl).

6.3.2 Critical Concentration for RPT Aggregation at pH 5.0

To determine the critical concentration (concentration below which aggregation will not occur) for RPT we examined the aggregation kinetics at pH 5 as a function of protein concentration. At this pH, we find that amyloid can form at concentrations as low as 2 μM . This value likely represents an upper limit given that we are at the current detection limit of our light scattering apparatus. RPT aggregation kinetics exhibit protein concentration dependent growth rates with similar lag times (Figure 6.4). Though not precluding concentration dependent lag phases at concentrations $< 2 \mu\text{M}$, these results may reflect an alternative aggregation mechanism^{7,216,217} other than nucleation/polymerization,²¹⁸ the common mechanism for disease-related amyloid formation processes.²¹⁷ The lack of lag time reduction as a function of protein concentration could also indicate that the critical RPT concentration is extremely low.

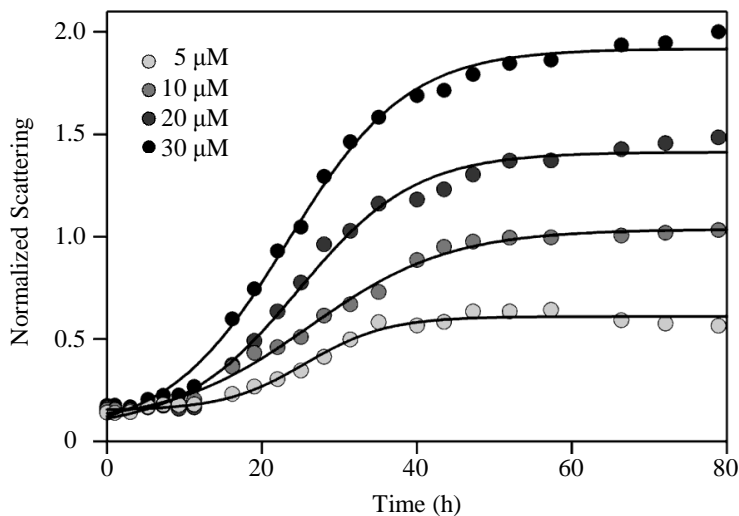


Figure 6.4 Concentration dependence of RPT amyloid formation. RPT amyloid formation kinetics monitored by laser light scattering ($\lambda_{\text{ex}} = 450 \text{ nm}$) for $[\text{RPT}] = 5 - 30 \mu\text{M}$ in 20 mM sodium acetate, 100 mM NaCl buffer, pH 5.0 incubated at 37 $^{\circ}\text{C}$ with agitation (600 rpm). Solid lines serve to guide the readers.

6.3.3 W423, a Site-specific Probe of RPT Conformation

We sought to determine how pH influences local protein conformation by fluorescence measurements of the only intrinsic tryptophan in RPT, W423, as a function of solution pH. W423 serves as an excellent structural probe as there are two nearby carboxylates and ~40% of the total carboxylates residing in the last two repeat domains (Figure 6.1). Prior to thermal incubation ($T = 0$), we observe variations in the steady-state W423 emission as the solution pH is lowered ($7 \rightarrow 4$) (Figure 6.5). These changes demonstrate that protonation of C-terminal carboxylates indeed affect local protein conformation.

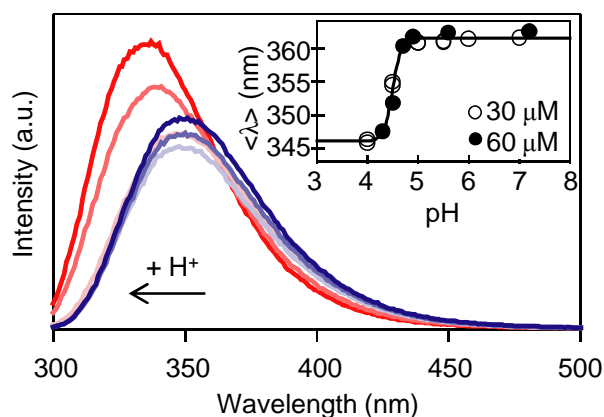


Figure 6.5. pH dependence of W423 emission spectra for RPT. W423 emission spectra for RPT (60 μ M) in pH 4.0 – 7.3 (red-to-blue respectively) buffers (pH 4.0 – 5.6: 20 mM sodium acetate, 100 mM NaCl, pH 6.0: 20 mM MES, 100 mM NaCl and pH 7.0 – 7.3: 20 mM MOPS, 100 mM NaCl). Inset: Mean wavelength, $\langle \lambda \rangle$, of W423 for RPT (30 and 60 μ M) in various pH buffers. Fit is shown as a solid line.

At neutral pH, W423 emission indicates a solvent-exposed indole with a mean wavelength ($\langle \lambda \rangle$) of 362 nm comparable to a model complex, N-acetyl-tryptophanamide ($\langle \lambda \rangle = 365$ nm). In more acidic environments, W423 emission blue

shifts (Table 6.1), with an apparent midpoint transition at pH 4.5. As evidenced by TEM (Figure 6.2), spectral blue shifts reflect a more hydrophobic environment for W423 as protein-protein contacts ensue at pH 4.0.

Table 6.1 Spectral properties of soluble vs. fibrillar RPT at different pH

pH ^c	<i>Soluble</i> ^a		<i>Fibrillar</i> ^b	
	$\langle\lambda\rangle$ (nm) ^d	I_{rel} (a.u.) ^e	$\langle\lambda\rangle$ (nm) ^d	I_{rel} (a.u.) ^e
4.0	349	1.19	343	1.41
4.3	348	1.21	344	1.37
4.5	354	0.91	344	1.14
4.7	360	0.86	346	1.20
5.0	360	0.86	347	0.60
5.5	361	0.94	352	0.37
5.6	362	0.85	355	0.44
6.0	361	0.90	361	0.84
7.0	361	0.95	362	0.93
7.2	362	0.92	363	0.93

^a Soluble data was collected prior to sample incubation ($T = 0$).

^b Fibrillar data was collected for all samples after the stationary phase of aggregation had been reached for pH 4 - 5.5 ($T > 50$ h). No aggregates or fibrils are formed at $\text{pH} \geq 6$.

^c Buffers: pH 4.0 – 5.6: 20 mM sodium acetate, 100 mM NaCl, pH 6.0: 20 mM MES, 100 mM NaCl and pH 7.0 – 7.3: 20 mM MOPS, 100 mM NaCl.

^d Systematic error in Trp423 mean wavelength (λ) is estimated to be $\sim \pm 1$ nm. For cases in which $n \geq 2$ (pH 4.0, 4.5, 5.0, 5.5, 6.0) an average value for $\langle\lambda\rangle$ is reported.

^e Integrated intensities (I) are normalized to the emission of a model fluorophore, N-acetyl-tryptophanamide to account for any variations due to lamp power fluctuations. This relative I , or I_{rel} , is given by

the following equation: $I_{rel} = \frac{I_{sample}}{I_{NATA}}$, where I_{sample} and I_{NATA} are the integrated steady state

emission spectrum of the sample and NATA, respectively. For cases in which $n \geq 2$ (pH 4.0, 4.5, 5.0, 5.5, 6.0) an average value for I is reported.

W423 also exhibits pH dependent changes in integrated emission intensity, I , with a small decrease from pH 7 to 5.5 and a substantial increase from pH 5.5 to 4.0

(Figure 6.5). Trp fluorescence quantum yields are known to be modulated in the presence of charged residues, with proximity to positive (negative) charges corresponding to quantum yield increase (decrease).⁵² It is plausible that observed I changes could reflect nearby carboxylate protonation states as well as intra- and/or interprotein conformational changes. To shed light on these possibilities, we used dynamic light scattering measurements to assess the RPT molecular dimensions as a function of pH. We find that there is a pH dependent global structural change (diffusion coefficient for pH 4.0 > 5.0 ~ 6.0) consistent with the presence of larger oligomers at pH 4 (Figure 6.6). These results support that W423 spectroscopic changes are sensitive to overall protein conformation as well as its molecular environment.

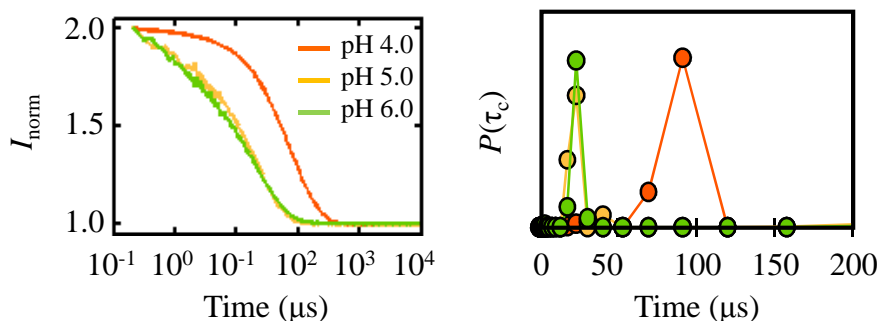


Figure 6.6 pH dependence on size of soluble RPT. (Left) Dynamic light scattering autocorrelation curves for RPT at pH 4.0 (red), 5.0 (yellow), and 6.0 (green). (Right) Relative probabilities for correlation times $P(\tau_c)$ of RPT under pH 4.0, 5.0, and 6.0 buffer conditions.

Using the Henderson-Hasselbalch equation, we obtain a $pK_a \sim 4.5$ (Figure 6.5, Inset). We find the involvement of at least 3 protons (n) in this process (5 protons yielded the best fit; however, adequate fits can be obtained for $n \geq 3$), which

is reasonable given the close proximity of W423 to several carboxylates (6 total in repeat 9 and 10). CD spectroscopy confirms that for all solutions conditions examined, RPT is unstructured with only minor differences below 230 nm (Figure 6.3) demonstrating the utility of W423 to detect even small changes in solution conformations.

6.3.4 W423, a Site-specific Probe of RPT Amyloid Formation

Subsequent conformational changes and protein-protein interactions during aggregation also were monitored by W423 as a function of incubation time (37°C, 600 rpm). The temporal evolution (0 – 90 h) of W423 steady-state fluorescence for RPT is shown in Figure 6.7. At and above pH 6.0, W423 emission is unchanged for the duration of the experiment demonstrating that RPT remains unstructured and monomeric. However, for all acidic conditions (< 6.0), distinct and time dependent W423 changes in integrated intensity and spectral shifts are observed. Initially, W423 emission for pH 5.5 is nearly identical to that observed for pH 6.0; however, during the growth phase (after ~ 40 – 50 h) *I* drops dramatically and a spectral blue shift is observed ($\Delta\langle\lambda\rangle = 10$ nm; 362 → 352 nm). As the pH is lowered to 5.0, an increased blue shift ($\Delta\langle\lambda\rangle = 14$ nm; 362 → 348 nm) as well as a moderate decrease in *I* is observed by ~ 20 – 30 h (during growth phase). Indeed, time-resolved anisotropy (Figure 6.8) and acrylamide quenching (Figure 6.9) data confirm that at pH 5.0, W423 in the fibrillar state exhibits reduced local mobility and greater solvent protection (K_{sv} (pH 5.0) = 10(1) M⁻¹; K_{sv} (NATA) = 34(5) M⁻¹) as compared to initial measurement (K_{sv} (pH 5.0) = 22(2) M⁻¹). Reflecting faster kinetics, W423 in pH 4.5 solution exhibits a blue shift comparable to that observed at higher pH ($\Delta\langle\lambda\rangle = 13$

nm; 355 → 342 nm) within the first 10 h of incubation. In contrast to other conditions, at pH 4.5, W423 exhibits a significant I increase with only a small decrease after ~ 40 h of incubation. At the lowest pH, we observed rapid RPT oligomerization with a high I and blue shifted spectrum at our earliest measurement ($t = 15$ min). While W423 emission continues to blue shift and increase in I , spectral changes are completed within 5 h.

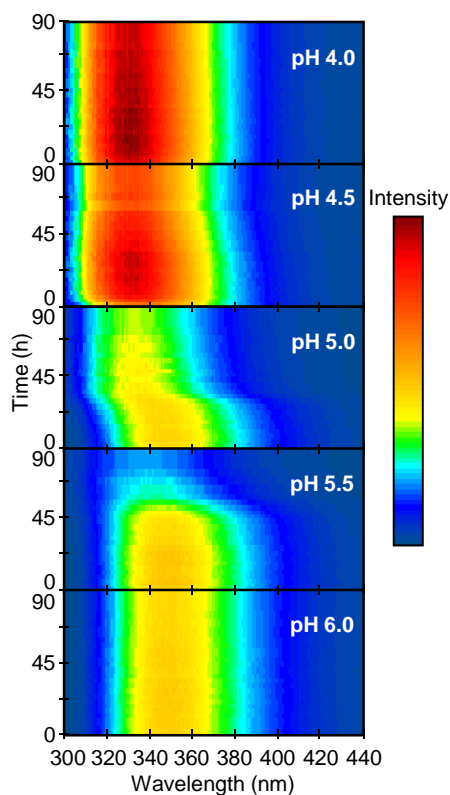


Figure 6.7 W423 emission intensity surfaces as a function of pH (4-to-6, top-to-bottom). RPT (30 μ M) emission surfaces are plotted as a function of the aggregation time (0 – 90 h) and wavelength (300 – 440 nm). Trp423 emission intensity is in arbitrary units (red-to-blue) normalized to the highest intensity (pH 4.0).

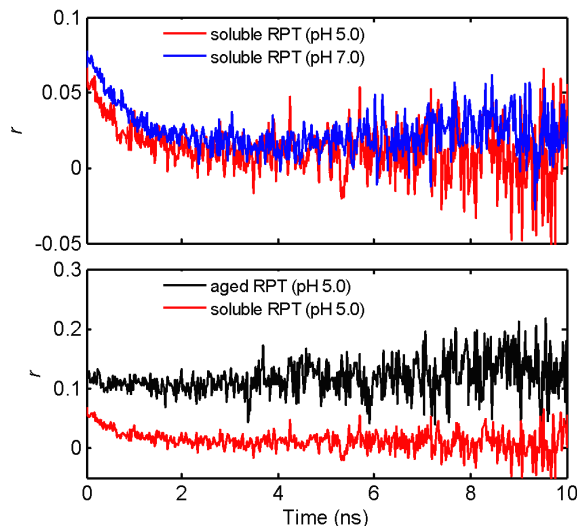


Figure 6.8 Time-resolved anisotropy measurements for RPT. (Top) Comparison between RPT in pH 5.0 (20 mM NaOAc, 100 mM NaCl) and pH 7.0 (20 mM MOPS, 100 mM NaCl) buffer. From fits to data an initial anisotropy (r_0) and correlation time (ϕ_c) of $r_0 \sim 0.05$, $\phi_c \sim 0.6$ ns and $r_0 \sim 0.04$, $\phi_c \sim 0.8$ ns were determined for pH 5 and pH 7, respectively (see Materials and Methods). (Bottom) Comparison between soluble and aged (~ 143 h at 37 °C, 600 rpm) RPT samples at pH 5.0.

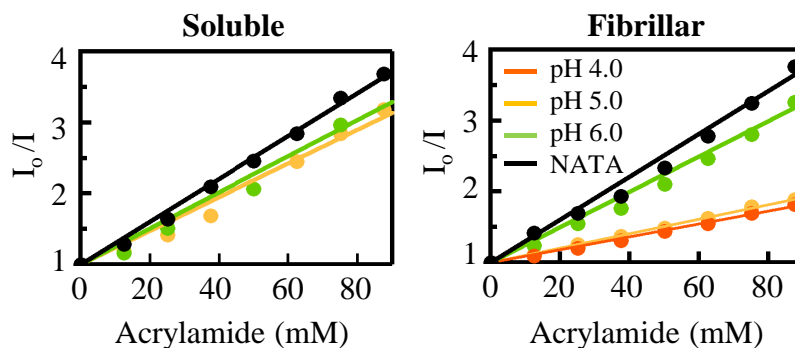


Figure 6.9 Acrylamide quenching for soluble ($T = 0$) and fibrillar RPT ($T > 50$ h) and N-acetyl-L-tryptophanamide (NATA, pH 5.0). For all experiments, $[RPT] = 30$ μ M (pH 4.0 and 5.0, 20 mM sodium acetate, 100 mM NaCl, pH 6.0: 20 mM MES, 100 mM NaCl). Data for NATA and RPT at pH 4.0, 5.0, and 6.0 are designated by black, red, yellow, and green, respectively. Fits to Stern-Volmer equation are shown as solid lines.

6.3.5 Tryptophan Fluorescence Reflects Fibril Morphologies

We found correlations between W423 spectral changes and amyloid morphology. In all cases for which a W423 decrease in I is observed (pH 4.5 – 5.5), distinct fibrillar species are also present. Measurements of W423 excited state decays are consistent with steady state data showing that the average fluorescence lifetime is decreased in the amyloid form for pH 5 (Figure 6.10). Specifically, decreases in I are most pronounced at pH 5.0 – 5.5 and commence during the growth phase when fibrils first appear. Further, at pH 4.5 long fibrils are only present after the small decrease in I commences (~ 40 h). Contrastingly, we find an increase rather than a reduction in W423 I at pH 4.0 and accordingly no long fibrillar species present. We suggest that this fluorescence signature (I decrease) could be attributable to Trp–Trp stacking, possibly resulting from a parallel in-register β -sheet conformation. We propose this fibrillar structure, where corresponding residues of adjacent polypeptides (W423–W423) are aligned in individual β -strands, because this is a common feature of several amyloidogenic proteins.^{219,220} While Trp-Trp stacking would explain the observed decreases in W423 intensity upon fibril formation, it is also reasonable that local molecular interactions and/or changes in environment could facilitate other quenching mechanisms.

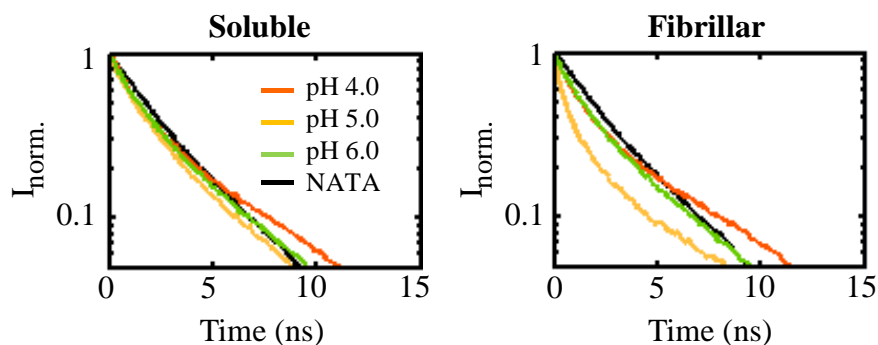


Figure 6.10 pH dependence of time-resolved Trp fluorescence for soluble and fibrillar RPT and N-acetyl-L-tryptophanamide (NATA, pH 5.0). For all experiments, [RPT] = 30 μ M (pH 4.0 and 5.0, 20 mM sodium acetate, 100 mM NaCl, pH 6.0: 20 mM MES, 100 mM NaCl).

We attribute the spectral blue shifts and increased I at low pH (< 4.5) to reflect an increased hydrophobic local environment upon protein oligomerization. Bimolecular acrylamide quenching data ($K_{sv} = 10(1) \text{ M}^{-1}$, pH 4.0) are consistent with a polypeptide structural rearrangement in which W423 is sequestered from the aqueous environment. Additionally, the I increases in the oligomeric state could reflect intra- or interprotein contacts that promote W423 interaction with positively charged residues (K378 and R429, [Figure 6.1](#)). We favor R429 because of its closer proximity to W423.

Regardless of the exact nature of these distinguishing spectroscopic features, it is clear that W423 is an exquisite probe of RPT amyloid formation and has provided kinetic information that is not available from other measurements. We note that while Trp fluorescence has been used to report on the amyloid formation process for the disease-related polypeptides α -synuclein^{221,222} and $A\beta_{1-40}$,²²³ large changes in $\langle\lambda\rangle$ and I are not always observed and are highly site-dependent. Particularly, W423

highlights an important role for the C-terminal repeats in RPT fibril growth. Supplementary lines of evidence also support that the RPT amyloid core likely involves the C-terminal repeats: (1) amyloid-structure destabilizing proline residues are found primarily between repeats 1 to 7 and repeat 10;²²⁴ (2) *in vivo*, repeats 2-3 are known to be heavily *O*-glycosylated with highly charged sialylated glycans which would add steric constraints within the N-terminal domain and therefore less likely to contribute to amyloid assembly;^{205,225} (3) the amyloid sequence predictor Waltz indentified ⁴⁰³AEVSIVVL⁴¹⁰, located within repeats 7 and 8, as the most amyloidogenic sequence.²²⁶

6.4 Implications

Our data clearly show that solution pH affects both RPT aggregation kinetics and fibril morphology with W423 reporting on the local conformational changes corresponding to observed ultrastructures. By comparison of equilibrium pH dependent W423 data we find that the pK_a of aggregated samples is shifted from 4.5 to 5.5 (Figure 6.11). This shift is reasonable given that it would be more favorable to have neutral rather than charged groups buried within the hydrophobic amyloid core. Therefore, protonation is facilitated upon aggregation. In contrast to protonation of the soluble protein, this process in the fibril involves only one ionizable group rather than multiple ones, suggesting that a specific carboxylate is responsible for fibril formation/stability.

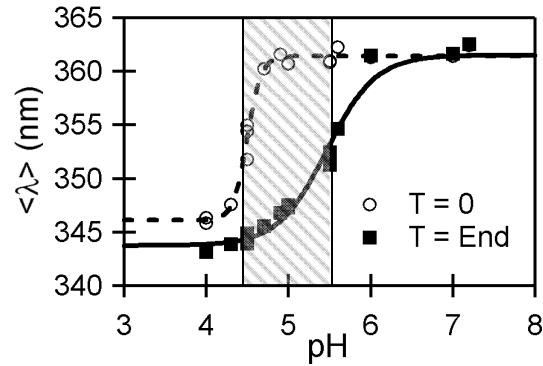


Figure 6.11 Comparison of critical pH regimes for soluble and fibrillar RPT. Mean wavelength, $\langle \lambda \rangle$, of W423 in different pH buffers (pH 4.0 – 5.6: 20 mM sodium acetate, 100 mM NaCl, pH 6.0: 20 mM MES, 100 mM NaCl and pH 7.0 – 7.3: 20 mM MOPS, 100 mM NaCl) of RPT samples at the beginning (T = 0) and end (T = end) of aggregation. Solid lines are fits. Critical amyloid formation pH is identified to be pH 4.5 – 5.5 (shaded area).

Because pH is critical in mediating RPT solution conformation and aggregation processes, we hypothesize that the changes in pH that occur during melanosome maturation provide one potential natural regulator of Pmel17 amyloid formation. To test this hypothesis, we monitored fibril morphological and local polypeptide conformational changes upon pH titration of aggregated RPT from pH 4 \rightarrow 5 \rightarrow 7 through TEM and W423 fluorescence (Figure 6.12). In the preformed aggregate at pH 4 ([RPT] = 30 μ M for 72 h at 37 $^{\circ}$ C, 600 rpm), the Trp indole is mostly solvent-protected ($\langle \lambda \rangle$ = 343 nm; K_{sv} = 10(1) M^{-1}). Upon sequential solution neutralization spectral red shifts (343 \rightarrow 350 \rightarrow 360 nm) and integrated intensity decreases are observed from pH 4 \rightarrow 5 \rightarrow 7, similar to that of the RPT samples independently prepared and aged (Figure 6.7). Interestingly, the observed fibril morphological changes from small, indistinct to long, striated fibrils are rapid ($<$ 10 min, 25 $^{\circ}$ C) and are reminiscent of those observed in stage I (pH 3 – 4) and II (pH 4.6

– 5) melanosomes.^{13,195} Further neutralization to pH 7 results in almost complete dissolution of fibrillar RPT, supporting a highly reversible aggregation-disaggregation process. It is this feature that makes RPT amyloid unique as disease-related fibrils are extremely difficult to dissolve even upon enzymatic digestion and detergent denaturation.²²⁷

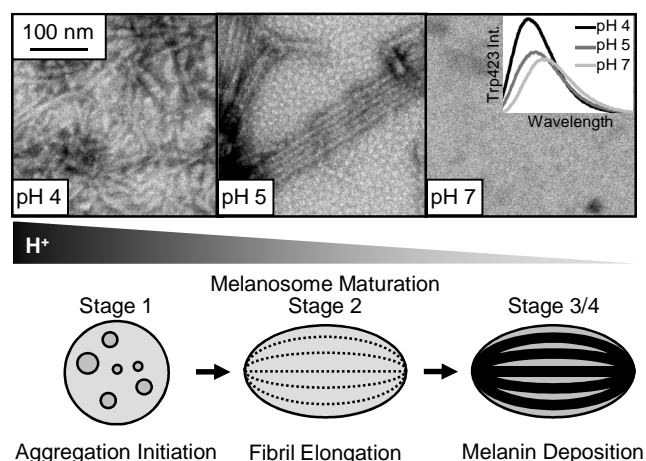


Figure 6.12 pH induced RPT fibril morphological conversion and the melanosome maturation process. TEM images (top) of aggregated RPT at pH 4 (20 mM sodium acetate, 100 mM NaCl, left), after adjusting the pH to 5 (after 10 min, middle), and to 7 (after 10 min, right). Corresponding W423 steady-state emission spectra are shown in the inset. Schematic representation (bottom) of pH dependence of melanosome maturation: stage I, protein aggregation is initiated; stage II, fibrils elongate; stages III/IV, melanin deposition occurs.

Based on our results, we propose in the highly acidic melanosome (stage I), protein aggregation is initiated with fibril elongation occurring only after the compartment solution reaches an optimized pH \sim 5 (stage II). Upon protonation of specific carboxylates, the electrostatic charge repulsion within the polypeptide chain reduces, thereby leading to formation of compact structures that promote key interactions required for fibril formation. In addition, our observation that RPT will

readily aggregate ($\leq 2 \mu\text{M}$) at the optimized pH (5.0) could suggest that only fibrils are stabilized in lieu of potentially toxic oligomers.¹⁹⁴ While our data show that fibrils would dissolve in the near neutral conditions (pH 6 and above) found in stage III and IV melanosomes, it is unclear whether upon melanin deposition, the polymeric material could sequester the fibrils from solution and hence protect them from dissolution. Nevertheless, if released and exposed to the neutral environments outside the melanosome, fibrils will readily disintegrate and thus maintain their benign nature in the body.

6.4 Summary

We have determined the effects of solution pH (4 \rightarrow 7), mimicking pH conditions of melanosomes, on the solution conformation and aggregation kinetics of the RPT domain of Pmel17. Using intrinsic Trp423 fluorescence, a highly sensitive probe of amyloid assembly, we have identified specific spectral features reflecting local conformational and macroscopic fibril morphological changes. A critical pH regime (5 ± 0.5) was identified for fibril formation suggesting the involvement of at least three carboxylic acids in the structural rearrangement necessary for aggregation. Moreover, we demonstrate that RPT fibril morphology can be transformed directly by changing solution pH. Based on these results, we propose that intramelanosomal pH regulates Pmel17 amyloid formation and its subsequent dissolution *in vivo*.

Appendix 1: Instrumentation

A1.1 Time-resolved Fluorescence

Time-resolved measurements were made using the output of an optical parametric amplifier (OPA) (Light Conversion) pumped by a regeneratively amplified femtosecond Ti:sapphire laser (1.3 W, 1 kHz, 150 fs, Clark-MXR) and a picosecond streak camera (Hamamatsu) for detection. To ensure monochromatic excitation of the sample, aberrant photons are separated from those of the desired wavelength by subjecting the OPA output beam to a Pellin Broca prism. Coarse adjustments to excitation power are made using a Berek polarization compensator (New Focus) in conjunction with a linear polarizer. To ensure elimination of polarization bias in time-resolved measurements, the linear polarizer is set to the “magic angle” condition of 35.25° from vertical.²²⁸ Fine power adjustments are made with a neutral density filter. Typical final sample excitation powers are 20 – 150 μW (292 nm) for single tryptophan containing samples (5 μM). Samples contained in 1 cm pathlength quartz cuvettes are placed in an excitation beam focused behind the sample and fluorescence emission collected at 90° geometry using a biconvex lens allowing for one to one imaging of the excitation volume onto an optical fiber array. A schematic representation of the time-resolved instrumental setup is provided in [Figure A1.1](#).

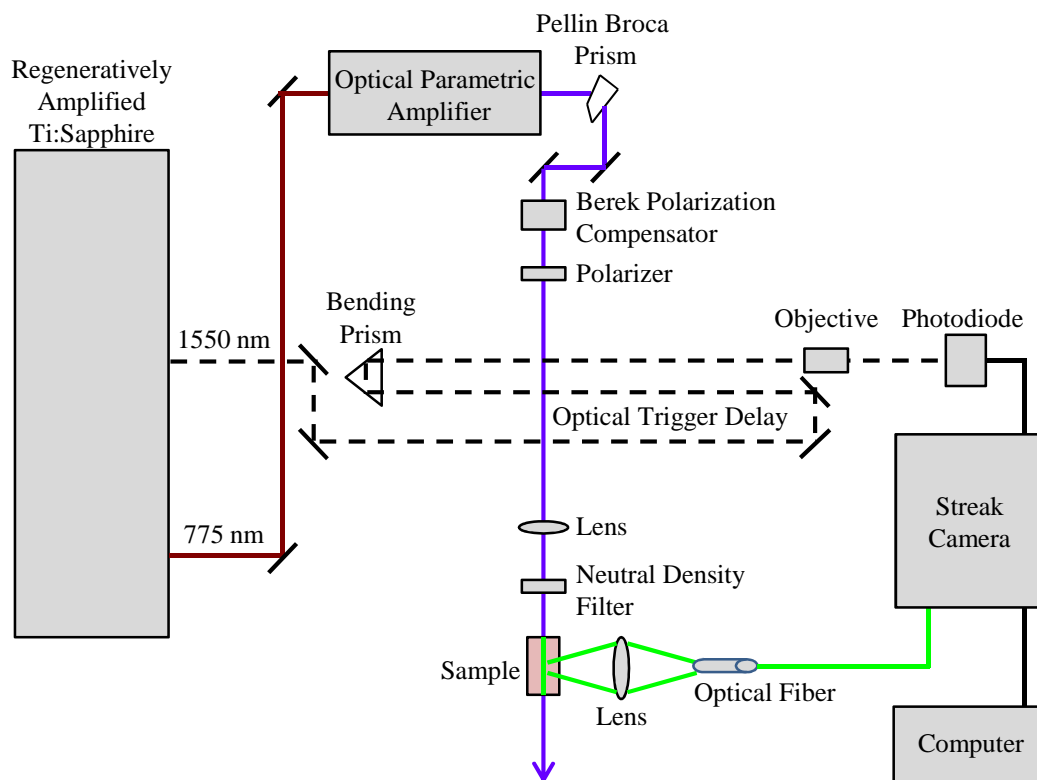


Figure A1.1: Schematic representation of the femtosecond Ti:Sapphire and streak camera setup used to measure time-resolved fluorescence and anisotropy decays.

Emission is focused on the entrance slit of the streak camera which spatially and temporally separates the photons (Figure A1.2). Briefly, incident photons are converted to electrons at the photocathode. The electrons are then accelerated in-between a pair of high voltage sweep electrodes. The voltage gradient across the electrodes causes deflections in the electrons proportional to the time and location in which electrons entered the voltage gradient. The spatially and temporally resolved electrons then enter a multichannel plate (MCP) where they are enhanced and imaged on a phosphor screen. An example digitized streak image used for data analysis is provided in Figure A1.3 (left). These 3D images contain information regarding the intensity, time, and location of photons. Images can be binned in the spatial

coordinate to generate 2D (intensity vs. time) fluorescence decay curves (Figure A1.3, right). For time-resolved data collection, the streak camera is operated in single shot mode with parameters for single tryptophan containing samples (5 μM) set as follows: threshold = 300, 111 ms exposure time, 2000 – 5000 exposures. At these settings, the highest emission intensity is between 3% – 5% above threshold.

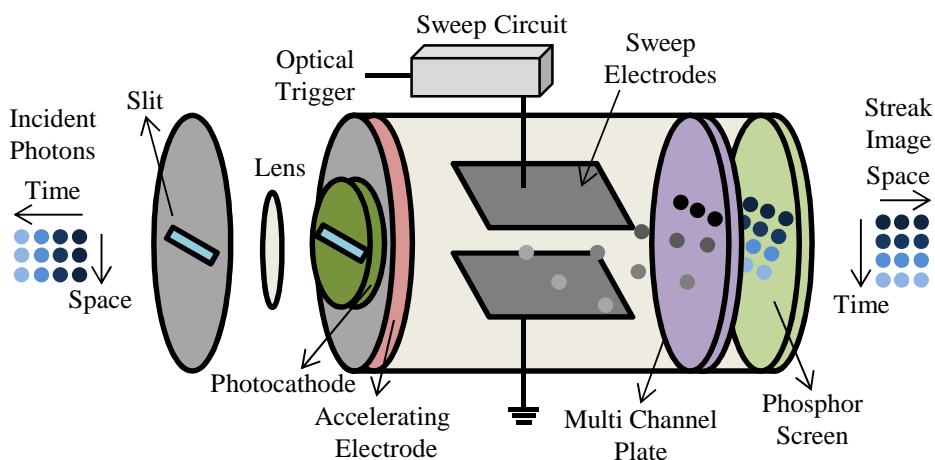


Figure A1.2: Schematic representation of the streak camera.

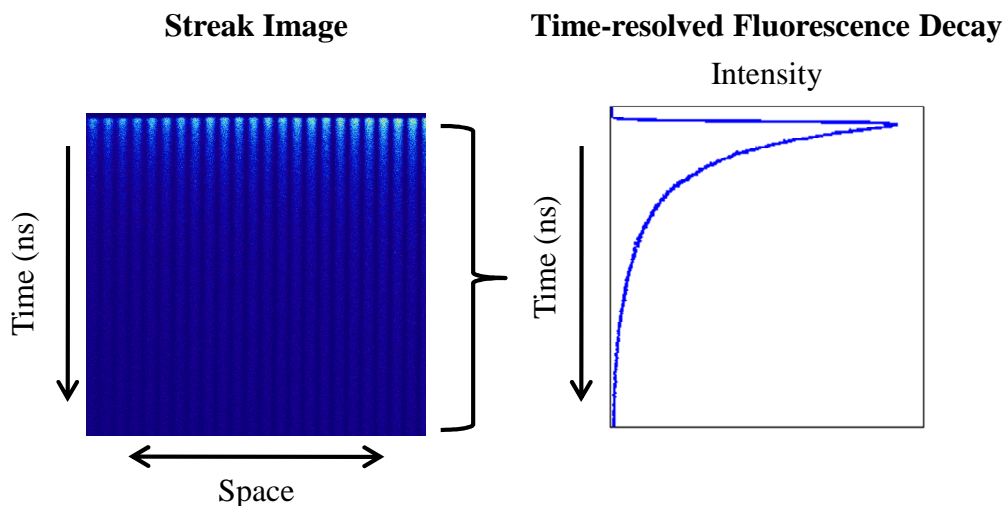


Figure A1.3: An image of the emission of a fluorescent protein sample generated by the streak camera (left). By binning data in the spatial coordinate, a 2D (intensity vs. time) fluorescence decay curve is generated (right).

To ensure synchronization of the camera voltage sweep with sample excitation pulses, an optical trigger is used. Under the conditions used for experiments (single shot mode), the camera only accepts a sample excitation pulse after a trigger signal is received. The camera resets and accepts subsequent trigger pulses at a 1kHz repetition rate using the sync out signal from the Ti:Sapphire laser. The output of the fiber laser used to seed the regeneratively amplified Ti:Sapphire (1550 nm, 48MHz) is exploited as the optical trigger (Figure A1.1). Because the fiber laser and sample excitation pulses are coupled, one can finely tune the respective time between the start of the camera sweep and the time of the incident sample pulse by changing the relative delay between the trigger and sample excitation pulses. One method to make this adjustment is by using an optical delay line (*i.e.* increasing or decreasing the distance the trigger pulse travels). For example, since the speed of light is 3.0×10^8 m/s, adding an additional 1 m to the optical path of the trigger beam would result in pulses shifted approximately 3.3 ns.

A1.2 Time-resolved Fluorescence Anisotropy

To calculate fluorescence anisotropy, a sample must be excited with vertically polarized light and the vertical and horizontal components of the fluorescence emission measured. Selection of vertical excitation light can easily be achieved by adjusting the linear polarizer adjacent to the Berek polarization compensator to the vertical position ($\theta = 0^\circ$) (Figure A1.1). Vertical and horizontal components of emission can be simultaneously measured by exploiting the unique ability of the streak camera to collect time-resolved information in the spatial dimension (*vide supra*). Specifically, the optical fiber array consists of individual optical fibers (100

μm) aligned linearly across a 1 cm length. By placing two linear polarizers (vertical, $\theta = 0^\circ$; horizontal, $\theta = 90^\circ$) in front of the optical fiber array, simultaneous vertical and horizontal fluorescence decays can be collected (Figure A1.4, left). An example streak camera image of anisotropy data is provided in Figure A1.4 (right). To correct for any differences in the collection efficiency between horizontal and vertical components, all data are normalized to the decays of the Trp model complex, N-acetyl-tryptophanamide (NATA). For tryptophan anisotropy measurements of singly labeled tryptophan proteins (5 μM), sample excitation power is usually 100 – 300 μW (292 nm) with streak camera parameters set as follows: threshold = 300, 111 ms exposure time, and 5 sequences of 2500 exposures collected.

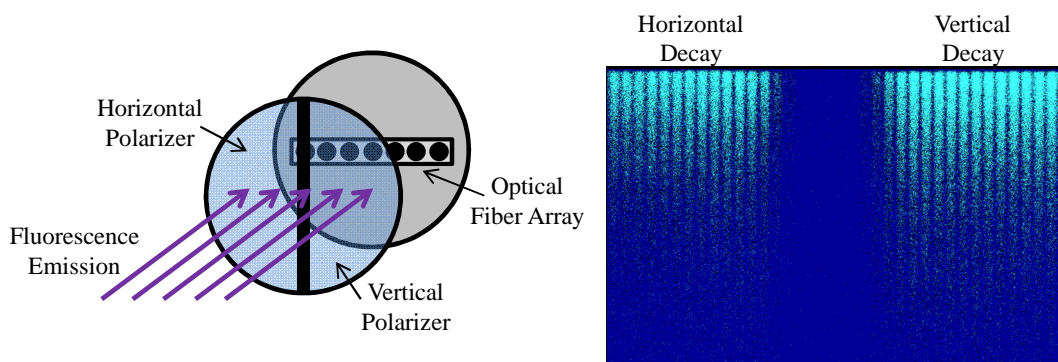


Figure A1.4: Time-resolved anisotropy data collection. (Left) A schematic representation of the two linear polarizers placed before the optical fiber array used to collect simultaneous vertical and horizontal components of the emission. (Right) An example image generated by the streak camera of anisotropy data.

A1.3 Static Light Scattering

A homebuilt static laser light scattering instrument is used to monitor macroscopic protein aggregate formation. The apparatus consists of a fiber coupled CW laser ($\lambda_{\text{ex}} = 450 \text{ nm}$, CrystaLaser) as the excitation source and a photodiode as the detector at a 90° geometry. Scattering intensities (mV) were recorded using a

data recorder (PicoScope 2205 oscilloscope) and averaged over a 30-s period while stirring at ambient temperature. Sample intensities are normalized to a standard scattering sample (polystyrene beads) as well to laser power as measured by a reference photodiode. A schematic of the instrumental set up is provided in [Figure A1.5](#).

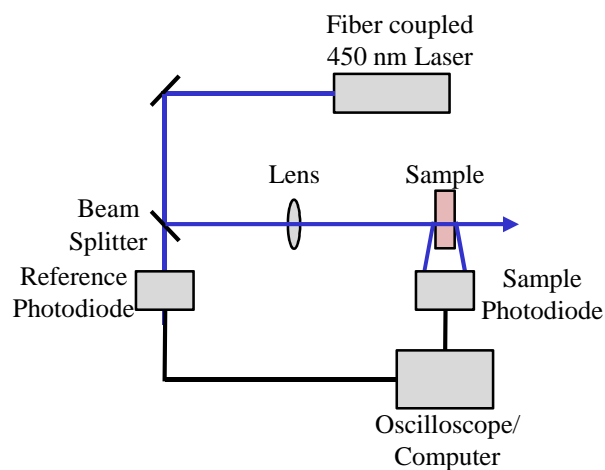


Figure A1.5: Schematic representation of the static light scattering instrument used to monitor macroscopic protein aggregation.

Appendix 2: Preparation and Characterization of Membrane Mimics

A2.1 Preparation of POPA:POPC Liposomes

Stock solutions of 16:0-18:1 PC and PA (25 mg/mL) dissolved in chloroform were purchased from Avanti Polar Lipids (see [Figure A2.1](#) for structure of lipids). Molar mixtures (1:1) of POPA:POPC were prepared gravimetrically by combining the proper amount of POPA and POPC in a glass vial.* Individual lipid aliquots (0.640 g; 0.432 mL) in glass vials (outer diameter \times height; 23 \times 85 mm) were then prepared and used immediately or purged with argon, sealed, parafilm, and stored at -20 °C for later use.

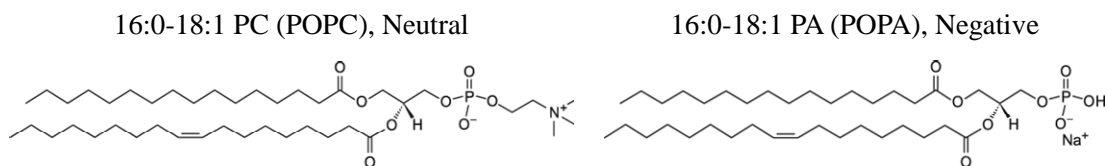


Figure A2.1: Structure of POPC and POPA lipids.

For preparation of unilamellar liposomes, lipids in chloroform were dehydrated under a nitrogen stream. Vials were first sealed with a rubber septum containing two needles, one connected to a nitrogen line and one for venting. As nitrogen is introduced to the lipid solution, the vial must be continuously rotated until

* Molecular weight of POPA and POPC is 696.9 and 760.1, respectively. In determination of the amount of POPA and POPC for a 1:1 molar mixture, all gravimetric measurements must take into account that lipids are dissolved in chloroform (density = 1.48 g/cm³ at 20 °C). Lipids dissolved in chloroform should not come in contact with plastic. Glass micropipettes and vials are always used for gravimetric measurements and lipid storage, respectively.

a uniform lipid film forms on the bottom of the vial. After 20 min under the argon stream, complete removal of the organic solvent is ensured by vacuum desiccation for 45 min. Dried lipids are rehydrated with 2.185 mL of desired buffer (5 mg/mL lipid) and re-suspended using a water bath sonicator (<10 min). Probe sonication is then performed using a Branson 450 Sonifier equipped with a micro-tip (45 min, duty cycle 50%, micro-tip limit).^{*} After sonication, vesicles are diluted to 2.5 mg/mL with 2.185 mL buffer. Liposomes are equilibrated overnight in a water bath above the transition temperature of the lipid mixture (−2 °C and 28 °C for POPC and POPA respectively). Before use, liposomes are centrifuged (10 min, 10,000 × *g*) to ensure removal of any titanium dust resulting from probe sonication.

A2.2 Characterization of 1:1 POPA:POPC Liposomes

Liposome concentration and size was confirmed using the Bartlett concentration assay, and transmission electron microscopy (TEM) and dynamic light scattering (DLS), respectively. In the Bartlett assay, phospholipids are converted to inorganic phosphate, phospho-molybdic acid, and then to 4-amino-2-naphthyl-4-sulfonic acid which can be colormetrically assayed and correlated to the original phospholipid content.¹⁵⁸ Using this assay, it was determined that no significant loss of lipids occurred as a result of probe sonication and subsequent centrifugation. Using TEM and DLS, the size distribution of liposome vesicles was evaluated. An example TEM image of POPA:POPC lipid vesicles is provided in [Figure A2.2](#). It

^{*}The microtip probe should be thoroughly cleaned with soap, rinsed with deionized water, and completely dry before use. The micro-tip should be centered in the center of the vial and in the middle of the lipid solution (not touching any part of the vial). The top of the vial should be covered with aluminum foil to prevent any spilling of the lipid solution during sonication. The liposome vial should be placed in a warm water bath during sonication.

was confirmed that the vesicles were unilamellar (TEM) and had average hydrodynamic radii of ~100 nm in diameter (DLS).

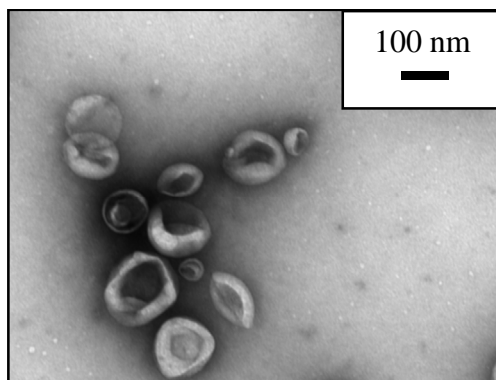


Figure A2.2: Characterization of 1:1 POPA:POPC lipid vesicles by TEM.

A2.3 Preparation of Purified Synaptic Vesicles

Steady-state and time-resolved fluorescence experiments were also conducted using purified mouse synaptic vesicles as model membranes. Synaptic vesicles were harvested from mouse brains and purified (synaptic vesicles isolation kit; Sigma Aldrich). Briefly, freshly dissected whole mice brains were weighed and placed in Hank's balanced salt solution buffer (HBSS) for immediate use. Brains were then subjected to a series of homogenization and centrifugation steps to achieve a crude vesicle preparation. To further enrich the synaptic vesicles, ultracentrifugation was performed in the presence of a density gradient medium (OptiPrep density gradient medium, Sigma Aldrich). A flow chart summarizing the purification protocol is provided in [Figure A2.3](#). For all experiments, the enriched synaptic vesicles were used. Synaptic vesicles were exchanged into appropriate buffer using PD10 columns (GE Healthcare).

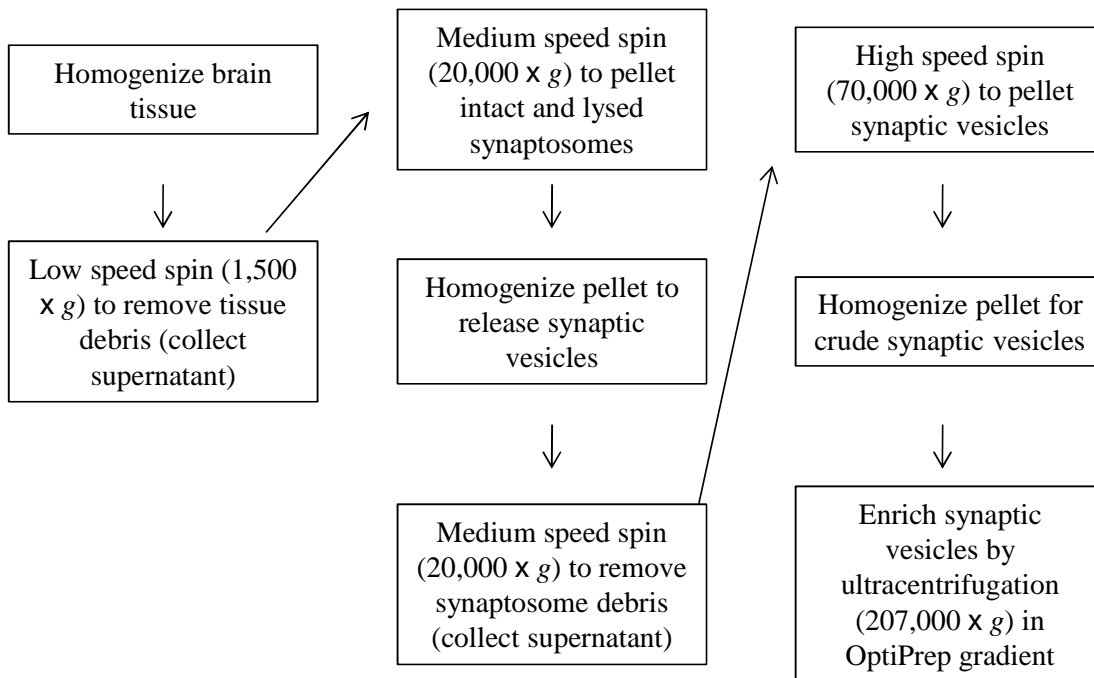


Figure A2.3: Flow chart for synaptic vesicles purification.*

A2.4 Characterization of Purified Synaptic Vesicles

To confirm the presence of and to characterize properties of purified synaptic vesicles, an immunoblotting assay and TEM was performed, respectively. Synaptic vesicles, unlike other cellular membranes, contain the membrane protein synaptophysin. Therefore the detection of synaptophysin is an indicator of synaptic vesicles. [Figure A2.4](#) shows a SDS-PAGE gel and subsequent western blot for synaptophysin of the purified synaptic vesicle fraction along with several fractions from purification steps. It is clear that synaptophysin is present in the enriched synaptic vesicle fraction used for experiments.

*Flow chart modified from the synaptic vesicle isolation kit technical bulletin (catalog number SV0100, Sigma Aldrich).

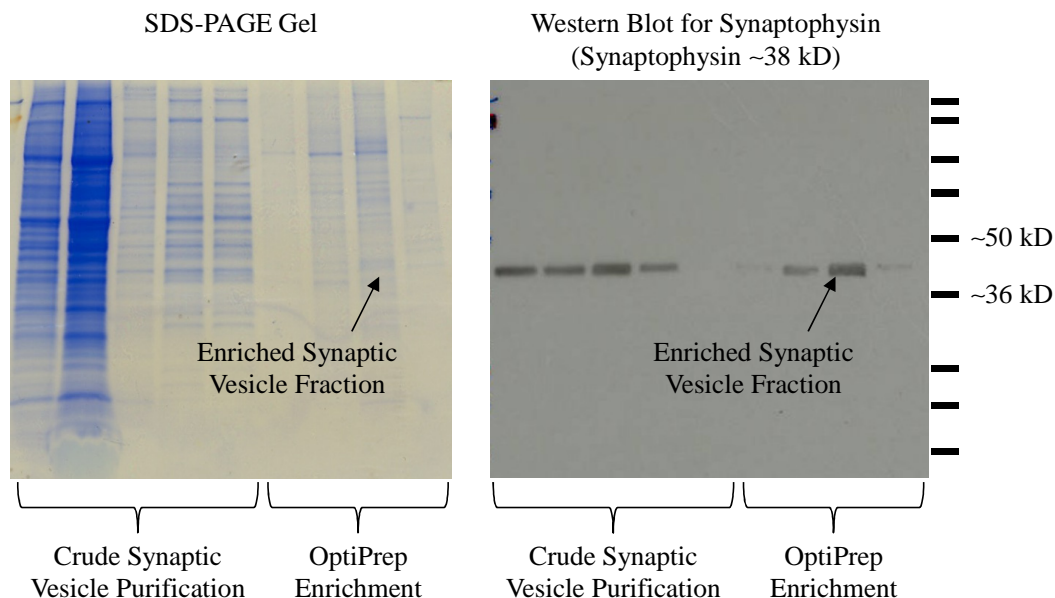


Figure A2.4: Confirmation of synaptic vesicle presence. Image of coomassie stained SDS-PAGE gel (left) and corresponding western blot for synaptophysin (right) used to confirm the presence of synaptic vesicles in various fractions during purification and enrichment. Lanes corresponding to crude purification and OptiPrep enrichment of synaptic vesicles are denoted for reference.

To characterize the size and homogeneity of the vesicles, purified synaptic vesicles were visualized with TEM. As seen in the TEM image in [Figure A2.5](#), vesicles are highly homogeneous and are approximately 50 – 75 nm in diameter. It is also apparent from the TEM image that several peripheral membrane proteins decorate the vesicles.

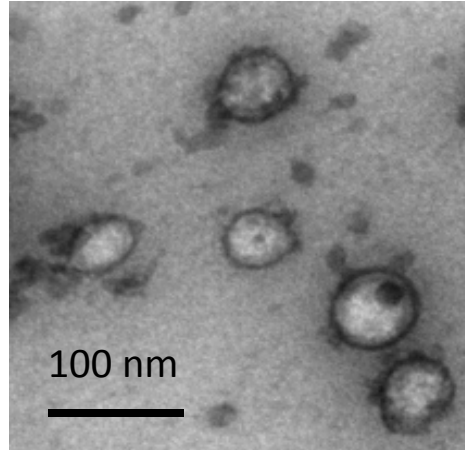


Figure A2.5: TEM visualization of synaptic vesicles. TEM image of negatively stained (0.5% uranyl acetate) mouse synaptic vesicles.

Appendix 3: Preparation and Characterization of Dye Labeled α -Synuclein*

A3.1 Incorporation of Single Cysteine Mutations into α -Synuclein

Site-directed mutagenesis to incorporate single cysteine residues at desired extrinsic fluorophore labeling sites in α -syn was accomplished by using the appropriate primers and template plasmid and a quick-change site-directed mutagenesis kit (Stratagene). Appropriate forward and reverse primers were designed such that at least 12 wild-type bases (coding 4 amino acids) flank the desired cysteine mutation site. For example, the primers used generate α -syn protein containing a G93C mutation are provided in [Figure A3.1](#). Wild-type human α -syn (pRK 172) was used as the template plasmid.⁸⁴

α -Synuclein Amino Acid Sequence	A	A	A	T	<u>C</u>	F	V	K	K		
Forward Primer	5'	GCA	GCA	GCC	ACT	<u>TGC</u>	TTT	GTC	AAA	AAG	3'
Reverse Primer	3'	GCA	GCA	GCC	ACT	<u>TGC</u>	TTT	GTC	AAA	AAG	5'

Figure A3.1: Primer design for G93C α -synuclein.

Components of polymerase chain reaction (PCR) mixtures are listed below in order of addition; all reagents were kept on ice prior to mixing.

H₂O to a volume of 20 μ L
2 μ L 10x buffer
25 – 50 ng wild-type α -syn plasmid

*Single extrinsic 1,5-IAEDANS or IANBD fluorophore labeled α -synucleins were used in fluorescence energy transfer, synaptic vesicle, and α -syn aggregation experiments. Results regarding α -syn aggregation experiments are reported in the following publication: Yap, T.L., Pfefferkorn, C. M., Lee J.C., Residue-specific fluorescent probes of α -synuclein: Detection of early events at the N- and C-termini during fibril assembly. *Biochemistry* **2011**, 50(12), 1963-1965.

50 ng	Forward primer
50 ng	Reverse primer
0.4 μ L	5 mM deoxyribonucleotide triphosphate (dNTP)
0.4 μ L	<i>PfuTurbo</i> (polymerase)

PCR mixtures were then subjected to thermal cycling as outlined below:

Step 1	95 °C	4 min
Step 2 (18 cycles)	94 °C	1 min
	55 °C	1 min 30 seconds
	72 °C	7 min
Step 3	72 °C	10 min

This procedure facilitates the denaturation of the template plasmid, the annealing of mutagenic primers, and the extension of primers to form double stranded DNA in which one strand contains the mutated sequence. Nicks in the mutated strand are sealed by components in the *PfuTurbo* enzyme blend. After thermal cycling, any remaining wild-type template plasmid is digested by adding the restriction endonuclease *DpnI* (1 μ L; 20 U/ μ L) to the reaction mixtures and incubating (1 h, 37 °C and 20 min, 80 °C).

For purification, PCR DNA products were transformed into XL1-Blue competent cells, grown in Luria Broth (LB) media containing Ampicillin (AMP) (100 μ g/ μ L), and treated using the QIAprep Miniprep Kit (Qiagen). Briefly, for transformation, DNA (1 μ l) was added to gently thawed XL1-blue cells (50 μ L) in pre-chilled PCR tubes and incubated on ice for 5 min followed by a heat shock (45 s, 42 °C). Growth medium (200 μ L LB) was then added to the DNA/cell mixture, incubated (1 h, 37 °C), and spread onto LB agar plates containing AMP (100 μ g/mL). After incubation (overnight, 37 °C), single colonies were added to 5 mL of growth media (LB containing 100 μ g/ μ L AMP) and incubated (shaking overnight, 37 °C).

Cultures were centrifuged and cell pellets treated according to protocols found in the QIAprep Miniprep Kit. Purified DNA concentration was measured using absorption spectroscopy ($OD_{260nm} = 1 = 50 \mu\text{g}/\mu\text{L}$). Mutations were verified by DNA sequencing (Macrogen, USA).

A3.2 Dye Labeling and Purification of Single Cysteine Containing α -Synucleins

Single cysteine containing proteins were expressed^{84,159} and purified¹⁰² as previously reported with minor modifications. To prevent disulfide bond formation, all lysis and purification buffers contained 0.5 mM dithiothreitol (DTT). Protein purity was assessed by SDS-PAGE on a Pharmacia Phastsystem (GE Healthcare) and visualized by silver staining methods. All purified proteins were concentrated using Amicon YM-3 (MWCO 3kD, Millipore) and stored at $-80 \text{ }^\circ\text{C}$.

Labeling of purified single cysteine containing α -syn with 1,5-IAEDANS, 5-(((2-iodoacetyl)amino)ethyl)amino)naphthalene-1-sulfonic acid (1,5-IAEDANS) or N,N'-dimethyl-N-(iodoacetyl)-N'-(7-nitrobenz-2-oxa-1,3-diazol-4-yl)ethylenediamine (IANBD) (Figure A3.2) is accomplished by forming a thioether bond to the thiol group of the cysteine. First, tris(2-carboxyethyl)phosphine, TCEP (70 μl of 100 mM), is added to purified protein (14 mL of 50 μM protein in 100 mM NaPi, pH 7.4) and incubated (1 h) to ensure complete reduction of any disulfide bonds. Dye is then added dropwise to the reaction mixture (1.5 mL of 5 mM dye prepared in dimethylsulfoxide (DMSO)) and incubated (2 h). The labeling reaction is stopped by the addition of DTT (1 mM). All reactions were performed in a three neck flask under nitrogen flow while stirring and protected from light.

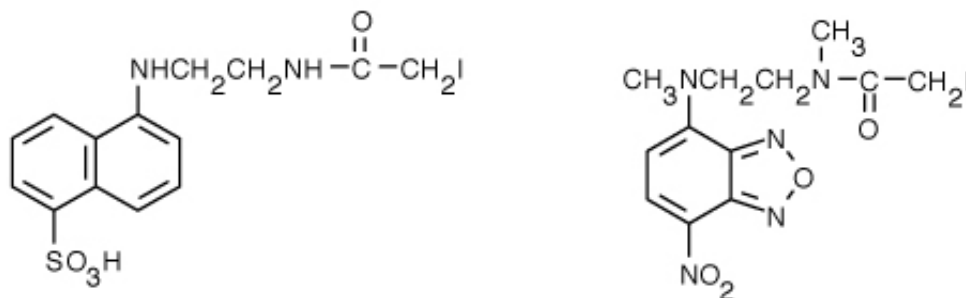


Figure A3.2: Structure of 1,5-IAEDANS (left) and IANBD amide (right).

The dye labeled proteins were then exchanged into the appropriate buffer (20 mM Tris, pH 8.0) and separated from excess dye using a desalting column (HiPrep Desalting 26/10, GE Healthcare). The singly-labeled α -syn was then purified by anionic exchange chromatography using a linear gradient from 100 – 300 mM NaCl in 20 mM Tris buffer (MonoQ column, GE Healthcare). An example chromatogram from purification of G7C 1,5-IAEDANS labeled α -syn is provided in [Figure A3.3](#). Peaks corresponding to single, double, and unlabeled protein can be identified based on absorbance. Unlabeled protein elutes with primarily 280 nm absorbance, while single and double dye labeled α -synucleins exhibit sizable absorbance at other wavelengths (1,5-IAEDANS: $\epsilon_{336\text{nm}} = 5700 \text{ M}^{-1}\text{cm}^{-1}$; IANBD: $\epsilon_{478\text{nm}} = 25,000 \text{ M}^{-1}\text{cm}^{-1}$). Purified α -syn fractions are concentrated using Amicon YM-3 (MWCO 3kD, Millipore). Concentrated and purified singly labeled 1,5-IAEDANS α -syn will exhibit a absorbance ratio ($\text{OD}_{336 \text{ nm}}/\text{OD}_{280 \text{ nm}}$) of approximately 0.8 – 0.9 whereas IANBD α -syn will exhibit a absorbance ratio ($\text{OD}_{478 \text{ nm}}/\text{OD}_{280 \text{ nm}}$) of approximately 0.4 – 0.6. Protein purity is assessed by SDS-PAGE on a Pharmacia Phastsystem (GE Healthcare) and visualized by silver staining methods. An example protein gel showing purified singly labeled 1,5-IAEDANS G7C α -syn fractions is provided in

Figure A3.4. ESI-MS was also used to confirm the mass of all the dye-labeled proteins.

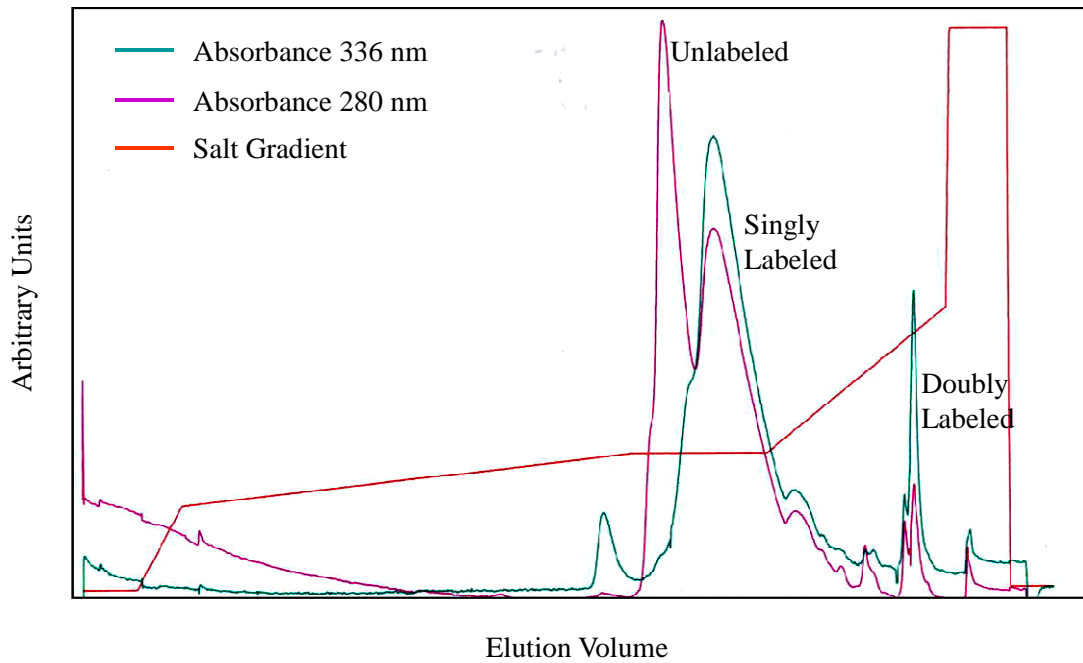


Figure A3.3: Anionic-exchange chromatogram from purification of 1,5-IAEDANS labeled G7C α -synuclein. Presence of protein and 1,5-IAEDANS are identified by absorbance peaks at 280 nm (purple) and 336 nm (green) respectively. The salt gradient is indicated in red.

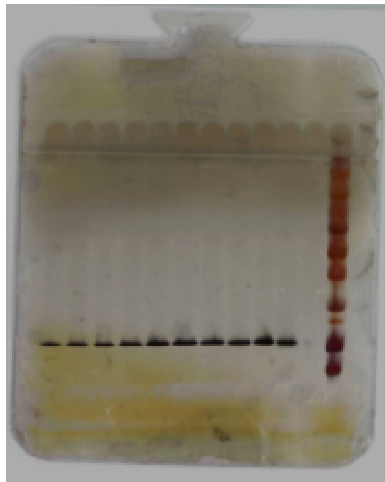


Figure A3.4: Silver stained SDS-PAGE gel used to confirm the purity of singly labeled 1, 5-IAEDANS α -synuclein fractions.

Bibliography

- (1) Cohen, A. S.; Calkins, E. *Nature* **1959**, *183*, 1202.
- (2) Vassar, P. S.; Culling, C. F. A. *Arch. Pathol.* **1959**, *68*, 487.
- (3) Divry, P.; Florkin, M. *C. R. Seances Soc. Biol. Ses Fil.* **1927**, *97*, 1808.
- (4) Eanes, E. D.; Glenner, G. G. *J. Histochem. Cytochem.* **1968**, *16*, 673.
- (5) Tycko, R. *Curr. Opin. Struct. Biol.* **2004**, *14*, 96.
- (6) Shewmaker, F.; McGlinchey, R. P.; Wickner, R. B. *J. Biol. Chem.* **2011**, *286*, 16533.
- (7) Bhak, G.; Choe, Y. J.; Paik, S. R. *BMB Rep.* **2009**, *42*, 541.
- (8) Chiti, F.; Dobson, C. M. *Annu. Rev. Biochem.* **2006**, *75*, 333.
- (9) Hammer, N. D.; Wang, X.; McGuffie, B. A.; Chapman, M. R. *J. Alzheimer's Dis.* **2008**, *13*, 407.
- (10) Fowler, D. M.; Koulov, A. V.; Balch, W. E.; Kelly, J. W. *Trends Biochem. Sci.* **2007**, *32*, 217.
- (11) Jahn, T. R.; Radford, S. E. *Arch. Biochem. Biophys.* **2008**, *469*, 100.
- (12) Maji, S. K.; Perrin, M. H.; Sawaya, M. R.; Jessberger, S.; Vadodaria, K.; Rissman, R. A.; Singru, P. S.; Nilsson, K. P. R.; Simon, R.; Schubert, D.; Eisenberg, D.; Rivier, J.; Sawchenko, P.; Vale, W.; Riek, R. *Science* **2009**, *325*, 328.
- (13) Raposo, G.; Marks, M. S. *Nat. Rev. Mol. Cell Biol.* **2007**, *8*, 786.
- (14) Roychaudhuri, R.; Yang, M.; Hoshi, M. M.; Teplow, D. B. *J. Biol. Chem.* **2009**, *284*, 4749.
- (15) Abedini, A.; Raleigh, D. P. *Phys. Biol.* **2009**, *6*.
- (16) White, S. H.; Wimley, W. C. *Biochim. Biophys. Acta, Rev. Biomembr.* **1998**, *1376*, 339.
- (17) Aisenbrey, C.; Borowik, T.; Bystrom, R.; Bokvist, M.; Lindstrom, F.; Misiak, H.; Sani, M. A.; Grobner, G. *Eur. Biophys. J.* **2008**, *37*, 247.

- (18) Murray, D.; Arbuzova, A.; Honig, B.; McLaughlin, S. *Curr. Top. Membr.* **2002**, *52*, 277.
- (19) McLaughlin, A.; Grathwohl, C.; McLaughlin, S. *Biochim. Biophys. Acta* **1978**, *513*, 338.
- (20) Jacobson, K.; Ishihara, A.; Inman, R. *Annu. Rev. Physiol.* **1987**, *49*, 163.
- (21) Ramadurai, S.; Holt, A.; Krasnikov, V.; van den Bogaart, G.; Killian, J. A.; Poolman, B. *J. Am. Chem. Soc.* **2009**, *131*, 12650.
- (22) Kirkitadze, M. D.; Condron, M. M.; Teplow, D. B. *J. Mol. Biol.* **2001**, *312*, 1103.
- (23) Teplow, D. B.; Lazo, N. D.; Bitan, G.; Bernstein, S.; Wyttenbach, T.; Bowers, M. T.; Baumketner, A.; Shea, J.-E.; Urbanc, B.; Cruz, L.; Borreguero, J.; Stanley, H. E. *Acc. Chem. Res.* **2006**, *39*, 635.
- (24) Anderson, V. L.; Ramlall, T. F.; Rospigliosi, C. C.; Webb, W. W.; Eliezer, D. *Proc. Natl. Acad. Sci. U. S. A.* **2010**, *107*, 18850.
- (25) Goldsbury, C.; Goldie, K.; Pellaud, J.; Seelig, J.; Frey, P.; Muller, S. A.; Kistler, J.; Cooper, G. J. S.; Aebi, U. *J. Struct. Biol.* **2000**, *130*, 352.
- (26) Kunjithapatham, R.; Oliva, F. Y.; Doshi, U.; Perez, M.; Avila, J.; Munoz, V. *Biochemistry* **2005**, *44*, 149.
- (27) Olofsson, A.; Borowik, T.; Grobner, G.; Sauer-Eriksson, A. E. *J. Mol. Biol.* **2007**, *374*, 186.
- (28) White, S. H. *Protein Sci.* **2004**, *13*, 1948.
- (29) Opella, S. J.; Marassi, F. M. *Chem. Rev.* **2004**, *104*, 3587.
- (30) Wang, G. S. *Curr. Protein Pept. Sci.* **2008**, *9*, 50.
- (31) Raunser, S.; Walz, T. *Ann. Rev. Biophys.* **2009**, *38*, 89.
- (32) Werten, P. J. L.; Remigy, H. W.; de Groot, B. L.; Fotiadis, D.; Philippsen, A.; Stahlberg, H.; Grubmuller, H.; Engel, A. *FEBS Lett.* **2002**, *529*, 65.
- (33) Greenfield, N. J. *Nat. Protoc.* **2006**, *1*, 2876.
- (34) Sreerama, N.; Woody, R. W. *Methods Enzymol.* **2004**, *383*, 318.
- (35) Byler, D. M.; Susi, H. *Biopolymers* **1986**, *25*, 469.

- (36) Kong, J.; Yu, S. *Acta Biochim. Biophys. Sin.* **2007**, *39*, 549.
- (37) Shafaat, H. S.; Sanchez, K. M.; Neary, T. J.; Kim, J. E. *J. Raman Spectrosc.* **2009**, *40*, 1060.
- (38) Sanchez, K. M.; Kang, G. P.; Wu, B. J.; Kim, J. E. *Biophys. J.* **2011**, *100*, 2121.
- (39) Bodner, C.; Dobson, C.; Bax, A. *J. Mol. Biol.* **2009**, *390*, 775.
- (40) Beyer, K. *Cell Biochem. Biophys.* **2007**, *47*, 285.
- (41) Watts, A.; Straus, S. K.; Grage, S. L.; Kamihira, M.; Lam, Y. H.; Zhao, X. *Methods Mol Biol* **2004**, *278*, 403.
- (42) Tycko, R. *Methods Enzymol.* **2001**, *339*, 390.
- (43) Beechem, J. M.; Haas, E. *Biophys. J.* **1989**, *55*, 1225.
- (44) Eftink, M. R. *Methods Biochem. Anal.* **1991**, *35*, 127.
- (45) Förster, T. *Ann. Phys.* **1948**, *437*, 55.
- (46) Wu, P. G.; Brand, L. *Anal. Biochem.* **1994**, *218*, 1.
- (47) Lee, J. C.; Langen, R.; Hummel, P. A.; Gray, H. B.; Winkler, J. R. *Proc. Natl. Acad. Sci. U. S. A.* **2004**, *101*, 16466.
- (48) Ferreon, A. C. M.; Gambin, Y.; Lemke, E. A.; Deniz, A. A. *Proc. Natl. Acad. Sci. U. S. A.* **2009**, *106*, 5645.
- (49) Reginsson, G. W.; Schiemann, O. *Biochem. J.* **2011**, *434*, 353.
- (50) Kim, J. E.; Arjara, G.; Richards, J. H.; Gray, H. B.; Winkler, J. R. *J. Phys. Chem. B* **2006**, *110*, 17656.
- (51) Kleinschmidt, J. H.; den Blaauwen, T.; Driessen, A. J. M.; Tamm, L. K. *Biochemistry* **1999**, *38*, 5006.
- (52) Callis, P. R.; Liu, T. Q. *J. Phys. Chem. B* **2004**, *108*, 4248.
- (53) Bolen, E. J.; Holloway, P. W. *Biochemistry* **1990**, *29*, 9638.
- (54) Kleinschmidt, J. H.; Tamm, L. K. *Biochemistry* **1999**, *38*, 4996.

- (55) London, E.; Feigenson, G. W. *Biochemistry* **1981**, *20*, 1932.
- (56) Markello, T.; Zlotnick, A.; Everett, J.; Tennyson, J.; Holloway, P. W. *Biochemistry* **1985**, *24*, 2895.
- (57) Caputo, G. A.; London, E. *Biochemistry* **2003**, *42*, 3265.
- (58) Hubbell, W. L.; Gross, A.; Langen, R.; Lietzow, M. A. *Curr. Opin. Struct. Biol.* **1998**, *8*, 649.
- (59) Lakowicz, J. R. *Principles of Fluorescence Spectroscopy*; 3rd ed.; Springer: New York, 2006.
- (60) Krepiy, D.; Mihailescu, M.; Freitas, J. A.; Schow, E. V.; Worcester, D. L.; Gawrisch, K.; Tobias, D. J.; White, S. H.; Swartz, K. J. *Nature* **2009**, *462*, 473.
- (61) McGillivray, D. J.; Valincius, G.; Heinrich, F.; Robertson, J. W. F.; Vanderah, D. J.; Febo-Ayala, W.; Ignatjev, I.; Losche, M.; Kasianowicz, J. J. *Biophys. J.* **2009**, *96*, 1547.
- (62) Valincius, G.; Heinrich, F.; Budvytyte, R.; Vanderah, D. J.; McGillivray, D. J.; Sokolov, Y.; Hall, J. E.; Losche, M. *Biophys. J.* **2008**, *95*, 4845.
- (63) Lakey, J. H. *J. R. Soc., Interface* **2009**, *6*, S567.
- (64) McGillivray, D. J.; Valincius, G.; Vanderah, D. J.; Febo-Ayala, W.; Woodward, J. T.; Heinrich, F.; Kasianowicz, J. J.; Losche, M. *Biointerphases* **2007**, *2*, 21.
- (65) Lees, A.; Hardy, J.; Revesz, T. *Lancet* **2009**, *373*, 2055.
- (66) Weinreb, P. H.; Zhen, W. G.; Poon, A. W.; Conway, K. A.; Lansbury, P. T. *Biochemistry* **1996**, *35*, 13709.
- (67) Conway, K. A.; Lee, S. J.; Rochet, J. C.; Ding, T. T.; Williamson, R. E.; Lansbury, P. T. *Proc. Natl. Acad. Sci. U. S. A.* **2000**, *97*, 571.
- (68) Ding, T. T.; Lee, S. J.; Rochet, J. C.; Lansbury, P. T. *Biochemistry* **2002**, *41*, 10209.
- (69) Uversky, V. N.; Li, J.; Fink, A. L. *J. Biol. Chem.* **2001**, *276*, 10737.
- (70) Hong, D. P.; Fink, A. L.; Uversky, V. N. *J. Mol. Biol.* **2008**, *383*, 214.
- (71) Dauer, W.; Przedborski, S. *Neuron* **2003**, *39*, 889.

- (72) Singleton, A. B.; Farrer, M.; Johnson, J.; Singleton, A.; Hague, S.; Kachergus, J.; Hulihan, M.; Peuralinna, T.; Dutra, A.; Nussbaum, R.; Lincoln, S.; Crawley, A.; Hanson, M.; Maraganore, D.; Adler, C.; Cookson, M. R.; Muentner, M.; Baptista, M.; Miller, D.; Blancato, J.; Hardy, J.; Gwinn-Hardy, K. *Science* **2003**, *302*, 841.
- (73) Chartier-Harlin, M. C.; Kachergus, J.; Roumier, C.; Mouroux, V.; Douay, X.; Lincoln, S.; Levecque, C.; Larvor, L.; Andrieux, J.; Hulihan, M.; Waucquier, N.; Defebvre, L.; Amouyel, P.; Farrer, M.; Destee, A. *Lancet* **2004**, *364*, 1167.
- (74) Kruger, R.; Kuhn, W.; Muller, T.; Woitalla, D.; Graeber, M.; Kosel, S.; Przuntek, H.; Epplen, J. T.; Schols, L.; Riess, O. *Nat. Genet.* **1998**, *18*, 106.
- (75) Polymeropoulos, M. H.; Lavedan, C.; Leroy, E.; Ide, S. E.; Dehejia, A.; Dutra, A.; Pike, B.; Root, H.; Rubenstein, J.; Boyer, R.; Stenroos, E. S.; Chandrasekharappa, S.; Athanassiadou, A.; Papapetropoulos, T.; Johnson, W. G.; Lazzarini, A. M.; Duvoisin, R. C.; DiIorio, G.; Golbe, L. I.; Nussbaum, R. L. *Science* **1997**, *276*, 2045.
- (76) Zarranz, J. J.; Alegre, J.; Gomez-Esteban, J. C.; Lezcano, E.; Ros, R.; Ampuero, I.; Vidal, L.; Hoenicka, J.; Rodriguez, O.; Ates, B.; Llorens, V.; Tortosa, E. G.; del Ser, T.; Munoz, D. G.; de Yebenes, J. G. *Ann. Neurol.* **2004**, *55*, 164.
- (77) Chu, Y. P.; Kordower, J. H. *Neurobiol. Dis.* **2007**, *25*, 134.
- (78) Greten-Harrison, B.; Polydoro, M.; Morimoto-Tomita, M.; Diao, L.; Williams, A. M.; Nie, E. H.; Makani, S.; Tian, N.; Castillo, P. E.; Buchman, V. L.; Chandra, S. S. *Proc. Natl. Acad. Sci. U. S. A.* **2010**, *107*, 19573.
- (79) Maroteaux, L.; Campanelli, J. T.; Scheller, R. H. *J. Neurosci.* **1988**, *8*, 2804.
- (80) Nakajo, S.; Omata, K.; Aiuchi, T.; Shibayama, T.; Okahashi, I.; Ochiai, H.; Nakai, Y.; Nakaya, K.; Nakamura, Y. *J. Neurochem.* **1990**, *55*, 2031.
- (81) Nakajo, S.; Tsukada, K.; Omata, K.; Nakamura, Y.; Nakaya, K. *Eur. J. Biochem.* **1993**, *217*, 1057.
- (82) Ueda, K.; Fukushima, H.; Masliah, E.; Xia, Y.; Iwai, A.; Yoshimoto, M.; Otero, D. A. C.; Kondo, J.; Ihara, Y.; Saitoh, T. *Proc. Natl. Acad. Sci. U. S. A.* **1993**, *90*, 11282.
- (83) George, J. M.; Jin, H.; Woods, W. S.; Clayton, D. F. *Neuron* **1995**, *15*, 361.
- (84) Jakes, R.; Spillantini, M. G.; Goedert, M. *FEBS Lett.* **1994**, *345*, 27.

- (85) Ji, H. J.; Liu, Y. L. E.; Jia, T. L.; Wang, M. S.; Liu, J. W.; Xiao, G. W.; Joseph, B. K.; Rosen, C.; Shi, Y. E. *Cancer Res.* **1997**, *57*, 759.
- (86) George, J. M. *Genome Biol.* **2002**, *3*, 6.
- (87) Clayton, D. F.; George, J. M. *J. Neurosci. Res.* **1999**, *58*, 120.
- (88) Abeliovich, A.; Schmitz, Y.; Farinas, I.; Choi-Lundberg, D.; Ho, W. H.; Castillo, P. E.; Shinsky, N.; Verdugo, J. M. G.; Armanini, M.; Ryan, A.; Hynes, M.; Phillips, H.; Sulzer, D.; Rosenthal, A. *Neuron* **2000**, *25*, 239.
- (89) Al-Wandi, A.; Ninkina, N.; Millership, S.; Williamson, S. J. M.; Jones, P. A.; Buchman, V. L. *Neurobiol. Aging* **2010**, *31*, 796.
- (90) Cabin, D. E.; Shimazu, K.; Murphy, D.; Cole, N. B.; Gottschalk, W.; McIlwain, K. L.; Orrison, B.; Chen, A.; Ellis, C. E.; Paylor, R.; Lu, B.; Nussbaum, R. L. *J. Neurosci.* **2002**, *22*, 8797.
- (91) Yavich, L.; Tanila, H.; Vepsalainen, S.; Jakala, P. *J. Neurosci.* **2004**, *24*, 11165.
- (92) Larsen, K. E.; Schmitz, Y.; Troyer, M. D.; Mosharov, E.; Dietrich, P.; Quazi, A. Z.; Savalle, M.; Nemani, V.; Chaudhry, F. A.; Edwards, R. H.; Stefanis, L.; Sulzer, D. *J. Neurosci.* **2006**, *26*, 11915.
- (93) Nemani, V. M.; Lu, W.; Berge, V.; Nakamura, K.; Onoa, B.; Lee, M. K.; Chaudhry, F. A.; Nicoll, R. A.; Edwards, R. H. *Neuron* **2010**, *65*, 66.
- (94) Burre, J.; Sharma, M.; Tsetsenis, T.; Buchman, V.; Etherton, M. R.; Sudhof, T. C. *Science* **2010**, *329*, 1663.
- (95) Vila, M.; Ramonet, D.; Perier, C. *J. Neurochem.* **2008**, *107*, 317.
- (96) Cole, N. B.; DiEuliis, D.; Leo, P.; Mitchell, D. C.; Nussbaum, R. L. *Exp. Cell Res.* **2008**, *314*, 2076.
- (97) Nakamura, K.; Nemani, V. M.; Wallender, E. K.; Kaehlcke, K.; Ott, M.; Edwards, R. H. *J. Neurosci.* **2008**, *28*, 12305.
- (98) Mishra, V. K.; Palgunachari, M. N. *Biochemistry* **1996**, *35*, 11210.
- (99) Clayton, D. F.; George, J. M. *Trends Neurosci.* **1998**, *21*, 249.
- (100) Segrest, J. P.; Jackson, R. L.; Morriset, J. D.; Gotto, A. M. *FEBS Lett.* **1974**, *38*, 247.

- (101) El-Agnaf, O. M. A.; Bodles, A. M.; Guthrie, D. J. S.; Harriott, P.; Irvine, G. B. *Eur. J. Biochem.* **1998**, *258*, 157.
- (102) Pfefferkorn, C. M.; Lee, J. C. *J. Phys. Chem. B* **2010**, *114*, 4615.
- (103) Tamamizu-Kato, S.; Kosaraju, M. G.; Kato, H.; Raussens, V.; Ruyschaert, J. M.; Narayanaswami, V. *Biochemistry* **2006**, *45*, 10947.
- (104) Chen, M.; Margittai, M.; Chen, J.; Langen, R. *J. Biol. Chem.* **2007**, *282*, 24970.
- (105) Heise, H.; Hoyer, W.; Becker, S.; Andronesi, O. C.; Riedel, D.; Baldus, M. *Proc. Natl. Acad. Sci. U. S. A.* **2005**, *102*, 15871.
- (106) Qin, Z.; Hu, D.; Han, S.; Hong, D. P.; Fink, A. L. *Biochemistry* **2007**, *46*, 13322.
- (107) Vilar, M.; Chou, H. T.; Luhrs, T.; Maji, S. K.; Riek-Loher, D.; Verel, R.; Manning, G.; Stahlberg, H.; Riek, R. *Proc. Natl. Acad. Sci. U. S. A.* **2008**, *105*, 8637.
- (108) Bisaglia, M.; Mammi, S.; Bubacco, L. *FASEB J.* **2009**, *23*, 329.
- (109) Bussell, R.; Eliezer, D. *Biochemistry* **2004**, *43*, 4810.
- (110) Choi, W.; Zibae, S.; Jakes, R.; Serpell, L. C.; Davletov, B.; Crowther, R. A.; Goedert, M. *FEBS Lett.* **2004**, *576*, 363.
- (111) Jensen, P. H.; Nielsen, M. S.; Jakes, R.; Dotti, G.; Goedert, M. *J. Biol. Chem.* **1998**, *273*, 26292.
- (112) Jo, E.; Fuller, N.; Rand, R. P.; St George-Hyslop, P.; Fraser, P. E. *J. Mol. Biol.* **2002**, *315*, 799.
- (113) Nuscher, B.; Kamp, F.; Mehnert, T.; Odoy, S.; Haass, C.; Kahle, P. J.; Beyer, K. *J. Biol. Chem.* **2004**, *279*, 21966.
- (114) Perrin, R. J.; Woods, W. S.; Clayton, D. F.; George, J. M. *J. Biol. Chem.* **2000**, *275*, 34393.
- (115) Stockl, M.; Fischer, P.; Wanker, E.; Herrmann, A. *J. Mol. Biol.* **2008**, *375*, 1394.
- (116) Davidson, W. S.; Jonas, A.; Clayton, D. F.; George, J. M. *J. Biol. Chem.* **1998**, *273*, 9443.

- (117) Necula, M.; Chirita, C. N.; Kuret, J. *J. Biol. Chem.* **2003**, *278*, 46674.
- (118) Zhu, M.; Fink, A. L. *J. Biol. Chem.* **2003**, *278*, 16873.
- (119) Zhu, M.; Li, J.; Fink, A. L. *J. Biol. Chem.* **2003**, *278*, 40186.
- (120) Chatelier, R. C.; Minton, A. P. *Biophys. J.* **1996**, *71*, 2367.
- (121) Fantini, J.; Yahi, N. *Expert Rev. Mol. Med.* **2010**, *12*, 22.
- (122) Drescher, M.; van Rooijen, B. D.; Veldhuis, G.; Subramaniam, V.; Huber, M. *J. Am. Chem. Soc.* **2010**, *132*, 4080.
- (123) Lee, H. J.; Choi, C.; Lee, S. J. *J. Biol. Chem.* **2002**, *277*, 671.
- (124) Cole, N. B.; Murphy, D. D.; Grider, T.; Rueter, S.; Brasaemle, D.; Nussbaum, R. L. *J. Biol. Chem.* **2002**, *277*, 6344.
- (125) Kayed, R.; Sokolov, Y.; Edmonds, B.; McIntire, T. M.; Milton, S. C.; Hall, J. E.; Glabe, C. G. *J. Biol. Chem.* **2004**, *279*, 46363.
- (126) Lashuel, H. A.; Hartley, D.; Petre, B. M.; Walz, T.; Lansbury, P. T. *Nature* **2002**, *418*, 291.
- (127) Butterfield, S. M.; Lashuel, H. A. *Angew. Chem., Int. Ed.* **2010**, *49*, 5628.
- (128) Quist, A.; Doudevski, L.; Lin, H.; Azimova, R.; Ng, D.; Frangione, B.; Kagan, B.; Ghiso, J.; Lal, R. *Proc. Natl. Acad. Sci. U. S. A.* **2005**, *102*, 10427.
- (129) Volles, M. J.; Lee, S. J.; Rochet, J. C.; Shtilerman, M. D.; Ding, T. T.; Kessler, J. C.; Lansbury, P. T. *Biochemistry* **2001**, *40*, 7812.
- (130) Volles, M. J.; Lansbury, P. T. *Biochemistry* **2002**, *41*, 4595.
- (131) Zakharov, S. D.; Hulleman, J. D.; Dutseva, E. A.; Antonenko, Y. N.; Rochet, J. C.; Cramer, W. A. *Biochemistry* **2007**, *46*, 14369.
- (132) van Rooijen, B. D.; Claessens, M.; Subramaniam, V. *FEBS Lett.* **2008**, *582*, 3788.
- (133) van Rooijen, B. D.; Claessens, M.; Subramaniam, V. *Biochim. Biophys. Acta, Biomembr.* **2009**, *1788*, 1271.
- (134) van Rooijen, B. D.; Claessens, M.; Subramaniam, V. *PLoS One* **2010**, *5*, 14292.

- (135) Kim, H. Y.; Cho, M. K.; Kumar, A.; Maier, E.; Siebenhaar, C.; Becker, S.; Fernandez, C. O.; Lashuel, H. A.; Benz, R.; Lange, A.; Zweckstetter, M. *J. Am. Chem. Soc.* **2009**, *131*, 17482.
- (136) Giehm, L.; Svergun, D. I.; Otzen, D. E.; Vestergaard, B. *Proc. Natl. Acad. Sci. U. S. A.* **2011**, *108*, 3246.
- (137) Varkey, J.; Isas, J. M.; Mizuno, N.; Jensen, M. B.; Bhatia, V. K.; Jao, C. C.; Petrlova, J.; Voss, J. C.; Stamou, D. G.; Steven, A. C.; Langen, R. *J. Biol. Chem.* **2010**, *285*, 32486.
- (138) Pandey, A. P.; Haque, F.; Rochet, J.-C.; Hovis, J. S. *J. Phys. Chem. B* **2011**, *115*, 5886.
- (139) Bisaglia, M.; Tessari, I.; Pinato, L.; Bellanda, M.; Giraud, S.; Fasano, M.; Bergantino, E.; Bubacco, L.; Mammi, S. *Biochemistry* **2005**, *44*, 329.
- (140) Eliezer, D.; Kutluay, E.; Bussell, R.; Browne, G. *J. Mol. Biol.* **2001**, *307*, 1061.
- (141) Chandra, S.; Chen, X. C.; Rizo, J.; Jahn, R.; Sudhof, T. C. *J. Biol. Chem.* **2003**, *278*, 15313.
- (142) Ulmer, T. S.; Bax, A.; Cole, N. B.; Nussbaum, R. L. *J. Biol. Chem.* **2005**, *280*, 9595.
- (143) Drescher, M.; Veldhuis, G.; van Rooijen, B. D.; Milikisyants, S.; Subramaniam, V.; Huber, M. *J. Am. Chem. Soc.* **2008**, *130*, 7796.
- (144) Borbat, P.; Ramlall, T. F.; Freed, J. H.; Eliezer, D. *J. Am. Chem. Soc.* **2006**, *128*, 10004.
- (145) Bussell, R.; Eliezer, D. *J. Mol. Biol.* **2003**, *329*, 763.
- (146) Georgieva, E. R.; Ramlall, T. F.; Borbat, P. P.; Freed, J. H.; Eliezer, D. *J. Am. Chem. Soc.* **2008**, *130*, 12856.
- (147) Jao, C. C.; Der-Sarkissian, A.; Chen, J.; Langen, R. *Proc. Natl. Acad. Sci. U. S. A.* **2004**, *101*, 8331.
- (148) Jao, C. C.; Hegde, B. G.; Chen, J.; Haworth, I. S.; Langen, R. *Proc. Natl. Acad. Sci. U. S. A.* **2008**, *105*, 19666.
- (149) Trexler, A. J.; Rhoades, E. *Biochemistry* **2009**, *48*, 2304.

- (150) Winkler, G. R.; Harkins, S. B.; Lee, J. C.; Gray, H. B. *J. Phys. Chem. B* **2006**, *110*, 7058.
- (151) Lee, J. C.; Gray, H. B.; Winkler, J. R. *J. Am. Chem. Soc.* **2005**, *127*, 16388.
- (152) Lee, J. C.; Lai, B. T.; Kozak, J. J.; Gray, H. B.; Winkler, J. R. *J. Phys. Chem. B* **2007**, *111*, 2107.
- (153) Beechem, J. M.; Brand, L. *Annu. Rev. Biochem.* **1985**, *54*, 43.
- (154) Chen, Y.; Barkley, M. D. *Biochemistry* **1998**, *37*, 9976.
- (155) Clayton, A. H. A.; Sawyer, W. H. *Eur. Biophys. J.* **2002**, *31*, 9.
- (156) Ladokhin, A. S.; Jayasinghe, S.; White, S. H. *Anal. Biochem.* **2000**, *285*, 235.
- (157) Yu, H. T.; Vela, M. A.; Fronczek, F. R.; McLaughlin, M. L.; Barkley, M. D. *J. Am. Chem. Soc.* **1995**, *117*, 348.
- (158) Bartlett, G. R. *J. Biol. Chem.* **1959**, *234*, 466.
- (159) Lee, J. C.; Gray, H. B.; Winkler, J. R. *J. Am. Chem. Soc.* **2008**, *130*, 6898.
- (160) Pace, C. N.; Vajdos, F.; Fee, L.; Grimsley, G.; Gray, T. *Protein Sci.* **1995**, *4*, 2411.
- (161) Chen, Y. H.; Yang, J. T.; Chau, K. H. *Biochemistry* **1974**, *13*, 3350.
- (162) Lee, J. C.; Engman, K. C.; Tezcan, F. A.; Gray, H. B.; Winkler, J. R. *Proc. Natl. Acad. Sci. U. S. A.* **2002**, *99*, 14778.
- (163) Saito, H.; Dhanasekaran, P.; Baldwin, F.; Weisgraber, K. H.; Lund-Katz, S.; Phillips, M. C. *J. Biol. Chem.* **2001**, *276*, 40949.
- (164) Tamm, L. K. *Biochim. Biophys. Acta* **1991**, *1071*, 123.
- (165) Kucerka, N.; Tristram-Nagle, S.; Nagle, J. F. *Biophys. J.* **2006**, *90*, L83.
- (166) Nagle, J. F.; Wiener, M. C. *Biochim. Biophys. Acta* **1988**, *942*, 1.
- (167) Gazzara, J. A.; Phillips, M. C.; Lund-Katz, S.; Palgunachari, M. N.; Segrest, J. P.; Anantharamaiah, G. M.; Rodriguez, W. V.; Snow, J. W. *J. Lipid Res.* **1997**, *38*, 2147.
- (168) Rhoades, E.; Ramlall, T. F.; Webb, W. W.; Eliezer, D. *Biophys. J.* **2006**, *90*, 4692.

- (169) Schulthess, G.; Compassi, S.; Werder, M.; Han, C. H.; Phillips, M. C.; Hauser, H. *Biochemistry* **2000**, *39*, 12623.
- (170) Fernández, C. O.; Hoyer, W.; Zweckstetter, M.; Jares-Erijman, E. A.; Subramaniam, V.; Griesinger, C.; Jovin, T. M. *EMBO J.* **2004**, *23*, 2039.
- (171) Ramakrishnan, M.; Jensen, P. H.; Marsh, D. *Biochemistry* **2003**, *42*, 12919.
- (172) Gorrissen, H.; Marsh, D.; Rietveld, A.; Dekruijff, B. *Biochemistry* **1986**, *25*, 2904.
- (173) Sankaram, M. B.; Brophy, P. J.; Marsh, D. *Biochemistry* **1989**, *28*, 9685.
- (174) Helenius, A.; McCaslin, D. R.; Fries, E.; Tanford, C.; Sidney, F.; Lester, P. *Methods Enzymol.* **1979**, *56*, 734.
- (175) Bertoncini, C. W.; Jung, Y. S.; Fernández, C. O.; Hoyer, W.; Griesinger, C.; Jovin, T. M.; Zweckstetter, M. *Proc. Natl. Acad. Sci. U. S. A.* **2005**, *102*, 1430.
- (176) Bartels, T.; Ahlstrom, L. S.; Leftin, A.; Kamp, F.; Haass, C.; Brown, M. F.; Beyer, K. *Biophys. J.* **2010**, *99*, 2116.
- (177) Vamvaca, K.; Volles, M. J.; Lansbury, P. T. *J. Mol. Biol.* **2009**, *389*, 413.
- (178) Segrest, J. P.; Jones, M. K.; Deloof, H.; Brouillette, C. G.; Venkatachalapathi, Y. V.; Anantharamaiah, G. M. *J. Lipid Res.* **1992**, *33*, 141.
- (179) Chou, P. Y.; Fasman, G. D. *Biochemistry* **1975**, *14*, 2536.
- (180) Tamm, L. K. In *Membrane Protein Structure Experimental Approaches*; White, S. H., Ed.; Oxford University Press: New York, 1994, p 283.
- (181) Ben-Tal, N.; Honig, B.; Peitzsch, R. M.; Denisov, G.; McLaughlin, S. *Biophys. J.* **1996**, *71*, 561.
- (182) McIntosh, T. J.; Holloway, P. W. *Biochemistry* **1987**, *26*, 1783.
- (183) Takamori, S.; Holt, M.; Stenius, K.; Lemke, E. A.; Gronborg, M.; Riedel, D.; Urlaub, H.; Schenck, S.; Brugger, B.; Ringler, P.; Muller, S. A.; Rammner, B.; Gräter, F.; Hub, J. S.; De Groot, B. L.; Mieskes, G.; Moriyama, Y.; Klingauf, J.; Grubmüller, H.; Heuser, J.; Wieland, F.; Jahn, R. *Cell* **2006**, *127*, 831.
- (184) Yap, T. L.; Gruschus, J. M.; Velayti, A.; Westbroek, W.; Goldin, E.; Moaven, N.; Sidransky, E.; Lee, J. C. *J. Biol. Chem.* **2011**, *286*, 28080.

- (185) Heinrich, F.; Ng, T.; Vanderah, D. J.; Shekhar, P.; Mihailescu, M.; Nanda, H.; Losche, M. *Langmuir* **2009**, *25*, 4219.
- (186) Pfefferkorn, C. M.; Jiang, Z.; C., L. J. *Biochim. Biophys. Acta, Biomembr.* **2011**.
- (187) Fiaux, J.; Bertelsen, E. B.; Horwich, A. L.; Wuthrich, K. *J. Biomol. NMR* **2004**, *29*, 289.
- (188) Dura, J. A.; Pierce, D. J.; Majkrzak, C. F.; Maliszewskyj, N. C.; McGillivray, D. J.; Losche, M.; O'Donovan, K. V.; Mihailescu, M.; Perez-Salas, U.; Worcester, D. L.; White, S. H. *Rev. Sci. Instrum.* **2006**, *77*.
- (189) Schalke, M.; Kruger, P.; Weygand, M.; Losche, M. *Biochim. Biophys. Acta, Biomembr.* **2000**, *1464*, 113.
- (190) Ankner, J. F.; Majkrzak, C. F. *Proc. SPIE* **1992**, *1738*, 260.
- (191) Gell, C.; Brockwell, D.; Smith, A. *Handbook of Single Molecule Fluorescence Spectroscopy*; Oxford University Press: New York, 2006.
- (192) Middleton, E. R.; Rhoades, E. *Biophys. J.* **2010**, *99*, 2279.
- (193) Bhatnagar, V.; Anjaiah, S.; Puri, N.; Darshanam, B. N. A.; Ramaiah, A. *Arch. Biochem. Biophys.* **1993**, *307*, 183.
- (194) Fowler, D. M.; Koulov, A. V.; Alory-Jost, C.; Marks, M. S.; Balch, W. E.; Kelly, J. W. *PLoS. Biol.* **2006**, *4*, 100.
- (195) Hurbain, I.; Geerts, W. J. C.; Boudier, T.; Marco, S.; Verkleij, A. J.; Marks, M. S.; Raposo, G. *Proc. Natl. Acad. Sci. U. S. A.* **2008**, *105*, 19726.
- (196) Brilliant, M. H. *Pigm. Cell. Res.* **2001**, *14*, 86.
- (197) Kubo, S.; Nemani, V. M.; Chalkley, R. J.; Anthony, M. D.; Hattori, N.; Mizuno, Y.; Edwards, R. H.; Fortin, D. L. *J. Biol. Chem.* **2005**, *280*, 31664.
- (198) Devi, C. C.; Tripathi, R. K.; Ramaiah, A. *Eur. J. Biochem.* **1987**, *166*, 705.
- (199) Canovas, F. G.; Garciacarmona, F.; Sanchez, J. V.; Pastor, J. L. I.; Teruel, J. A. L. *J. Biol. Chem.* **1982**, *257*, 8738.
- (200) Dunn, L. C.; Thigpen, L. W. *J. Hered.* **1930**, *21*, 495.

- (201) Kwon, B. S.; Chintamaneni, C.; Kozak, C. A.; Copeland, N. G.; Gilbert, D. J.; Jenkins, N.; Barton, D.; Francke, U.; Kobayashi, Y.; Kim, K. K. *Proc. Natl. Acad. Sci. U. S. A.* **1991**, *88*, 9228.
- (202) Berson, J. F.; Harper, D. C.; Tenza, D.; Raposo, G.; Marks, M. S. *Mol. Biol. Cell* **2001**, *12*, 3451.
- (203) Theos, A. C.; Truschel, S. T.; Raposo, G.; Marks, M. S. *Pigm. Cell. Res.* **2005**, *18*, 322.
- (204) Berson, J. F.; Theos, A. C.; Harper, D. C.; Tenza, D.; Raposo, G.; Marks, M. S. *J. Cell Biol.* **2003**, *161*, 521.
- (205) Hoashi, T.; Muller, J.; Vieira, W. D.; Rouzaud, F.; Kikuchi, K.; Tamaki, K.; Hearing, V. J. *J. Biol. Chem.* **2006**, *281*, 21198.
- (206) Harper, D. C.; Theos, A. C.; Herman, K. E.; Tenza, D.; Raposo, G.; Marks, M. S. *J. Biol. Chem.* **2008**, *283*, 2307.
- (207) Kummer, M. P.; Maruyama, H.; Huelsmann, C.; Baches, S.; Weggen, S.; Koo, E. H. *J. Biol. Chem.* **2009**, *284*, 2296.
- (208) Hoashi, T.; Tamaki, K.; Hearing, V. J. *FASEB J.* **2010**, *24*, 916.
- (209) McGlinchey, R. P.; Shewmaker, F.; McPhie, P.; Monterroso, B.; Thurber, K.; Wickner, R. B. *Proc. Natl. Acad. Sci. U. S. A.* **2009**, *106*, 13731.
- (210) Watt, B.; van Niel, G.; Fowler, D. M.; Hurbain, I.; Luk, K. C.; Stayrook, S. E.; Lemmon, M. A.; Raposo, G.; Shorter, J.; Kelly, J. W.; Marks, M. S. *J. Biol. Chem.* **2009**, *284*, 35543.
- (211) Leonhardt, R. M.; Vigneron, N.; Rahner, C.; Van den Eynde, B. J.; Cresswell, P. *J. Biol. Chem.* **2010**, in press.
- (212) Hoashi, T.; Sato, S.; Yamaguchi, Y.; Passeron, T.; Tamaki, K.; Hearing, V. J. *FASEB J.* **2010**, *24*, 1616.
- (213) Puri, N.; Gardner, J. M.; Brilliant, M. H. *J. Invest. Dermatol.* **2000**, *115*, 607.
- (214) LeVine, H. In *Amyloid, Prions, and Other Protein Aggregates*; Academic Press Inc: San Diego, 1999; Vol. 309, p 274.
- (215) Xue, W. F.; Homans, S. W.; Radford, S. E. *Proc. Natl. Acad. Sci. U. S. A.* **2008**, *105*, 8926.

- (216) Thirumalai, D.; Klimov, D. K.; Dima, R. I. *Curr. Opin. Struct. Biol.* **2003**, *13*, 146.
- (217) Morris, A. M.; Watzky, M. A.; Finke, R. G. *Biochim. Biophys. Acta, Proteins Proteomics* **2009**, *1794*, 375.
- (218) Hofrichter, J.; Ross, P. D.; Eaton, W. A. *Proc. Natl. Acad. Sci. U. S. A.* **1974**, *71*, 4864.
- (219) Margittai, M.; Langen, R. *Q. Rev. Biophys.* **2008**, *41*, 265.
- (220) Tycko, R. *Q. Rev. Biophys.* **2006**, *39*, 1.
- (221) Dusa, A.; Kaylor, J.; Edridge, S.; Bodner, N.; Hong, D. P.; Fink, A. L. *Biochemistry* **2006**, *45*, 2752.
- (222) Kaylor, J.; Bodner, N.; Edridge, S.; Yamin, G.; Hong, D. P.; Fink, A. L. *J. Mol. Biol.* **2005**, *353*, 357.
- (223) Touchette, J. C.; Williams, L. L.; Ajit, D.; Gallazzi, F.; Nichols, M. R. *Arch. Biochem. Biophys.* **2010**, *494*, 192.
- (224) Chang, H. Y.; Lin, J. Y.; Lee, H. C.; Wang, H. L.; King, C. Y. *Proc. Natl. Acad. Sci. U. S. A.* **2008**, *105*, 13345.
- (225) Valencia, J. C.; Rouzaud, F.; Julien, S.; Chen, K. G.; Passeron, T.; Yamaguchi, Y.; Abu-Asab, M.; Tsokos, M.; Costin, G. E.; Yamaguchi, H.; Jenkins, L. M. M.; Nagashima, K.; Appella, E.; Hearing, V. J. *J. Biol. Chem.* **2007**, *282*, 11266.
- (226) Maurer-Stroh, S.; Debulpaep, M.; Kuemmerer, N.; de la Paz, M. L.; Martins, I. C.; Reumers, J.; Morris, K. L.; Copland, A.; Serpell, L.; Serrano, L.; Schymkowitz, J. W. H.; Rousseau, F. *Nat. Methods* **2010**, *7*, 237.
- (227) Murphy, R. M. *Annu. Rev. Biomed. Eng.* **2002**, *4*, 155.
- (228) O'Connor, D. V.; Phillips, D. *Time-correlated Single Photon Counting*; Academic Press: London, 1984.